

DISS. ETH NO. 26955

**OBJECTIVE COHERENT STRUCTURES NEAR THE
TURBULENT/NON-TURBULENT INTERFACE IN A
STABLY STRATIFIED TURBULENT FLOW**

A thesis submitted to attain the degree of
DOCTOR OF SCIENCES of ETH ZURICH

(Dr. sc. ETH Zurich)

presented by

Marius Mihai Neamtu-Halic

Master of Science, Roma TRE

born on 22.10.1989

citizen of Romania

accepted on the recommendation of

Prof. Dr. M. Holzner, examiner
Prof. Dr. J.R. Dawson, co-examiner
Prof. Dr. G. Haller, co-examiner

2020

PhD Thesis

**Objective coherent structures near the
turbulent/non-turbulent interface in a stably
stratified turbulent flow**

Marius Mihai Neamtu-Halic

July 9, 2020

Abstract

At the outer boundary of turbulent flows, irrotational ambient fluid is continuously entrained into the turbulent flow region across a sharp and highly convoluted interface, the so-called turbulent/non-turbulent interface (TNTI). This process has a direct bearing on the transport and mixing of fluid mass and momentum in a variety of flows, as for example in jets, wakes and boundary layers. Many recent studies indicated that vortical structures might play a fundamental role in the entrainment process; however, arbitrariness in vortex identification methods has hampered our ability to properly identify coherent structures and establish their role in this process. A recent string of studies developing the *Lagrangian coherent structures* theory enables to overcome the issues connected with the classic vortex extraction methods. By imposing the material coherence of the vortex core, these identification methods fulfill the objective property of continuum mechanics, i.e. observer-independence, which has been neglected in the past.

The main aim of this work is to use these novel detection methods to educe objective vortical structures (OVSs) from a gravity current flow and shed a light on the relation between these structures and the turbulent entrainment process. Gravity currents are important in geophysical applications, as for example in the case of oceanic overflows that are observed to play a key role in the thermohaline circulation and consequently in the climate dynamics. A better understanding of the role of OVSs on the turbulent entrainment will hence improve our ability to devise models for the growth rate of these geophysical currents, which might increase the accuracy of climate model predictions.

In the first part of the thesis, the impact of OVSs on the TNTI and entrainment of an experimentally realized gravity current is investigated. For flow measurements, a novel multivolume 3D particle tracking velocimetry technique is developed and to extract the OVSs, an automatic 3D extraction algorithm for multiple structures identification is implemented. A conditional analysis based on the presence of OVSs near the interface shows that the structures modulate the average TNTI height, affecting thereby the interface area, and organize the flow field on both the turbulent and non-turbulent sides of the gravity current boundary, influencing the local entrainment velocity. In conclusion, the

results show that coherent structures have an impact on the two key factors of the overall entrainment flux, namely the TNTI area and the local entrainment velocity.

In the second part of the thesis, direct numerical simulations (DNSs) of a temporal gravity current is used to investigate the role of OVSs on the time evolution of the TNTI area. The TNTI area is continuously produced and destroyed via stretching and curvature/propagation effects. Our results show that the production/destruction of the TNTI area is a multiscale process, in which production by flow stretching is balanced at all the scales of the TNTI wrinkles by destruction via curvature/propagation effects. This scale-by-scale balance is shown to be compatible with a demonstrated scale invariance of the OVSs near the TNTI, in which TNTI area is produced at the leading edge and destroyed at the trailing edge of the TNTI bulges in the OVSs proximity. We show that the latter observation can be explained by the rotational motion of the flow induced by OVSs near the interface. This study implies that the vortical structures not only contribute to set the TNTI area, but they also influence the multiscale process of its time evolution.

In the last part of the thesis, the dynamics of the OVSs and their role on the local entrainment process is investigated. To this end, DNSs of a temporal gravity current are used. For the dynamical characterization of the structures, radial profiles of the enstrophy transport terms inside the OVSs are computed. It is shown that vortex-stretching produces enstrophy inside the OVSs, while viscous diffusion transfers the enstrophy from the core of the OVSs to the nearby fluid parcels. Although overlooked in the past, the viscous dissipation of enstrophy is shown to play a role on the enstrophy budget, while the baroclinic torque is negligible. When considering the region near the TNTI, it is shown that the intensity of the conditional profiles of the enstrophy transport terms across the interface is considerably higher when a structure is present near the interface. Moreover, the shape of these profiles is observed to be compatible with the radial profiles of an OVS positioned near the TNTI. The overall picture that emerges is that the vortical structures have a significant impact on the enstrophy transport across the TNTI and thus on the mechanism through which an initially irrotational fluid parcel enters in the turbulent region. In conclusion, this dissertation presents novel tools for a rigorous investigation of the impact of vortical structures on the TNTI area that enable a better understanding of their role on the entrainment process. Although here limited to gravity current flow, the results presented in this dissertation are expected to be transferable to other turbulent flows that are bounded by a turbulent/non-turbulent interface, such as jets, wakes and boundary layers.

Sommario

Lo scopo principale di questa tesi è quello di utilizzare metodi di estrazione oggettivi per l'identificazione di strutture vorticose in correnti di gravità al fine di far luce sulla relazione tra queste strutture e il processo di *entrainment*. L'*entrainment* turbolento è quel processo per il quale il fluido ambiente in stato irrotazionale presente all'esterno di una regione turbolenta viene continuamente inglobato nella regione stessa fluendo attraverso una sottile interfaccia estremamente convoluta, detta interfaccia turbolenta/non-turbolenta (TNTI). Tale processo influenza notevolmente il trasporto ed il mescolamento (*mixing*) sia della massa fluida, sia della sua stessa quantità di moto in una vasta gamma di flussi quali i getti, le scie, e gli strati limite. Numerose ricerche recenti indicano che le strutture vorticose coerenti potrebbero giocare un ruolo fondamentale nel processo di *entrainment*; ciononostante, l'arbitrarietà nei metodi per l'identificazione dei vortici ha ostacolato la nostra capacità di individuare in un modo appropriato le strutture coerenti e capirne il ruolo in questo processo. Una recente linea di ricerca, la cosiddetta *teoria delle strutture coerenti di Lagrange*, permette di ovviare alle problematiche relative ai metodi classici di estrazione, imponendo la coerenza materiale del nucleo del vortice. Questi metodi di identificazione rispettano dunque la proprietà oggettiva della meccanica classica, ovvero l'indipendenza dal sistema di riferimento dell'osservatore, trascurata da molti dei metodi classici.

In questo lavoro, l'analisi del legame tra le strutture coerenti e il processo di *entrainment* è stata effettuata nell'ambito delle correnti di gravità. Le correnti di gravità hanno rilevanti applicazioni geofisiche, come ad esempio nel caso degli *oceanic overflows* che svolgono un ruolo chiave nella circolazione termoalina e di conseguenza nella dinamica climatica. Ne consegue che una più approfondita conoscenza del ruolo delle strutture nell'*entrainment* turbolento permette lo sviluppo di modelli più accurati per la simulazione di queste correnti che possono avere un notevole impatto sui modelli climatici.

Nella prima parte di questa tesi, viene studiato l'impatto delle strutture vorticose oggettive (OVSs) sulla TNTI e sul processo di *entrainment* di una corrente di gravità realizzata sperimentalmente in laboratorio. Per l'analisi dei dati è stata sviluppata una nuova tecnica multivolume di 3D *particle tracking velocimetry* e le OVSs vengono estratte utilizzando un

nuovo algoritmo automatico per l'identificazione di molteplici strutture in tre dimensioni. Un'analisi condizionale è stata usata per studiare l'influenza delle OVSs sulla TNTI e sul processo di *entrainment*. L'analisi ha dimostrato che le strutture modulano l'altezza della TNTI, influenzandone dunque l'area della superficie, e che esse organizzano il campo di moto del fluido da entrambe le parti dell'interfaccia, sia nella regione turbolenta che nella regione irrotazionale, influenzando di conseguenza la velocità di *entrainment* locale. Pertanto, il quadro generale che ne emerge è che le OVSs condizionano entrambe le quantità che governano il flusso di *entrainment*, ovvero l'area dell'interfaccia e la velocità locale di *entrainment*.

Nella seconda parte della tesi, vengono impiegate simulazioni numeriche dirette (DNSs) di correnti di gravità temporali per lo studio dell'impatto delle strutture vorticosi sul processo di produzione/distruzione dell'area della TNTI. L'area dell'interfaccia viene continuamente prodotta e distrutta attraverso effetti di *stretching* e di curvatura/propagazione della stessa. Attraverso l'analisi delle simulazioni, si è dimostrato che il processo di produzione/distruzione dell'interfaccia è un processo multiscala in cui la produzione di area tramite *stretching* viene bilanciata a tutte scale della TNTI dalla distruzione tramite effetti curvatura/propagazione. Successivamente, è stato dimostrato che questo equilibrio è compatibile con una invarianza di scala delle OVSs vicino alla TNTI, nella quale l'area della TNTI viene creata nella parte anteriore dell'interfaccia in prossimità delle strutture e viene distrutta nella zona posteriore della stessa. Inoltre è stato dimostrato che questo tipo di meccanismo locale può essere associato ad un campo di moto rotatorio indotto dalle strutture in prossimità dell'interfaccia. In conclusione, in questa seconda parte è stato mostrato come le strutture coerenti influenzino l'*entrainment* locale anche attraverso il processo di produzione/distruzione dell'interfaccia.

Nell'ultima parte della tesi, vengono studiate la dinamica delle OVSs e il loro ruolo nel processo locale di *entrainment*. A tal fine, vengono utilizzate DNSs di una corrente di gravità temporale. Per la caratterizzazione dinamica delle strutture, si sono valutati i profili radiali dei termini dell'equazione di trasporto dell'instrofia all'interno delle OVSs. I risultati della nostra analisi mostrano che il termine di *vortex-stretching* produce instrofia all'interno delle OVSs mentre la diffusione viscosa la trasferisce dal nucleo delle OVSs alle particelle di fluido circostanti. Sebbene spesso trascurata in passato, la dissipazione viscosa dell'instrofia all'interno delle strutture vorticosi ha un ruolo fondamentale nel bilancio della stessa, mentre il momento torcente baroclinico è stato osservato essere essenzialmente trascurabile. Quest'ultima parte del lavoro verte sul ruolo delle OVSs nel processo locale di *entrainment*. Si è così dimostrato che l'intensità dei profili dei termini delle equazioni di trasporto dell'instrofia, attraverso l'interfaccia, è considerevolmente maggiore quando una OVS è presente vicino alla TNTI e che la forma di questi profili è compatibile con la forma dei profili radiali di una OVS posizionata in prossimità della TNTI. Ciò dimostra che le strutture vorticosi hanno un impatto notevole sul trasporto dell'instrofia attraverso l'interfaccia e dunque sul processo attraverso il quale una particella fluida, in stato irrotazionale, entra nella regione turbolenta.

In conclusione, questa tesi presenta una serie di strumenti per lo studio rigoroso dell'impatto che strutture vorticosi hanno sull'area dell'interfaccia turbolenta/non-turbolenta e sul pro-

cesso di *entrainment*. Sebbene, l'analisi effettuata qui sia stata condotta nel caso particolare di correnti di gravità, si prevede che i risultati presentati in questo lavoro possano essere analoghi anche ad altri tipi di flussi turbolenti che sono confinati da regioni irrotazionali come ad esempio i getti, le scie e gli strati limite turbolenti.

Contents

Abstract	i
Sommario	iii
1 Introduction	1
1.1 The turbulent/non-turbulent interface	3
1.2 Gravity currents	4
1.3 Objectives	6
1.4 Thesis Outline	6
Bibliography	10
2 Lagrangian coherent structures and entrainment near the turbulent/non-turbulent interface of a gravity current	15
2.1 Introduction	16
2.2 Methods	17
2.2.1 Experiments	17
2.2.2 Measurements	18
2.2.3 TNTI identification and local entrainment velocity	20
2.2.4 VLCSs eduction	22
2.2.5 VLCS size and orientation	25
2.3 Results	26
2.3.1 VLCS geometrical properties	26
2.3.2 Interaction between the TNTI and VLCSs	28
2.4 Discussion and summary	34
Bibliography	37

3	Connecting the time evolution of the turbulence interface to coherent structures	41
3.1	Introduction	42
3.2	Methods	44
3.2.1	Direct numerical simulations	44
3.2.2	TNTI identification and local entrainment velocity	46
3.2.3	Equation for the time evolution of the TNTI area	47
3.2.4	Coherent flow structures extraction	47
3.3	Results	48
3.3.1	Time evolution of the TNTI area	48
3.3.2	Time evolution of the TNTI area: a 2D approach	51
3.3.3	Impact of OECSs on the production/destruction of TNTI area	57
3.4	Concluding remarks	64
	Bibliography	66
4	Role of vortical structures for enstrophy and scalar transport in a turbulent flow with and without stable stratification	71
4.1	Introduction	72
4.2	Methods	74
4.2.1	DNS data set	74
4.2.2	OECSs eduction and TNTI identification	76
4.2.3	Radial profiles and conditional profiles.	78
4.3	Results	78
4.3.1	General description of coherent structures	78
4.3.2	Radial profiles of the terms of enstrophy and scalar transport equations	81
4.3.3	Impact of coherent structures on the enstrophy and concentration transport near the TNTI	84
4.4	Summary and conclusions	87
	Bibliography	90
5	Summary and Conclusions	95
5.1	Suggestions for future work	97
	Bibliography	99
	Acknowledgements	100
	Curriculum Vitae	102

Chapter 1

Introduction

In turbulent flows, the characteristics and dynamics of the vortical structures have been studied extensively in recent decades. Vortical structures are often defined as tubular regions with a high content of coherent vorticity and with a lifetime larger than the typical time-scales of the flow. These structures are considered as one of the building blocks of turbulence and they offer the possibility of understanding complex flow phenomena using relatively simple models e.g. see Lesieur (1987). Moreover, several studies indicated that vortical structures play a key role for the transport and mixing of mass, momentum and scalars (e.g. temperature). Understanding how these transport processes are related to the vortical structures is crucial for practical applications, as for example turbulence control, heat exchange and dispersion of pollutants in atmosphere.

Following a common categorization in turbulent flows (da Silva *et al.*, 2011), vortical structures can be subdivided into two classes, namely, the so-called *large-scale structures* and the *intense vortical structures*. The large-scale structures are flow dependent and generally originate from the mechanism that generates, or maintains, the turbulence (Davidson, 2015). Their geometrical and kinetic properties such as size, orientation and vorticity content depends on the particular type of flow. Usually identified through a threshold on the pressure (da Silva *et al.*, 2011), the size of these structures is also known to be an outer cut-off for the range of possible sizes of the vortical structures in the turbulent flow. Moreover, they are governed by an inviscid mechanism and are responsible for the production of the turbulent kinetic energy that is transferred to the smaller scales (Davidson, 2015).

As suggested by the name, the intense vortical structures contain the highest levels of

the flow vorticity. Usually identified with a particularly high threshold on vorticity vector, the intense vortical structures are also known in isotropic turbulence under the name of *vortex filaments* (Siggia, 1981). Many studies have been dedicated to these structures, particularly in isotropic turbulence (Siggia, 1981; Vincent & Meneguzzi, 1991; Ashurst *et al.*, 1987; Jimenez & Wray, 1998), but also in other flows such as mixing layers (Tanahashi *et al.*, 2001), channel flows (Kang *et al.*, 2007) and jets (Ganapathisubramani *et al.*, 2008; da Silva *et al.*, 2011). Different from the large-scale vortical structures, the intense vortical structures share similar characteristics in a variety of flows. For example, the vortex radius is of order of 5η , where η is the Kolmogorov micro-scale, in isotropic turbulence, mixing layers, channel flows and jets. While intense vortical structures seem to be a general feature of many homogeneous density turbulent flows, they have never been investigated in stratified flows which are the main focus of this thesis.

Up to date, progress in our understanding of the role of vortical structures in turbulence has been hampered by the fact that there is no generally accepted definition of vortical structures yet. There are broadly two accepted characteristics for the definition of vortical structures. The first is that the vortices should possess a high content of vorticity and the second one is that they should be materially coherent (Haller *et al.*, 2016). In most of the studies, their identification is made by a threshold on the vorticity relative to other flow domains (Hussain, 1986; Jiménez *et al.*, 1993; da Silva *et al.*, 2011) or relative to the strain (Okubo, 1970; Hunt *et al.*, 1988; Weiss, 1991; Hua & Klein, 1998). In other studies a high degree of material invariance of the vortex core is required (Chong *et al.*, 1990; Provenzale, 1999; Haller, 2005; Chelton *et al.*, 2011). Indeed as Haller *et al.* (2016) recognized, what constitutes a high degree of vorticity might be "subject to individual judgement, thresholding and choice of frame of reference", whereas the material coherence of a vortex core holds even "more promise as a first requirement in an unambiguous vortex definition". The latter requirement implies that a vortex must have the objective property of continuum mechanics, i.e. it must be observer-independent.

A recent vortical structure identification method that fulfils both the aforementioned characteristics has been developed by Haller *et al.* (2016). This method uses a new dynamic version of the classic polar decomposition introduced in Haller *et al.* (2016) and identifies vortical Lagrangian coherent structures (VLCSs) as tubes of deforming fluid elements that complete the same material rotation relative to the mean rotation of the surrounding fluid. Haller *et al.* (2016) showed that the initial position of such tubes coincide with the tubular level surfaces of the so-called Lagrangian-Averaged Vorticity Deviation (LAVD), "the trajectory integral of the normed difference of the vorticity from its spatial mean". Moreover, in the limit of zero advection time, the Lagrangian definition turns into an objective Eulerian vortex definition. The objective vortical coherent structures (OECSs) are identified by tubular surfaces of equal material rotation rate that is objectively measured by the Instantaneous Vorticity Deviation (IVD). These two methods allow overcoming the issues connected to the arbitrariness of the classic identification methods and constitute a promising tool for a rigorous vortex definition that is objective as required by experimental reproducibility. While both the aforementioned methods are equivalently valid, they are intimately different. The LAVD method guarantees the material coherence of the vortex

core over an imposed extraction time, but at the expense of high computational costs due to the use of vorticity along fluid trajectories. On the other hand, the IVD method is much less computationally expensive but the material coherence of vortex cores is not guaranteed over time. However, in a recent work by Serra & Haller (2016), it was shown that the initial position of many objective Eulerian vortices coincide with their Lagrangian counterpart, thereby justifying the use of objective Eulerian methods when computational costs are unsustainable. In this thesis, the LAVD method is used in chapter 2, where experimental data is employed, whereas the IVD method is used in chapter 3 and chapter 4, in which heavier direct numerical simulation data is employed.

Vortical structures often reside at the dividing interface between turbulent and non-turbulent flow regions which is an important but not well understood feature of several turbulent flows. In this thesis, a particular attention is given the influence of vortical structures on the kinematics and dynamics of the flow near this interface.

1.1 The turbulent/non-turbulent interface

A sharp and highly contorted interface is known to separate turbulent fluid from the outer irrotational region of free shear (e.g. jets, wakes and mixing layers) and semi-bounded (e.g. boundary layers and wall jets) turbulent flows (Corrsin & Kistler, 1955). Across this interface, so-called turbulent/non turbulent interface (TNTI), initially irrotational fluid is continuously incorporated in the turbulent region, a phenomenon known as turbulent entrainment. From a local prospective, the flux of entrained fluid can be expressed as the product of the local entrainment velocity, averaged over the whole TNTI surface, and the instantaneous, wrinkled interface area. Conversely, the global entrainment flux is expressed based on the time averaged and flat interface area (e.g. a plane for a planar jet or a cone for a round turbulent jet) and the mean entrainment velocity. To date, it is widely accepted that the turbulent entrainment occurs at the smallest scales of turbulence and that is dominated by viscous processes (Mathew & Basu, 2002; Westerweel *et al.*, 2009). However, it is also broadly recognized that the overall entrainment rate is independent on viscosity, viz. Reynolds number (Tritton, 1988; Tsinober, 2009). It is therefore believed the large-scale vortical structures act to cancel the Reynolds number dependence of the small-scale entrainment (Townsend, 1980; Sreenivasan *et al.*, 1989). In other words, the large-scale vortical structures distort and enhance the TNTI area in a way to cancel the dependence on the small viscous scales. Recent flow-visualizations from direct numerical simulations suggest that indeed vortical structures of average size of the Taylor microscale occupy the largest convolutions of the TNTI, thereby lending support to this view (da Silva & dos Reis, 2011). A more rigorous approach that uses conditional analysis showed that effectively, the TNTI surface area increases in the vicinity of large scale motion of a turbulent boundary layer (Lee *et al.*, 2017). However, a systematic analysis case of how objectively identified vortical structures modulate the TNTI is still missing. Furthermore, it is not clear yet how the large-scale vortices in the TNTI proximity interact with the interface to set the small-scale local entrainment.

The TNTI area is continuously produced and destroyed as a result of stretching and

curvature/production mechanisms. Hypothesizing a constant entrainment velocity over the TNTI, (Phillips, 1972) concluded that on average the curvature/propagation effect creates TNTI area along the bulges and destroys it in the valleys of the TNTI. While this is an important theoretical finding, the local entrainment velocity is known to vary significantly along the TNTI (Holzner & Lüthi, 2011; Wolf *et al.*, 2012; Watanabe *et al.*, 2014), with a predominance of negative values implying entrainment that alternate with sporadic positive values representing detrainment zones. It is thus not clear how this variation of the entrainment changes the curvature/propagation effect. In addition, it was observed that the coherent vortices that fill the bulges near the TNTI distort the mean flow in their proximity (Mistry *et al.*, 2016). This indicates that the vortical structures may have an impact on the process of production/destruction of the TNTI area. However, the role of vortical structures on the time evolution of the TNTI is largely unknown.

The process through which an initially irrotational fluid parcel enters into the turbulent core region across the TNTI has been observed to occur in a sequence of two stages (Watanabe *et al.*, 2017). Initially, fluid parcel acquires vorticity at the outer layer of the TNTI via viscous diffusion of enstrophy. The outer layer of the TNTI where viscous effects are dominant is the so-called viscous superlayer. Afterwards, in a second stage the fluid particle undergoes an enstrophy amplification via the vortex-stretching mechanism in the so-called turbulent sublayer. Up to date it remains unclear whether the vortical structures that populate the region near the TNTI play a role in this process.

1.2 Gravity currents

In many flows in nature or industrial applications, turbulent shear flows develop in presence of stable stratification. One of the most common examples is the case of gravity currents, in which the flow is driven by the density difference between two fluids. Gravity currents are ubiquitous in nature and in practical applications (Simpson, 1999). The most spectacular examples include snow powder avalanches (figure 1.1a) and pyroclastic flows (figure 1.1b). The latter are characterized by the presence of suspended volcanic material and gasses at high temperature and they flow down along the mountainsides after a volcanic eruption, reaching top velocities between 50 and 300 Km/h. A further example of a gravity current is lahars (figure 1.2 a), a rather violent type of mudflow that forms as a result of volcanic eruptions. Lahars are composed of pyroclastic material, rocky debris and water and flow down from a volcano, typically along a river valley.

In these examples, the density difference between the gravity current and the ambient fluid (air) is given by the presence of suspended material. However, in other examples the density difference is due to a gradient of a scalar, as for example temperature or salinity. This is the case of the katabatic winds, also known as downslope winds, or gravity winds. These winds originate at high altitudes through rapid cooling of the air (figure 1.2 a). The cooled air, with a higher density as compared to the surrounding, flows down a sloping bottom under the force of gravity.

An important feature of these flows is that the turbulence generated by the shear is damped by the stable stratification.

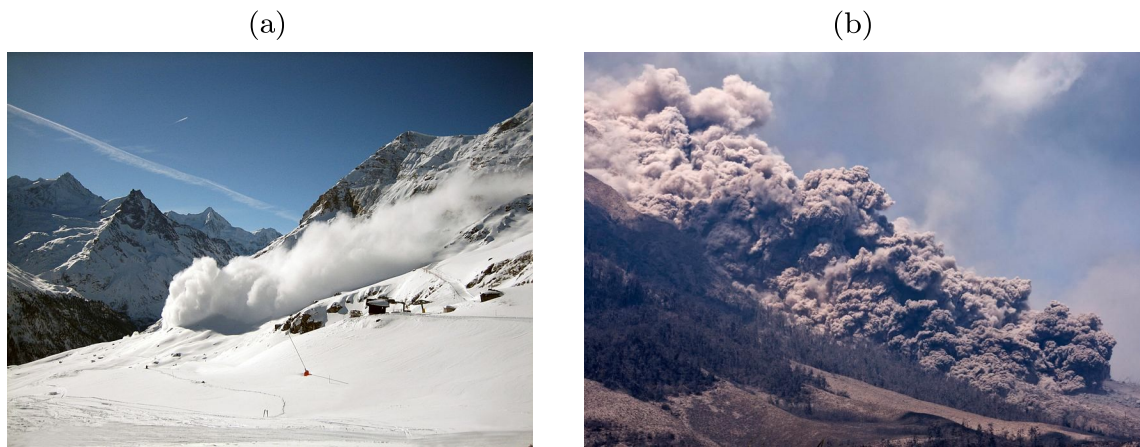


Figure 1.1: (a) Avalanche on the mountain Zinal, Switzerland (source: Camptocamp.org). (b) Example of pyroclastic flow (courtesy of Ulet Ifansasti—Getty Images).

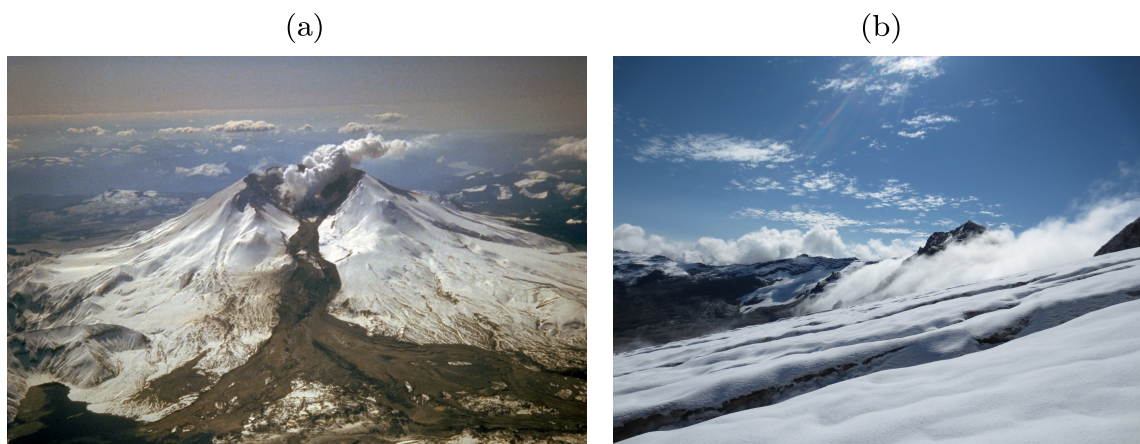


Figure 1.2: (a) Lahar on the Saint Elena mountain in march 1982 (source: USGS). (b) View of katabatic wind from the upper reaches of Tsanteleina Glacier in the western Italian Alps (courtesy of T. Shaw).

In this thesis, the particular case of inclined gravity currents is investigated. In this case, the density difference is given by a salinity gradient and a dense turbulent fluid flows in a lighter ambient fluid that is at rest along the bottom of an inclined wall. If the density difference between the two fluids is small enough, the so-called Boussinesq approximation applies, and this case is equivalent to lighter turbulent flow the flows up in a denser quiescent fluid along the top of an inclined wall.

For these flows, the entrainment coefficient is known to diminish with increasing ratio between the buoyancy and the shear strength of the flow, represented by the Richardson number Ri . Recently, it has been demonstrated (Krug *et al.*, 2015; van Reeuwijk *et al.*, 2018) that the reduction of the entrainment coefficient with increasing Ri is associated with the decrease of both the average entrainment velocity and the TNTI area. It remains thus to be understood whether the vortical structures that are known to populate the region near the TNTI play a role in the area reduction and whether these structures have an impact on the entrainment velocity decrease.

1.3 Objectives

The objectives of this thesis are to implement a fully automatic 3D extraction algorithm for objective coherent structures identification based on the LAVD and IVD fields and to use this algorithm to educe VLCSs and OECSs from experimental and direct numerical simulation data of a gravity current. The aim is to characterize these structures from a geometrical, kinematic and dynamic point of view and understand their role in the entrainment mechanism. In particular, with regard to the entrainment mechanism, the impact of the vortical structures on both the local entrainment velocity and the area of the TNTI is investigated. This allows us to obtain a new understanding of how the vortical structures modulate the TNTI area, how they control the time evolution of the area and how they impact the two step process of fluid parcels entrainment.

1.4 Thesis Outline

This thesis is the result of the three distinct scientific publications, each of which constitute an individual chapter, while the conclusions and the findings of this work are synthesized in a final chapter.

In chapter 2, large-scale 3D VLCSs are extracted from experimental data of a gravity current. The gravity current is realized using the experimental facility introduced in Krug *et al.* (2013). The facility allows to create a gravity current in steady state conditions by injecting a turbulent light fluid (a mixture of water and ethanol) at a constant rate in a denser ambient fluid (a mixture of water and salt) along the top wall of an inclined tank. Ambient fluid is continuously resupplied along the bottom of the tank to replenish the entrained fluid. A multivolume three dimensional particle tracking is developed for flow measurements, with the rationale of observing a large interrogation volume, while maintaining a high resolution. For 3D VLCSs identification, a new extraction algorithm that allows for multiple structures eduction is implemented. The size, shape and orientation are

used to characterize the VLCSs, while conditional analysis is used to assess their impact on the area of the TNTI and on the local entrainment velocity. The results presented in this chapter allow to understand how the large-scale vortical structures act to cancel the dependence of the entrainment rate on the viscosity.

Chapter 3 deals with the impact of objective coherent structures on the time evolution of the TNTI area. To this end, direct numerical simulation data of a temporal gravity current is used. While the algorithm described in chapter 2 is applied to the IVD field extract 3D OECSs for a flow visualization, the main outcomes are based on results from 2D vertical planes. The results show that the TNTI area is continuously produced through flow stretching and destroyed via curvature/propagation effects, which balance each other in time and at all the scales of the flow. In particular, the time evolution of the area is shown to be multiscale process that is compatible with an observed scale invariance of the OECSs in the TNTI proximity. Conditional analysis is used to show that TNTI area is produced at leading edge and destroyed at the trailing edge of the TNTI near a vortical structure. As the stratification increases, the magnitude of the stretching production and curvature/propagation destruction decreases. An explanation of the former is offered in terms of a fractal model of the TNTI, which shows that this decrease is largely attributable to a change TNTI geometry which tends to flatten at all the scales of the interfaces. The framework presented in chapter 3 permits to understand how the TNTI area is set at the different length-scales and what is the role played by vortical structures in this process.

In chapter 4, the dynamical structure of the OECSs is assessed. To this end, the same data of a temporal gravity current used for chapter 3 is employed. For the OECSs dynamical characterization, the radial profiles of the enstrophy transport equation terms are computed. In particular, it is shown that the enstrophy production via vortex-stretching does not balance the viscous diffusion and the viscous dissipation of enstrophy inside the boundaries of the OECSs, while the baroclinic torque has a negligible impact. For the OECSs with different sizes and different vertical distances from the wall, the radial profiles show a similar behavior although with a different magnitude. The conditional profiles of the enstrophy transport equation terms across the TNTI are fundamental to understand how initially non-turbulent fluid is entrained. The typical conditional profiles of these terms are reproduced and it is shown that when further conditioning to the presence of an OECS, their magnitude is up to one order of magnitude higher. This demonstrates that the shape of these conditional profiles might be largely connected with the presence of OECSs in the TNTI proximity, thereby shedding light on the important role played by vortical structures in the entrainment process. Moreover, the same analysis is conducted in terms of the scalar transport equation. It is shown that OECSs have an impact on the transport of the scalar, which is trapped within their boundaries. This results in an enhanced molecular diffusion as compared to the unconditioned mean diffusion, which means that the OECSs accelerate the mixing of the scalar. The results presented in this chapter clarify the dynamical behavior of the OECSs and sheds a light on their role on the local entrainment.

The upcoming chapters (2-4) of this thesis are based on the following publications:

Chapter 2:

M. Neamtu^{a,b,c,d,e}, D. Krug^{a,d,f}, G. Haller^{d,f} and M. Holzner^{a,d,f} (2019)

Lagrangian coherent structures and entrainment near the turbulent/non-turbulent interface of a gravity current. *J. Fluid. Mech.*, 877(824-843)

<https://doi.org/10.1017/jfm.2019.635>

^a Study concept and design; ^b Data acquisition; ^c Data analysis; ^d Interpretation of the data; ^e Manuscript Drafting; ^f Critical revision;

My contribution to this chapter is the implementation of a multivolume flow measurement technique. Subsequently, I performed the measurements, I post-processed the data and I implemented an algorithm of the extraction of vortical coherent structures. Writing codes for data analysis, plotting of the figures and writing the first draft of the manuscript were my task. All the co-authors contributed to improve the manuscript.

Chapter 3:

M. Neamtu^{a,c,d,e}, D. Krug^{a,c,d,f}, J.-P. Mollicone^b, M. van Reeuwijk^{b,d,f}, G. Haller^f and M. Holzner^{a,d,f} (2020)

Connecting the time evolution of the turbulence interface to coherent structures. Accepted for publication in *J. Fluid. Mech.*

^a Study concept and design; ^b Data acquisition; ^c Data analysis; ^d Interpretation of the data; ^e Manuscript Drafting; ^f Critical revision;

In this chapter, my contribution is the analysis of the numerical data, including setting up the algorithms of data analysis and the results interpretation. I have produced the figures and written the manuscript. All the co-authors contributed to improve the text.

Chapter 4:

M. Neamtu^{a,c,d,e}, J.-P. Mollicone^{b,f}, M. van Reeuwijk^{b,f} and M. Holzner^{a,d,f} (2020)

Role of vortical structures for enstrophy and scalar transport in flows with and without stable stratification. Submitted to *J. Turbul.*

^a Study concept and design; ^b Data acquisition; ^c Data analysis; ^d Interpretation of the data; ^e Manuscript Drafting; ^f Critical revision;

In this chapter, my contribution is the analysis of the numerical data, including setting up the algorithms of data analysis and the results interpretation. I have produced the figures and written the manuscript. All the co-authors contributed to improve the text.

In the last chapter of this thesis (Chapter 5), a summary of the conclusions drawn from the three publications is provided. Moreover, suggestions for future research topics related to the results presented here are made.

Bibliography

- ASHURST, W. T., KERSTEIN, A. R., KERR, R. M. & GIBSON, C. H. 1987 Alignment of vorticity and scalar gradient with strain rate in simulated navier–stokes turbulence. *Phys. Fluid.* **30** (8), 2343–2353. pages 2
- CHELTON, D. B., GAUBE, P., SCHLAX, M. G., EARLY, J. J. & SAMELSON, R. M. 2011 The influence of nonlinear mesoscale eddies on near-surface oceanic chlorophyll. *Science* **334** (6054), 328–332. pages 2
- CHONG, M. S., PERRY, A. E. & CANTWELL, B. J. 1990 A general classification of three-dimensional flow fields. *Phys. Fluids A* **2** (5), 765–777. pages 2
- CORRSIN, S. & KISTLER, A. L. 1955 Free-stream boundaries of turbulent flows . pages 3
- DAVIDSON, P. A. 2015 *Turbulence: an introduction for scientists and engineers*. Oxford University Press. pages 1
- GANAPATHISUBRAMANI, B., LAKSHMINARASIMHAN, K. & CLEMENS, N. T. 2008 Investigation of three-dimensional structure of fine scales in a turbulent jet by using cinematographic stereoscopic particle image velocimetry. *J. Fluid Mech.* **598**, 141–175. pages 2
- HALLER, G. 2005 An objective definition of a vortex. *J. Fluid Mech.* **525**, 1–26. pages 2
- HALLER, G., HADJIGHASEM, A., FARAZMAND, M. & HUHN, F. 2016 Defining coherent vortices objectively from the vorticity. *J. Fluid Mech.* **795**, 136–173. pages 2
- HOLZNER, M. & LÜTHI, B. 2011 Laminar superlayer at the turbulence boundary. *Phys. Rev. Lett.* **106** (13), 134503. pages 4
- HUA, B.L. & KLEIN, P. 1998 An exact criterion for the stirring properties of nearly two-dimensional turbulence. *Physica D* **113** (1), 98–110. pages 2
- HUNT, J. C. R., WRAY, A. A. & MOIN, P. 1988 Eddies, streams, and convergence zones in turbulent flows . pages 2

- HUSSAIN, A. K. M. F. 1986 Coherent structures and turbulence. *J. Fluid Mech.* **173**, 303–356. pages 2
- JIMENEZ, J. & WRAY, A. A. 1998 On the characteristics of vortex filaments in isotropic turbulence. *J. Fluid Mech.* **373**, 255–285. pages 2
- JIMÉNEZ, J., WRAY, A. A., SAFFMAN, P. G. & ROGALLO, R. S. 1993 The structure of intense vorticity in isotropic turbulence. *J. Fluid Mech.* **255**, 65–90. pages 2
- KANG, S.J., TANAHASHI, M. & MIYAUCHI, T. 2007 Dynamics of fine scale eddy clusters in turbulent channel flows. *J. Turbul.* (8), N52. pages 2
- KRUG, D., HOLZNER, M., LÜTHI, B., WOLF, M., KINZELBACH, W. & TSINOBER, A. 2013 Experimental study of entrainment and interface dynamics in a gravity current. *Exp. Fluids* **54** (5), 1530. pages 6
- KRUG, D., HOLZNER, M., LÜTHI, B., WOLF, M., KINZELBACH, W. & TSINOBER, A. 2015 The turbulent/non-turbulent interface in an inclined dense gravity current. *J. Fluid Mech.* **765**, 303–324. pages 6
- LEE, J., SUNG, H. J. & ZAKI, T. A. 2017 Signature of large-scale motions on turbulent/non-turbulent interface in boundary layers. *J. Fluid Mech.* **819**, 165–187. pages 3
- LESIEUR, M.L. 1987 *Turbulence in fluids: stochastic and numerical modelling*. Nijhoff Boston, MA. pages 1
- MATHEW, J. & BASU, A. J. 2002 Some characteristics of entrainment at a cylindrical turbulence boundary. *Phys. Fluids* **14** (7), 2065–2072. pages 3
- MISTRY, D., PHILIP, J., DAWSON, J. R. & MARUSIC, I. 2016 Entrainment at multi-scales across the turbulent/non-turbulent interface in an axisymmetric jet. *J. Fluid Mech.* **802**, 690–725. pages 4
- OKUBO, A. 1970 Horizontal dispersion of floatable particles in the vicinity of velocity singularities such as convergences. In *Deep-Sea Res.*, , vol. 17, pp. 445–454. Elsevier. pages 2
- PHILLIPS, O. M. 1972 The entrainment interface. *J. Fluid Mech.* **51** (1), 97–118. pages 4
- PROVENZALE, A. 1999 Transport by coherent barotropic vortices. *Annu. Rev. Fluid Mech.* **31** (1), 55–93. pages 2
- VAN REEUWIJK, M., KRUG, D. & HOLZNER, M. 2018 Small-scale entrainment in inclined gravity currents. *Environ. Fluid Mech.* **18** (1), 225–239. pages 6
- SERRA, MATTIA & HALLER, GEORGE 2016 Objective eulerian coherent structures. *Chaos* **26** (5), 053110. pages 3

- SIGGIA, E. D. 1981 Numerical study of small-scale intermittency in three-dimensional turbulence. *J. Fluid Mech* **107**, 375–406. pages 2
- DA SILVA, C. B., DOS REIS, R.J.N. & PEREIRA, J.C.F. 2011 The intense vorticity structures near the turbulent/non-turbulent interface in a jet. *J. Fluid Mech.* **685**, 165–190. pages 1, 2
- DA SILVA, C. B. & DOS REIS, R. J. N. 2011 The role of coherent vortices near the turbulent/non-turbulent interface in a planar jet. *Phil. Trans. R. Soc. A* **369** (1937), 738–753. pages 3
- SIMPSON, J. E. 1999 *Gravity currents: In the environment and the laboratory*. Cambridge university press. pages 4
- SREENIVASAN, K. R., RAMSHANKAR, R. & MENEVEAU, C. H. 1989 Mixing, entrainment and fractal dimensions of surfaces in turbulent flows. *Proc. R. Soc. Lond. A* **421** (1860), 79–108. pages 3
- TANAHASHI, M., IWASE, S. & MIYAUCHI, T. 2001 Appearance and alignment with strain rate of coherent fine scale eddies in turbulent mixing layer. *J. Turbul.* **2** (6), 1–17. pages 2
- TOWNSEND, A. A. R. 1980 *The structure of turbulent shear flow*. Cambridge university press. pages 3
- TRITTON, D. J. 1988 *Physical fluid dynamics, Clarendon*. pages 3
- TSINOBER, A. 2009 An informal conceptual introduction to turbulence, , vol. 483. Springer. pages 3
- VINCENT, A. & MENEGUZZI, M. 1991 *The satial structure and statistical properties of homogeneous turbulence*. *J. Fluid Mech.* **225**, 1–20. pages 2
- WATANABE, T., JAULINO, R., TAVEIRA, R.R., DA SILVA, C.B., NAGATA, K. & SAKAI, Y. 2017 *Role of an isolated eddy near the turbulent/non-turbulent interface layer*. *Phy. Rev. Fluid* **2** (9), 094607. pages 4
- WATANABE, T., SAKAI, Y., NAGATA, K., ITO, Y. & HAYASE, T. 2014 *Enstrophy and passive scalar transport near the turbulent/non-turbulent interface in a turbulent planar jet flow*. *Phys. Fluids* **26** (10), 105103. pages 4
- WEISS, J. 1991 *The dynamics of enstrophy transfer in two-dimensional hydrodynamics*. *Physica D* **48** (2-3), 273–294. pages 2
- WESTERWEEL, J., FUKUSHIMA, C., PEDERSEN, J. M. & HUNT, J. C. R. 2009 *Momentum and scalar transport at the turbulent/non-turbulent interface of a jet*. *J. Fluid Mech.* **631**, 199–230. pages 3

-
- WOLF, M., LÜTHI, B., HOLZNER, M., KRUG, D., KINZELBACH, W. & TSINOBER, A.
2012 *Investigations on the local entrainment velocity in a turbulent jet. Phys. Fluids*
24 (10), 105110. pages 4

Chapter 2

Lagrangian coherent structures and entrainment near the turbulent/non-turbulent interface of a gravity current

This chapter consists of a manuscript published in Journal of Fluid Mechanics, 2019:

M. Neamtu, D. Krug, G. Haller, and M. Holzner (2019). Lagrangian coherent structures and entrainment near the turbulent/non-turbulent interface of a gravity current. *J. Fluid. Mech.*, 877(824-843), <https://doi.org/10.1017/jfm.2019.635>

Abstract: In this paper, we employ the theory of Lagrangian coherent structures for three-dimensional vortex eduction and investigate the effect of large-scale vortical structures on the turbulent/non-turbulent interface (TNTI) and entrainment of a gravity current. The gravity current is realized experimentally and different levels of stratification are examined. For flow measurements, we use a multivolume three-dimensional particle tracking velocimetry technique. To identify vortical Lagrangian coherent structures (VLCSs), a fully automated three-dimensional extraction algorithm for multiple flow structures based on the so-called Lagrangian-averaged vorticity deviation method is implemented. The size, the orientation and the shape of the VLCSs are analysed and the results show that these characteristics depend only weakly on the strength of the stratification. Through conditional analysis, we provide evidence that VLCSs modulate the average TNTI height, consequently affecting the entrainment process. Furthermore, VLCSs influence the local

entrainment velocity and organize the flow field on both the turbulent and non-turbulent sides of the gravity current boundary.

2.1 Introduction

The flow in the vicinity of the sharp interface that is widely observed to form between a turbulent flow and non-turbulent surroundings, e.g. a chimney plume issuing into quiescent air, has received considerable attention in the literature over the last decades (e.g. Dimotakis, 2000; Holzner *et al.*, 2008; da Silva *et al.*, 2014). Among others, the main motivation for these studies stems from the fact that across turbulent/non-turbulent interfaces (TNTIs), fluid is continuously incorporated into the turbulent flow, a process known as turbulent entrainment. The entrainment rate has direct bearing on mixing properties and global dynamics of the flow and is therefore of high relevance and interest in many applications, e.g. jet, wake and boundary layer flows.

To date, much research has focused on small-scale properties of the entrainment process (see e.g. Westerweel *et al.*, 2005; Holzner & Lüthi, 2011; Silva *et al.*, 2018) and it is now well established (Mathew & Basu, 2002; Westerweel *et al.*, 2009) that the process by which non-turbulent fluid initially acquires vorticity is of viscous nature, as originally envisioned by Corrsin & Kistler (1955). However, the overall entrainment rate is known to be independent of viscosity or, in other terms, of the Reynolds number (see e.g. Tritton, 1988; Tsinober, 2009). It is therefore believed that structures at larger scales act to cancel the Reynolds-number dependence of the small-scale process. That is to say, even though locally non-turbulent fluid becomes turbulent via viscous diffusion of vorticity, the overall entrainment is imposed by fluid motion at larger scales which control the surface area of the TNTI (Townsend, 1980; Sreenivasan *et al.*, 1989). Recently, Lee *et al.* (2017) used conditional analysis to show that the TNTI surface area of a turbulent boundary layer increases in the vicinity of large-scale motions (LSMs). However, a similar observation is missing for other flows, far from the wall, and at present it is not clear how the fluid motion near the TNTI is related to the vortical structures in the flow.

da Silva & dos Reis (2011) visualized the vortical structures near the TNTI of a turbulent planar jet. They suggested that the large-scale vortices “sitting” on the TNTI are mostly defining its shape. Moreover, they conclude that the characteristic vorticity jump of the TNTI, as well as its thickness, is imposed by the radial vorticity distribution of these structures.

Nevertheless, progress in our understanding of the relation between the large-scale vortical structures and TNTI has been hampered by the arbitrariness in the ‘vortex’ structure definition. Often structures are extracted based on arbitrary thresholds and based on quantities that are not invariant to a change of the system of reference, i.e. they are not objective. Newly developed Lagrangian methods (for a review, see Haller, 2015) for vortex identification constitute a promising tool to overcome this issue.

Since the initial work of Haller & Yuan (2000), the theory of Lagrangian coherent structures (LCSs) has aimed to identify vortical structures - referred hereinafter as vortical Lagrangian coherent structures VLCSs to distinguish them from other types of LCSs

- using dynamical systems approaches, overcoming the arbitrariness that characterizes the classical non-objective methods, such as Q - (Hunt *et al.*, 1988), Δ - (Chong *et al.*, 1990) and λ_2 - *criterion* (Jeong & Hussain, 1995). LCS approaches are mostly based on stretching requirements (Haller, 2015) and identify highly coherent, ‘black hole’ type material regions with high accuracy, but at substantial computational cost (see e.g. Haller & Beron-Vera, 2013; Hadjighasem & Haller, 2016).

Recently, a less computationally expensive approach has been developed that replaces the stretching-based coherence requirement with rotational coherence. This method uses a new dynamic version of the classic polar decomposition introduced in Haller (2016) and identifies the initial positions of VLCSs as tubular level surfaces of the so-called Lagrangian-averaged vorticity deviation (LAVD). Haller *et al.* (2016) identified vortical structures, using LAVD-based methods, in two-dimensional (2D) and three-dimensional (3-D) flow fields. However, as highlighted by Haller *et al.* (2016), a fully automated implementation of LAVD methods for multiple 3D coherent structures is still missing.

In the present work, we seek to implement a 3D VLCS extraction method based on the LAVD theory of Haller *et al.* (2016) and apply it to experimental data of a gravity current. The gravity current constitutes an interesting flow case for two reasons. On the one hand, it has important practical applications, e.g. river plumes, katabatic winds and oceanic overflows. On the other hand, the entrainment rate across the TNTI varies with the ratio between the buoyancy and the flow shear strengths, represented by the Richardson number, Ri . This allows us to investigate how the properties of the TNTI vary to accommodate the entrainment variation with Ri and how these properties are related to the VLCSs in the proximity of the TNTI.

The paper is organized as follows. In 2.2 we describe the experimental measurements, together with the TNTI identification and VLCSs eduction methods. Then in 2.3 we characterize the VLCSs and analyse their relationship with the TNTI and the entrainment process. The article closes with the discussion and conclusions in 2.4.

2.2 Methods

2.2.1 Experiments

The gravity current data presented here were collected using the experimental apparatus developed in Krug *et al.* (2013). This set-up is sketched in figure 2.1 and was designed to create a gravity current along the top of an inclined glass tank, which can be tilted between 0 and 90° and whose dimensions are 2 m long and 0.5 m wide and high. The gravity current was realized by the continuous injection of a light fluid (a mixture of water and ethanol) along the top wall of the tank into a denser ambient fluid (a mixture of water and sodium chloride). As outlined in detail in Krug *et al.* (2014), a proper preparation of the solutions provides the desired density difference, while keeping the same refractive index in the two solutions. The latter is a crucial requirement for optical measurement techniques. During the experiment, the flow rate of the light fluid is driven by a water pump, measured via a flowmeter and its feedback is implemented as a closed-loop control. In this way, a

constant flow rate is guaranteed throughout the entire experiment. The natural transition to turbulence of the light fluid via Kelvin-Helmholtz instabilities requires an impracticably long tank (for a discussion, see Krug *et al.*, 2013). It was therefore preferred to force the transition to turbulence at the inlet by means of a diffuser equipped with rotating flapping grids. In previous experimental studies by Krug *et al.* (2013) and Odier *et al.* (2014), it was shown that with this system the turbulence characteristics at a location sufficiently 'far' from the inlet, as in the case of the present study, are independent of the inflow turbulence. The ambient entrained fluid was gently resupplied along the bottom of the tank to replenish entrained fluid. As noted by Krug *et al.* (2013), the particular value of the flow rate of the ambient fluid does not influence the entrainment rate; however, a proper choice of it avoids large-scale recirculation within the tank.

In this paper, we present results for three different flow cases. They differ in the initial density difference between the two solutions $\Delta\rho_0$ and the tank inclination α . An overview of the flow parameters is presented in Table 2.1. To compute the inflow Reynolds number, Re_0 , and the inflow Richardson number, Ri_0 , we used the inlet height d and the mean inflow velocity U_0 . Note that the label of the flow cases designates the respective value of Ri_0 . As shown by Ellison & Turner (1959), a gravity current adjusts itself to an equilibrium Ri number that depends only on the inclination of the tank α . Recently, Negretti *et al.* (2017) demonstrated that for a gravity current at the onset of the turbulence, the equilibrium Richardson number depends also on the inflow interfacial Richardson number. Maintaining a constant inflow velocity U_0 , we varied $\Delta\rho_0$ such that the resulting flow is close to the equilibrium state near the inflow. This was guided by the numerical results of Krug *et al.* (2017b) and van Reeuwijk *et al.* (2019).

2.2.2 Measurements

Flow measurements were performed using three-dimensional particle tracking velocimetry (3D-PTV). In order to capture a large investigation volume while maintaining a fine spatial resolution, which is crucial for VLCS extraction method used here, we performed measurements using four separate 3D-PTV systems. Their individual measurement domains were then stitched together in the streamwise direction. Each 3D-PTV system consisted of one high-speed camera (Mikrotron EoSens) equipped with a four-way image splitter to mimic a classical four-camera set-up, which allowed a continuous recording of 120 s.

The light source for illumination was a diode-pumped Nd:YLF laser (Quantronix, Darwin Duo, 527 nm). As flow tracers, we used neutrally buoyant polyamide particles with a mean diameter of 100 μm (manufactured by Evonik Industries, Germany).

Each single 3D-PTV system covered an observation volume of approximately 9 cm x 9 cm x 4 cm in x (streamwise), y (wall-normal), and z (spanwise) directions, respectively. The fields of view of the individual PTV systems overlapped for approximately 2 cm to track particles continuously across the different observation volumes. The start of the measurement volume was located approximately 50 cm away from the inlet and covered roughly 31 cm in the streamwise direction (figure 2.2). For each observation volume, it was possible to track up to 3000 particles simultaneously. This corresponds to a mean interparticle distance of approximately 3.5 mm, equivalent to roughly 10η , with $\eta = (\nu^3/\epsilon)^{1/4}$ being

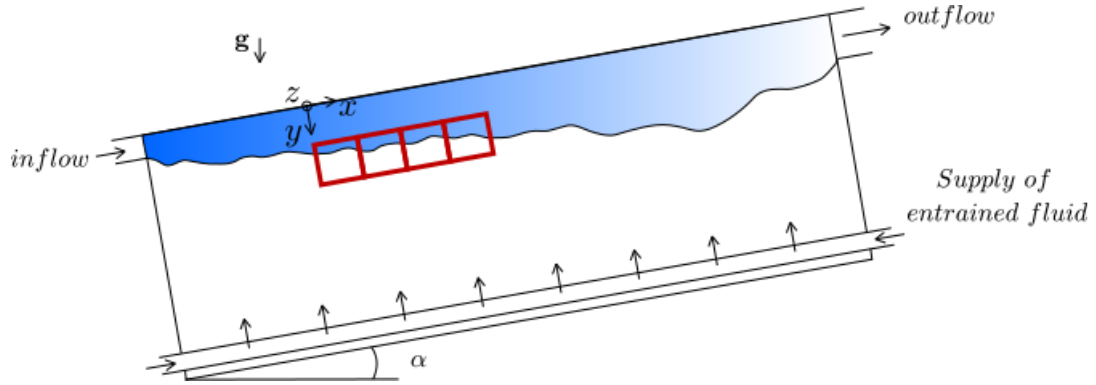


Figure 2.1: Sketch of the experimental set-up. The blue area indicates the gravity current (lighter turbulent fluid) that flows along the top wall of the tank. At the bottom, heavy fluid is resupplied to make up for the entrained flux, while mixed fluid spills out of the tank through the outlet at the top-end of the tank. The four 3D-PTV investigation domains are indicated by red rectangles.

	<i>Ri0</i>	<i>Ri10</i>	<i>Ri20</i>
$U_0[cm/s]$	10	10	10
$\Delta\rho_0[g/l]$	0	2.1	4.1
$\alpha[^\circ]$	0	10	5
$d[cm]$	5	5	5
$Re_0 = U_0d/\nu$	5000	5000	5000
$Ri_0 = g'd \sin \alpha / U_0^2$	0	0.10	0.20
$\eta[mm]$	0.23	0.29	0.31
$L[cm]$	1.00	0.96	1.00
$l_{sk}[cm]$	5.21	3.60	3.16
$u_\eta[cm/s]$	0.43	0.34	0.32
$Re_L = u'L/\nu$	152	107	102

Table 2.1: Overview of flow parameters for the three flow cases. The subscript 0 indicates the inflow parameters.

the Kolmogorov microscale, where ν is the kinematic viscosity and $\epsilon = u'^3/L$ is the local dissipation. Here, u' is the root mean square (r.m.s.) of the velocity fluctuation and L is the integral length scale of the turbulence, evaluated as the integral of the autocorrelation function of the streamwise velocity along x . The turbulence level was quantified

through the integral Reynolds number $Re_L = u'L/\nu$ (Table 2.1). As can be observed, the stable stratification reduces the turbulence level. Reference length and time scales were evaluated at a height of approximately 7 cm from the top wall, a location that is far from the wall but still sufficiently far from the strongly intermittent region close to the TNTI. The spatial resolution achieved in our experiments is not sufficiently accurate to resolve the Kolmogorov scale. However, it was considered adequate for the purposes of the present work and a suitable compromise between a large enough spatial domain and spatial resolution. As shown by Krug *et al.* (2017b), the smallest convolutions of the TNTI are of order of 10η and the TNTI geometry is therefore sufficiently captured by our measurements. The LCS extraction method explained below is based on vorticity. Given that the vorticity is somewhat under-resolved in our measurements, the extracted VLCSSs represent those of a filtered velocity field, where we neglect the effect of Kolmogorov-sized eddies. The time resolution was set to 250 Hz, which oversamples approximately 20 times τ_η , with $\tau_\eta = (\nu/\epsilon)^{1/2}$ being the Kolmogorov time scale. We applied a temporal Savitzky-Golay filter with a span of $0.5\tau_\eta$ to the velocity data. This reduced experimental noise due to position uncertainty of tracked tracer particles (Lüthi *et al.*, 2005; Wolf *et al.*, 2012).

A well-known feature of experimental particle tracking data is that particle trajectories have variable length and may be partly interrupted due to, for example optical occlusions. However, the LCS extraction method explained below requires un-interrupted trajectories. We therefore interpolated the Lagrangian velocity data on an Eulerian grid with a spacing of 5η . Subsequently we advected fluid particles numerically from these Eulerian velocity fields. A similar procedure has been applied for example by Ouellette (2012). In figure 2.2, we show samples of numerically computed fluid trajectories. To estimate the error of numerically calculated fluid particle trajectories, we used the longest measured trajectories and computed the r.m.s. distance between particle positions at the end of the trajectories. For one full flow-through time of the entire volume, we obtained an acceptable value of approximately one Kolmogorov length scale.

2.2.3 TNTI identification and local entrainment velocity

Following previous work, the identification of the TNTI was done using a threshold on the enstrophy field, $\omega^2 = \boldsymbol{\omega} \cdot \boldsymbol{\omega}$, where $\boldsymbol{\omega}$ is the vorticity vector (see e.g. Holzner *et al.*, 2008; Krug *et al.*, 2015). The TNTI location is then defined by an isosurface corresponding to a specific ω_{th}^2 threshold. In the present investigation, the threshold was fixed at $\omega_{th}^2 = 2.5s^{-2}$ just above the noise level of the data. This value is very close to those chosen by Krug *et al.* (2015) for the same flow and by Wolf *et al.* (2012) for a turbulent jet. The local velocity propagation of the TNTI surface with respect to the fluid particles, the entrainment velocity v_n , was estimated using the direct approach, presented by Wolf *et al.* (2012). In their approach, v_n is computed from

$$v_n = v_{\omega_{th}^2} - v_f, \quad (2.1)$$

where $v_{\omega_{th}^2}$ is the local velocity of TNTI and v_f is the local flow velocity. To determine $v_{\omega_{th}^2}$, we used the positions of the ω_{th}^2 isosurface at consecutive time steps. Similar to the

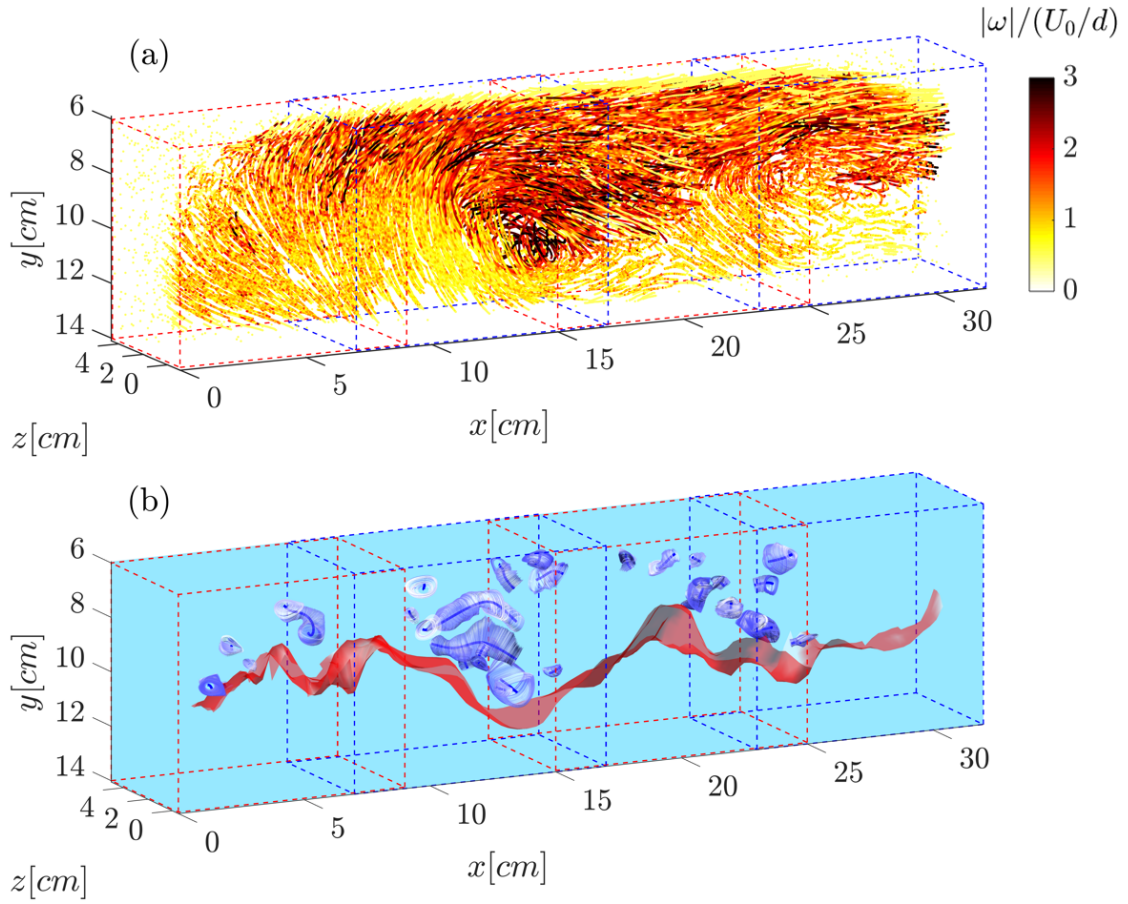


Figure 2.2: (a) 3D fluid trajectories color-coded with the norm of the vorticity for the flow case Ri_{20} . The time period shown here is equivalent to three turnover-times (defined in §2.2.4) of the largest eddies. The four alternated red and blue rectangular outlines represent the four 3D-PTV observation volumes. (b) Corresponding 3D VLCSs, represented by blue tubular surfaces (boundaries) surrounding 1D curves (centres), and the TNTI of the gravity current (red open-surface). The region above the TNTI is turbulent, whereas below the flow is irrotational.

velocity data, we also applied a temporal filter to the measured TNTI interface locations to remove occasional spurious outliers in the irrotational region.

2.2.4 VLCSs eduction

The detection of the Lagrangian coherent vortices is based on LAVD theory. We recall the definition of LAVD

$$LAVD_{t_0}^t(x_0) = \int_{t_0}^t |\boldsymbol{\omega}(x(s, x_0), s) - \bar{\boldsymbol{\omega}}(s)| ds. \quad (2.2)$$

where $\boldsymbol{\omega}$ is the vorticity along fluid trajectories, $\bar{\boldsymbol{\omega}}$ is its spatial average and $x(t, x_0)$ denotes the fluid trajectory starting at x_0 at time t_0 . According to Haller *et al.* (2016), a rotational Lagrangian coherent vortex is defined as an evolving material domain filled with a nested family of tubular surfaces of $LAVD_{t_0}^t(x_0)$ with outward-decreasing LAVD values. The boundary of the VLCS is the outermost tubular level surface, whereas its centre is the innermost member of the LAVD level-surface family. LAVD-based methods have been successfully applied in the past to 2D data of satellite oceanic velocity fields and direct numerical simulations of forced turbulence, as well as to 3D data of the ocean model ‘SOSE’ (Haller *et al.*, 2016). Prior applications of the detection method to 3D data utilized the physics and geometry of the problem to simplify the extraction of the structures. For example, the 3D vortex extracted by Haller *et al.* (2016) from the ‘SOSE’ model is a single vertically oriented structure. In the present study, we implemented this method for extraction of multiple 3D vortical structures without a prior knowledge on the physics or geometry. Our algorithm can be described as a two-step procedure. In the first step, we compute one-dimensional (1D) curves representing the centre of the structures, and in a second step, we determine the boundaries of the VLCSs.

In Haller *et al.* (2016), the centres of VLCSs are defined by 1D ridges of the LAVD field. In general, the computation of 1D ridges in three dimensions is a challenging task. In the present work, we address this task by extending the 2D ‘gradient climbing’ algorithm proposed by Mathur *et al.* (2007) to three dimensions. This algorithm uses the property that trajectories computed on the gradient field of a scalar quantity tend to accumulate along the ridges of the scalar field. The final position of these trajectories can be exploited to determine 1D candidates for ridge identification. Our ridge extraction algorithm is implemented as follows:

(i) For any initial time t_0 , we determine narrow regions in neighbourhood of ridges, where the magnitude of the $\nabla(LAVD)$ is higher than a predefined threshold and use points inside these regions as the initial conditions for computing numerically the solutions $\boldsymbol{x}_0(t)$ of the gradient dynamical system:

$$\frac{d\boldsymbol{x}_0}{dt} = \nabla LAVD_{t_0}^{t_0+T}(\boldsymbol{x}_0), \quad (2.3)$$

where t denotes the time and ∇ denotes the spatial gradient with respect to the initial position \boldsymbol{x}_0 . The solution $\boldsymbol{x}_0(t)$ takes the initial conditions to the closest ridge along the local gradient field of the LAVD.

(ii) For a given initial condition, the computation of the corresponding solution $\mathbf{x}_0(t)$ is stopped if the following two conditions hold: (a) the Hessian matrix $\nabla^2 LAVD_{t_0}^{t_0+T}(\mathbf{x}_0(t))$ has at least two negative eigenvalues (a prerequisite for a point to be on a ridge), and (b) the angle between the eigenvector $\mathbf{e}_{t_0}^{t_0+T}(\mathbf{x}_0(t))$ corresponding to the smaller-in-norm eigenvalue of the Hessian matrix $\nabla^2 LAVD_{t_0}^{t_0+T}(\mathbf{x}_0(t))$ and $\nabla LAVD_{t_0}^{t_0+T}(\mathbf{x}_0(t))$ shows no appreciable change (a sign of closeness to a nearby ridge). For large enough T , the eigenvector $\mathbf{e}_{t_0}^{t_0+T}(\mathbf{x}_0(t))$ will be approximately tangent to a ridge.

(iii) To determine the ridge candidates, we use the final positions of the solutions $\mathbf{x}_0(t)$ and select among them only points with a sufficiently close neighbouring point. To this end, we use a predefined threshold on the distance between two points.

(iv) We then group together points belonging to the same ridge and order them. To order the points, we sort them in ascending order with respect to their x , y and z coordinates and select among the three sets, the one that minimizes the curve arc length.

(v) Finally, we smooth the ridges. By parametrizing their x , y and z coordinates with respect to the arc length, we fit them with a cubic smoothing spline.

In figure 2.3, we show an example of the application of the last three steps described above. In this case, part of the points in ridge proximity are not aligned along a 1D curve (figure 2.3a). We therefore select only points with sufficiently close neighbouring points, sort them (blue curve in figure 2.3b) and apply a smoothing cubic spline (long blue curve in figure 2.3c).

After computing the centres of structures, we determined their boundaries using the following steps:

(i) For each point of a given ridge, we erect point-wise normal planes to the ridge curve and determine the in-plane outermost almost-convex LAVD contour that encircles the point. These curves are one-dimensional curves in 3D.

(ii) We then use these curves to build the VLCSs boundaries. This is achieved for every pair of nearby curves by using the *MATLAB* function *convhull* to compute the lateral surface connecting them.

In figure 2.3(c), we show the result of the application of these steps to the ridges shown in figure 2.3(b). The second step of the construction of the boundaries of the VLCS is slightly different from the one described in Haller *et al.* (2016) in that these authors use tubular level surfaces of a fixed LAVD value. We observed that tubular LAVD level surfaces typically enclosed only part of the LAVD ridges. That is, although perfectly aligned to the structure's centre and enclosed by almost-convex contours, part of the ridge remained outside of the structure (see the example in figure 2.4a), which is why we preferred to use the union of almost-convex contours.

To give an impression of how the method performs on our data, we show several VLCSs

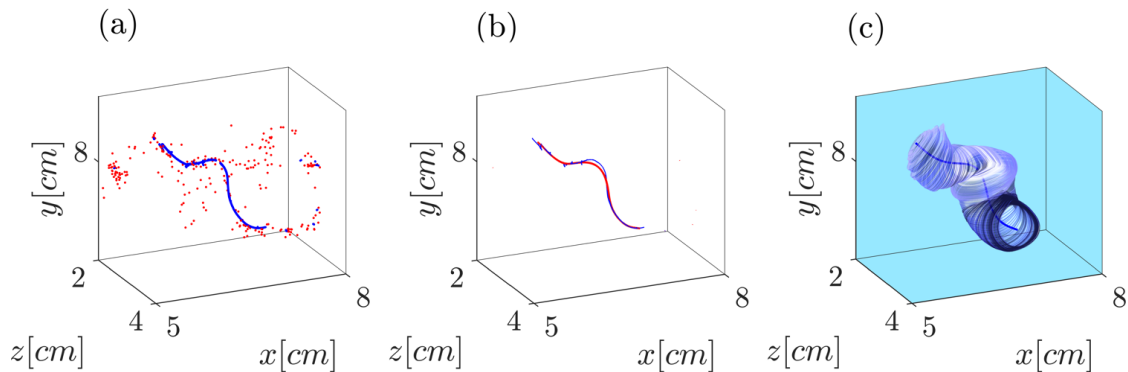


Figure 2.3: Example of VLCS extraction. In (a), the final position of the solution $\mathbf{x}_0(s)$ of equation 2.3 is shown. The blue dots are selected for the ridge construction, whereas the red ones are discarded. In (b), in blue, the connection of the points selected in (a) and its smooth fitting curve (red) are shown. The corresponding VLCS is shown in (c).

in figure 2.2(b). These are composed of tubular surfaces enclosing 1D curves (centres), in the proximity of the TNTI, represented under the form of an open surface. Here, the portion of the volume above the TNTI, where the VLCSs are located, corresponds to the turbulent part, whereas the lower side corresponds to the irrotational flow. While some of the structures lie ‘far’ from the TNTI, others are located close to it. The latter appear to shape the interface locally, as can be gleaned from figure 2.4(c). This aspect will be investigated further in §2.3.2.

In the following, we discuss the effect of the extraction time Δt on the detected VLCSs, to explain how Δt was chosen for the present data. We remark that, for short extraction times, in the limit of $\Delta t \rightarrow 0$, VLCSs tend to their Eulerian counterparts (see Haller, 2015). In this case, the material coherence is guaranteed only instantaneously, in the sense that there is no certainty that an Eulerian structure remains coherent over any observation time $\Delta t > 0$. On the contrary, for very long extraction times, no coherent structure can survive since the material coherence is limited in time for unsteady flows. For the vortical structures investigated here, the relevant temporal scale is the large eddy turnover time, which can be estimated as $t^* = L/u'$.

For the measurement set-up adopted in this work, there is a natural upper limit for Δt . This is related to the residence time of a fluid particle in the observation volume (i.e. the time spent by a particle inside the measurement volume). For the portion of the measurement volume closer to the wall, we observed that the residence time varies between one and four turnover times. In order to set the extraction time in formula (2.2), we tested different Δt values between zero (Eulerian proxy) and the maximum ($4t^*$) and investigated their effect in terms of V_{VLCS} , the average volume of a single VLCS. As can be observed in Table 2.2, V_{VLCS} is weakly influenced by the extraction time, at least in the range $t^* \leq \Delta t \leq 4t^*$. The same applies to other properties related to the size, the shape and the orientation of the VLCSs (not shown). The extraction time has a considerable impact on the number of structures that can be extracted using our measurement set-up.

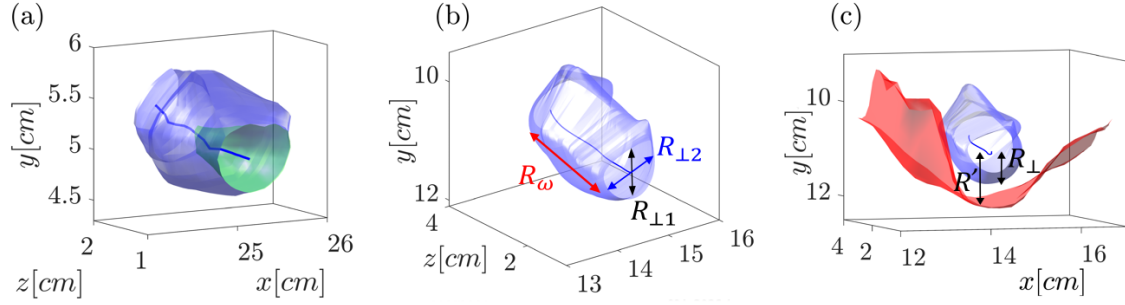


Figure 2.4: (a) VLCS reconstruction following the algorithm of Haller *et al.* (2016) (green inner-surface) and the modified algorithm introduced here (blue outer-surface). (b) Schematic of VLCS dimensions. (c) Schematic representation of R_{\perp} , VLCS (blue) cross-sectional size and R' , the distance between VLCS center and the TNTI (red).

$\Delta t/t^*$	0	1	2	3	4
V_{VLCS}/L^3	0.28	0.41	0.41	0.37	0.39

Table 2.2: Average volume of the single VLCS, V_{VLCS} , for different extraction times of the flow case Ri20.

As Δt increases the number of trajectories entirely contained in the observation volume decreases drastically. This reduces the available volume for the VLCS extraction and thus the number of structures that can be educed. As a consequence of this and observing that the extraction time appears to influence only weakly the characteristics of VLCSs, we opted to use $\Delta t = t^*$. We checked that qualitatively all results and conclusions remain the same for longer extraction times, albeit with reduced statistics.

2.2.5 VLCS size and orientation

Given the three-dimensionality of VLCSs investigated here, we defined three characteristic dimensions (figure 2.4b): one along the VLCS's rotation axis and two in the cross-section. The two cross-sectional sizes are measured as follows. At each point of the centreline of the structure, we computed the pointwise perpendicular plane to the centreline. We then evaluated the intersection between this plane and the VLCS's boundary and we fitted an ellipse to the intersection points. By taking the average of the minor and major axes of the fitted ellipses, we assigned to each VLCS: $R_{\perp 1}$ (the minor) and $R_{\perp 2}$ (the major cross-sectional size). The third dimension, R_{ω} , is given by the length of the axis of rotation. As can be observed in figure 2.2(b), some of the vortices are truncated in the rotation axis direction by the boundaries of the measurement domain. In such a case, we made an estimation of R_{ω} based on a quadratic fit. The fit was done in 1D using the average values between $R_{\perp 1}$ and $R_{\perp 2}$ along the rotation axis and using the zero crossing of the

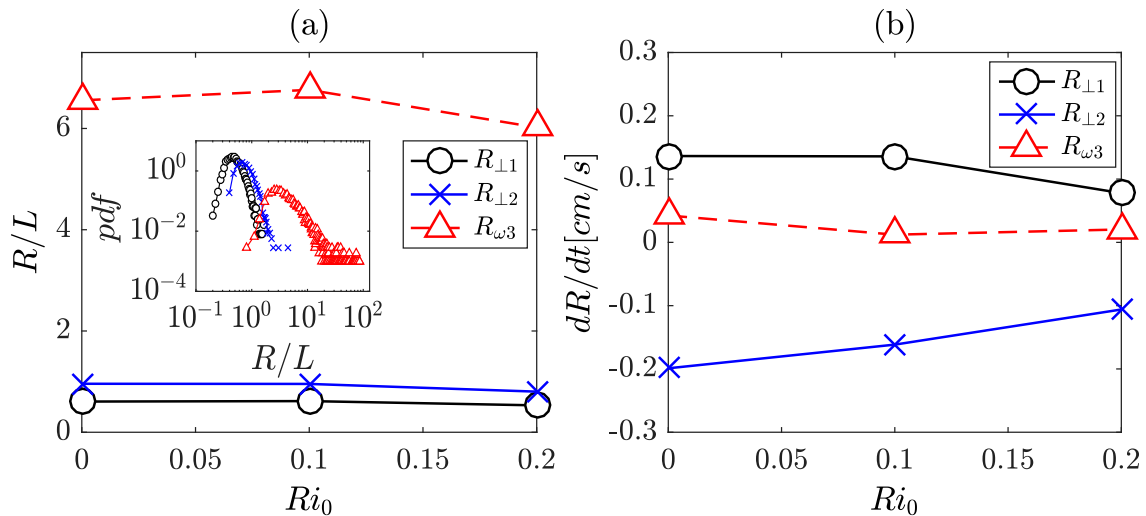


Figure 2.5: Average VLCS dimensions (a) and their growth rates (b) as a function of the initial Richardson number Ri_0 .

fitted curve. That is, we assumed that R_{ω} is finite and represented by the spatial distance between two cross-sections with zero area.

The orientation of the VLCSs was assessed by computing the average unit vector \mathbf{n} tangent to the axis of rotation.

2.3 Results

2.3.1 VLCS geometrical properties

The average size parameters of the VLCSs as a function of the initial Richardson number Ri_0 are presented in figure 2.5(a). Here, the three dimensions are normalized by the integral length scale of turbulence L , which is almost constant for all the flow cases (see Table 2.1). From figure 2.5(a), together with the observation that L is almost constant with Ri_0 , it follows that the mean dimensions of the VLCSs do not vary significantly with the stratification. The cross-sectional average sizes $R_{\perp 1}$ and $R_{\perp 2}$ are equal to approximately $0.6L$ and $0.95L$. This gives an idea of the shape of the cross-section of the structures, which on average is an ellipse with eccentricity of roughly 0.6. The average size of the third dimension, the axis of rotation R_{ω} , is of order $7L$. If the two cross-sectional sizes are ordered as a consequence of their construction, the third dimension is technically free to vary, i.e. it can be smaller or larger than $R_{\perp 1}$ and $R_{\perp 2}$. However, it is evident from figure 2.5(a) that the rotation axis of the VLCS is on average the longest one. The conclusion from this observation is that most of the structures appear to have a tubular shape. The inset in figure 2.5(a), in which we show the probability density functions (p.d.f.s) of the three size parameters for $Ri_0 = 0.2$ gives an impression about their distribution.

The VLCS dimensions presented in figure 2.5(a) are measured at the initial time t_0 of

their extraction. Solving the equation of motion between an initial time t_0 and a final time $t_0 + \delta t$ for the particles constituting the centres and the boundaries of the VLCSs, it is possible to advect the structures under the flow evolution and to evaluate their final size, and hence their growth rates, dR/dt . Here, δt was chosen to be equal to the extraction time. The growth rates of the cross-sectional sizes were evaluated computing $R_{\perp 1}$ and $R_{\perp 2}$ as described in §2.2.5 at the final time $t_0 + \delta t$. The growth rate of the axis of rotation was determined by the continuity equation, given that for a material structure $dR_{\perp 1}/dt + dR_{\perp 2}/dt + dR_{\omega}/dt = 0$. An alternative way to determine dR_{ω}/dt is to compute it by directly estimating R_{ω} as described in §2.2.5 at t_0 respectively $t_0 + \delta t$. However, we preferred the use of the continuity equation in order to avoid the inaccuracies introduced by the estimation approach of R_{ω} when the structure is not fully contained in the observation volume. In figure 2.5(b), we display the average growth rates of the VLCS dimensions as a function of Ri_0 . The growth rates corresponding to the minor axis and to the rotation axis are positive in sign, and thus these axes increase their sizes in time, whereas the growth rate of the major axis is negative. The positive growth of the rotation axis implies a predominant stretching of the vortical structures along the rotation axis. In general, the picture that emerges is that, under the flow evolution, the VLCSs are typically stretched and their cross-section tends towards a more isotropic shape compared to their initial conditions.

Further, figure 2.5(b) shows clearly that the growth rates diminish as Ri_0 increases. Thus, the stratification reduces the average VLCS compression (of the intermediate axis) and stretching (of the smallest and the rotation axis dimensions). We also note that for all Ri_0 the magnitude of average growth rates is rather small and of the order of the Kolmogorov velocity scale magnitude u_{η} (see Table 2.1), meaning that the VLCSs are on average not very strongly stretched. This result confirms our expectations, since by definition VLCSs are materially coherent structures that are not supposed to undergo very significant deformation under flow evolution.

In figure 2.6, we present the orientation of the rotation axis of the VLCSs. Specifically, we plot the joint p.d.f.s of two components of the unit vector tangent to the axis of rotation of the VLCSs. Since there is no obvious choice in which direction the tangent vector should point, we show the absolute values of the two components.

For all the flow cases, the joint p.d.f.s show a peak near $n_x \approx 0.9$. That is, the structures exhibit a preferential orientation in the streamwise direction. Also, some moderate tendency for an orientation in the spanwise direction ($n_z \approx 1$) can be observed, whereas the wall-normal orientation ($n_x \approx n_z \approx 0$) is not significant. As the Richardson number increases, the spanwise orientation gains some more importance at the expense of the streamwise one (figure 2.6c).

To assess the shape of the structures, one can build a map of R_{max}/R_{min} and R_{int}/R_{min} , with R_{max} , R_{int} and R_{min} representing, respectively, the major, intermediate and minor VLCS size. We should mention here that $R_{\perp 1}$, $R_{\perp 2}$ and R_{ω} do not coincide, respectively, with R_{min} , R_{int} and R_{max} for all the structures, although we observed in figure 2.5 that this is true on average. The map is a useful tool to determine the shape of the VLCSs. In particular, values of R_{max}/R_{min} and R_{int}/R_{min} close to the origin (1, 1) rep-

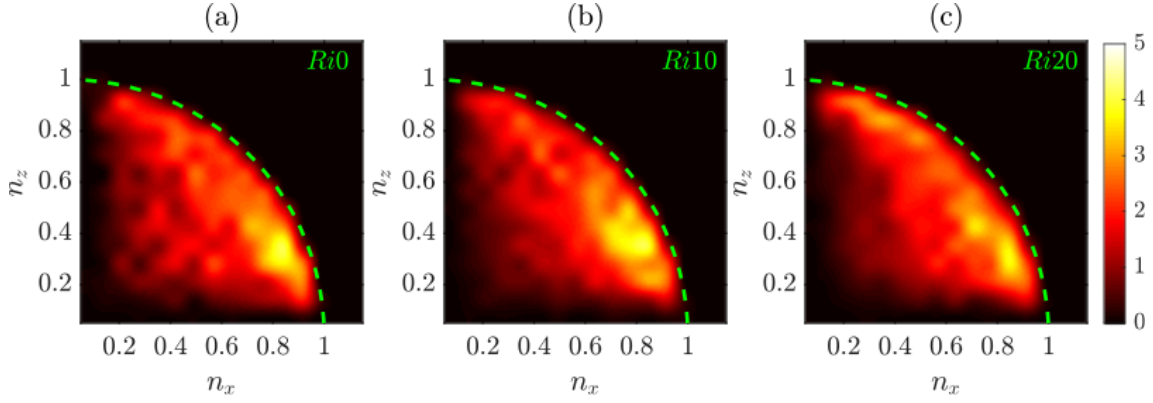


Figure 2.6: Joint p.d.f.s of VLCS orientation in the n_x - n_z plane at the initial time of the detection of the VLCSs for Ri0 (a), Ri10 (b) and Ri20 (c). The wall-normal component n_y can be estimated from the joint p.d.f.s reminding that $n_x^2 + n_y^2 + n_z^2 \approx 1$.

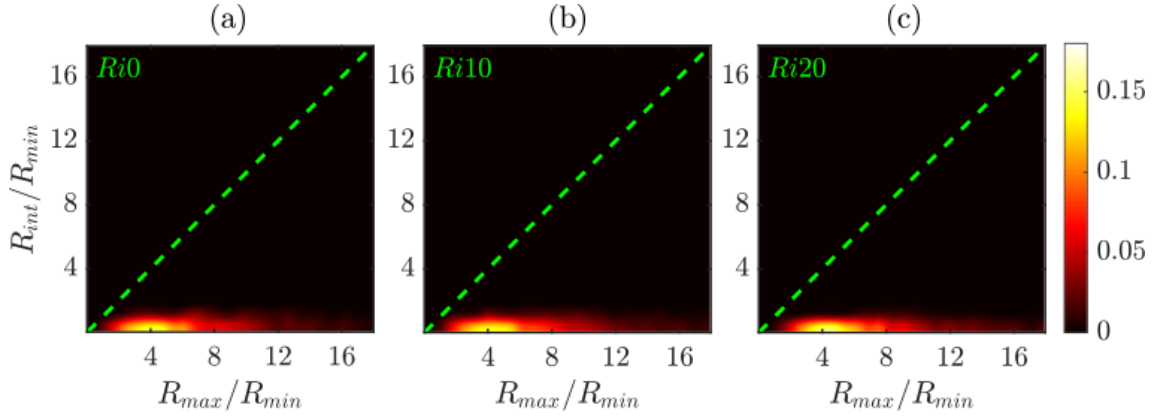


Figure 2.7: Joint p.d.f.s of VLCS shape in the R_{max}/R_{min} and R_{int}/R_{min} map at the initial time of the detection of the VLCSs for Ri0 (a), Ri10 (b) and Ri20 (c).

resent isotropic, sphere-like, structures. Values lying close to the abscissa denote tubular structures, whereas values in the proximity of the bisector denote sheet-like structures. In figure 2.7, we show joint p.d.f.s of the shape map.

For all the flow cases, there is a clear prevalence of tubular structures, which persists with increasing stratification. The three joint p.d.f.s show qualitatively similar behaviour, with a peak of $(R_{max}/R_{min}, R_{int}/R_{min})$ between $(3, 1)$ and $(7, 1)$. The peak position is consistent with figure 2.5(a), in which we showed that the average value of the rotation axis R_ω is approximately seven times larger than $R_{\perp 1}$ and $R_{\perp 2}$.

2.3.2 Interaction between the TNTI and VLCSs

In the following, we present the relationship between the TNTI and nearby VLCSs. Through conditional analysis, we provide evidence that the average interface height and

the local entrainment velocity are locally modulated by the presence of VLCSs. As observed in figure 2.2(b), part of the VLCSs are located in the proximity of the TNTI. We selected VLCSs that are ‘sufficiently’ close to the TNTI by computing the ratio r between R' , the vertical distance of the centre of the VLCS with respect to the TNTI, and R_{\perp} , the VLCS cross-sectional average radius, defined as one-half of the mean value between $R_{\perp 1}$ and $R_{\perp 2}$. A sample representation of R' and R_{\perp} can be found in figure 2.4(c). Given that in the non-turbulent region there is no vorticity, the VLCSs cannot cross the TNTI. This implies that r cannot be smaller than one. For the following conditional analysis, we selected structures with r smaller than a threshold value $r_{th} = 2.5$, which was fixed after testing different values and observing qualitatively similar results.

In a second step, for each selected structure we resampled both the instantaneous velocity field at the initial extraction time and the LAVD field around it, onto a uniform grid. For this operation, we positioned the frame of reference at the centre of the VLCS and normalized the three dimensions x , y and z around the structure with the VLCS’s cross-sectional average radius R_{\perp} . The rationale was to have a common frame of reference for all VLCSs and to compare flow fields around VLCSs of the same normalized size. Taking the average of the LAVD fields around the VLCSs, we extracted a mean representative VLCS, that is, we applied the extraction algorithm described in 2.2.4 to the average LAVD field.

Applying the same coordinate transformation to the TNTI surfaces in the proximity of the VLCSs, we computed the conditional average height of the TNTI. Moreover, at each location of the average height, we evaluated a mean local entrainment velocity $\langle v_n \rangle$. To this end, we computed the mean of instantaneous entrainment velocities near the structures. It is worth mentioning here that the high variance of the TNTI for the unstratified case Ri0 did not permit us to include this flow case in our analysis, given that the TNTI is observable in the measurement domain for a limited amount of instances, which did not allow us to obtain a meaningful statistical analysis.

In figure 2.8, we present the results for Ri10 and Ri20. The centres of the structures are represented by the continuous lines close to the origin of the frame of reference and their boundaries by tubular surfaces enclosing them. Below the structures, the open surfaces represent the average TNTI positions, which we colour-coded with the average local entrainment velocity. Around each structure, we show the direction of the average flow fields with cones that point along the velocity vector with the size representing its magnitude.

The first observation that emerges from figure 2.8 is that the average VLCS is oriented differently for the two flow cases. For Ri10, the average VLCS is oriented in the streamwise direction (figure 2.8a), whereas for Ri20, the VLCS is mainly oriented in the spanwise direction (figure 2.8d). In both flow cases, the TNTI is positioned at approximately $y/R \approx -2$ and the surface is clearly modulated by the nearby structure, having a curvature that follows that of the VLCS’s boundaries. As the stratification increases, the curvature of the TNTI is observed to reduce, which is consistent with a decrease of the mean surface area of the TNTI.

In order to reveal the effect of the orientation of the VLCSs on the shape of the TNTI,

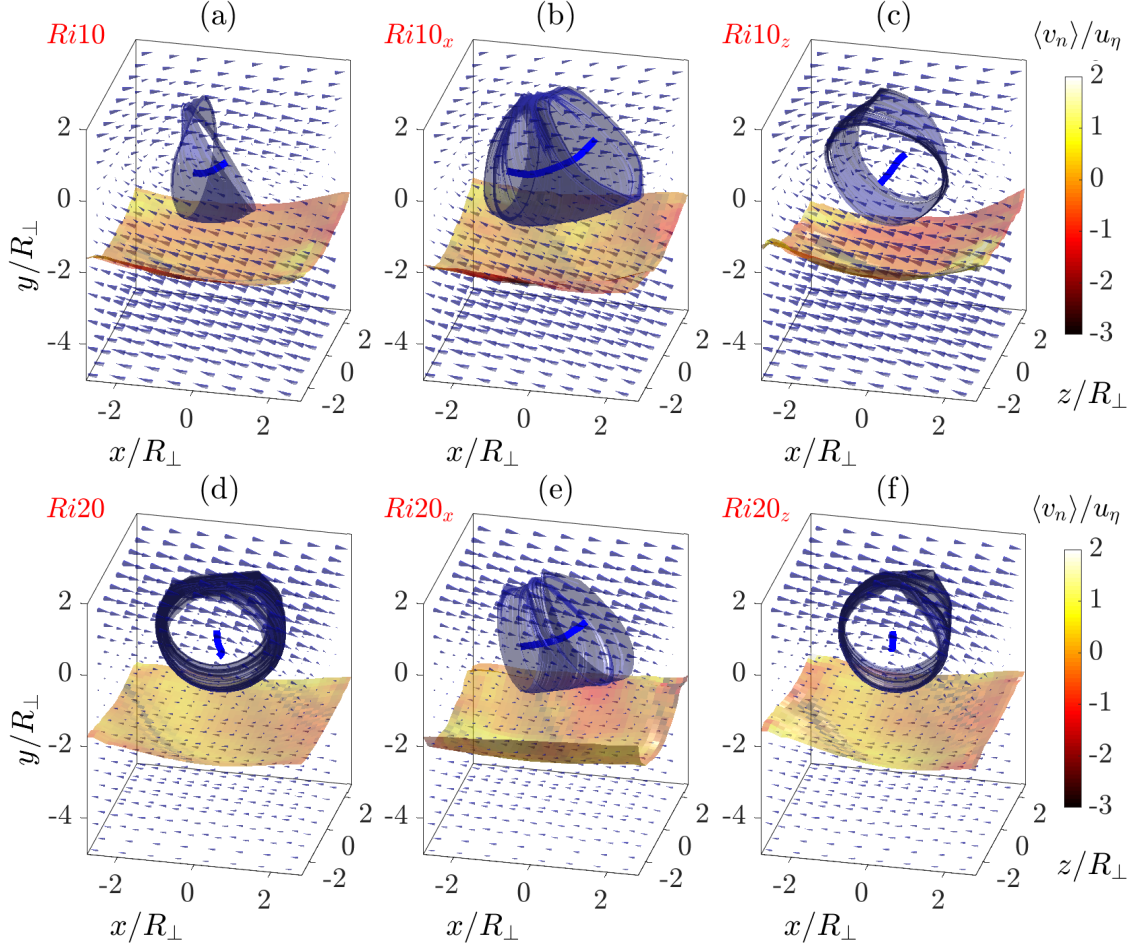


Figure 2.8: Conditional average VLCS and TNTI position for $Ri10$ (a-c) and $Ri20$ (d-f). VLCS centres are represented by the continuous blue lines and their boundaries by the tubular surfaces. The open surface is the conditioned TNTI mean position, color-coded with the average of the local entrainment velocity. The direction and the size of the vectors represent the conditional average velocity field. In the first column (a,d) the conditional analysis is made for all the structures, whereas in second (b,e) and the third column (c,f) the analysis is conditioned also on the orientation of the structures. The structures are oriented prevalently in the streamwise direction in (b) and (e), respectively in the spanwise direction in (c) and (f).

we conditioned our analysis to streamwise (figure 2.8b,e), respectively spanwise oriented structures. To this end, we compared n_x and n_z , evaluated as described in §2.2.5. For a given VLCS, if $n_x > n_z$, the structure is considered to be oriented approximately in the streamwise direction; otherwise it is considered to be oriented in the spanwise direction. From the second and third columns of figure 2.8, it appears clearly that the interface shape recalls that of the VLCS boundaries having a larger curvature in the plane orthogonal to

the rotation axis of the VLCS. Consider for example figure 2.8(e), in which we conditioned our analysis to VLCSs of Ri20 oriented in the streamwise direction. The curvature of the average TNTI is almost entirely contained in $y - z$ planes, which are orthogonal to the centre of the structure, while they are almost flat in the $x - y$ planes. Similarly, the curvature of the TNTI near the structures oriented prevalently in the spanwise direction is mostly limited to $x - z$ planes (see for example figure 2.8c). The average entrainment velocity $\langle v_n \rangle$ is shown in colour on the TNTI surface. As is common practice, we normalized v_n with the Kolmogorov velocity microscale u_η . Here, negative values of v_n represent entrainment of dense irrotational fluid from below into the lighter turbulent fluid. The spatial distribution of $\langle v_n \rangle / u_\eta$ on the TNTI shows a similar pattern for the two flow cases in figure 2.8, with higher negative values downstream with respect to the centre of the structure, that is to say, close to $x/R_\perp \approx 2$ for the VLCSs oriented in the spanwise direction. For the structures oriented in the streamwise direction, $\langle v_n \rangle / u_\eta$ has higher negative values at the sides of the VLCSs near $z/R_\perp \approx \pm 2$. Corresponding to the centre of the VLCS, for $(x/R_\perp, y/R_\perp) \approx (0, 0)$ higher or even positive values of $\langle v_n \rangle / u_\eta$ are observed (see e.g. figure 2.8d). The maximum negative value of $\langle v_n \rangle / u_\eta$ is different between the two flow conditions, diminishing (in terms of absolute value) for increasing stratification, from $\langle v_n \rangle / u_\eta \approx -1$ for Ri10 (figure 2.8a) to $\langle v_n \rangle / u_\eta \approx -0.5$ for Ri20 (figure 2.8b). As previously observed, just below the centre of the VLCSs, positive values of $\langle v_n \rangle / u_\eta$ can be noticed. The existence of regions of positive $\langle v_n \rangle / u_\eta$ (detrainment) is well known. Wolf *et al.* (2012) showed that v_n / u_η can be positive in regions with positive curvature of the TNTI (concave curvature looking to the interface from the turbulent side). As seen in figure 2.2, some of these bulges host VLCSs. As shown by others (e.g. Watanabe *et al.*, 2014; Krug *et al.*, 2017a), unconditioned averages of $\langle v_n \rangle / u_\eta$ are negative (entrainment), but instantaneous positive (detrainment) values can be observed (Mistry *et al.*, 2019). To interpret the latter, one can take into account the local entrainment velocity decomposition based on the turbulent enstrophy equation introduced by Holzner & Lüthi (2011). Based on their decomposition, $\langle v_n \rangle / u_\eta$ can be locally positive if the enstrophy destruction outweighs both the enstrophy production, which is comparatively small in the viscous superlayer, and the viscous diffusion, which is mostly positive in the viscous superlayer. This can lead to the reduction of the local enstrophy level below the threshold used for the TNTI identification.

In Table 2.3, we present the mean radius of curvature R_H of the TNTI surfaces shown in figure 2.8(a) and (d). The mean radius of curvature increases from $R_H/R_\perp = 6.6$ for Ri10 to $R_H/R_\perp = 9.4$ for Ri20. The effectiveness of the VLCSs to contort the average interface reduces with increasing stratification. Although the mean radius of curvature is not a direct measure of the surface area of TNTI, it is clear that higher values of R_H correspond to lower values of the surface area. It follows thus that the conditioned surface area of the TNTI decreases with increasing stratification, which is consistent with earlier work (see e.g. Krug *et al.*, 2015). Furthermore, in Table 2.3, we report $\overline{\langle v_n \rangle} / u_\eta$, the average of the local entrainment velocity over the TNTI surfaces in figures 2.8(a) and (d). The average of $\overline{\langle v_n \rangle} / u_\eta$ exhibits a higher value for the lower stratification passing from $\overline{\langle v_n \rangle} / u_\eta = -0.27$ for Ri10 to $\overline{\langle v_n \rangle} / u_\eta = -0.03$ for Ri20.

	<i>Ri10</i>	<i>Ri20</i>
R_H/R_\perp	6.6	9.4
$\overline{\langle v_n \rangle} / u_\eta$	-0.27	-0.03

Table 2.3: Average entrainment velocity and mean curvature of the surface of TNTI conditioned on the presence of VLCSs for *Ri10*(a) and *Ri20*(b).

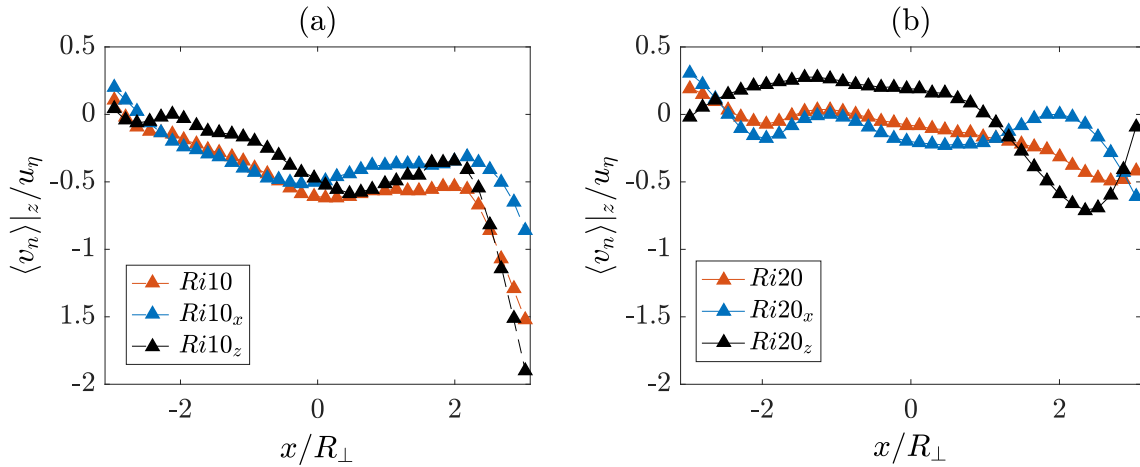


Figure 2.9: Conditioned spanwise average of the local entrainment velocity in the proximity of the VLCSs related to the figures 2.8(a,d).

In order to further illustrate how the large-scale VLCSs influence the small-scale entrainment, in figure 2.9 we show the spanwise average of $\langle v_n \rangle / u_\eta$ corresponding to figures 2.8(a,d). In both cases shown in figure 2.9, the entrainment velocity is higher in the downstream region ($x/R_\perp \approx 2$), and lower or even positive (figure 2.9b) in the proximity of the centre of the VLCS ($x/R_\perp \approx 0$). In a similar fashion to figure 2.8, we show the effect of the orientation of the structures on the entrainment velocity. For *Ri10* (figure 2.9a), it is clear that the entrainment has the same behaviour for the structures oriented both in the spanwise and in the streamwise directions. For *Ri20* (figure 2.9b), $\langle v_n \rangle|_z / u_\eta$ has considerably smaller negative values, and for the structures oriented in the spanwise direction, it has positive values around 0.2 for $x/R_\perp \approx 0$.

Finally, we analyse how VLCSs near the TNTI influence the flow around them. The impact of the VLCSs on the mean flow in the proximity of the TNTI surface is different for the two flow conditions shown in figure 2.8. For *Ri10*, no clear influence of the VLCSs can be observed (figure 2.8a). However, the spanwise-oriented structures (figure 2.8c) organize the flow both inside and outside the turbulent zone. Inside the turbulent region, the average flow field revolves around the centre of the structure, giving rise to a rotational motion, whereas outside, it deviates towards the upstream region. In the case of *Ri20*,

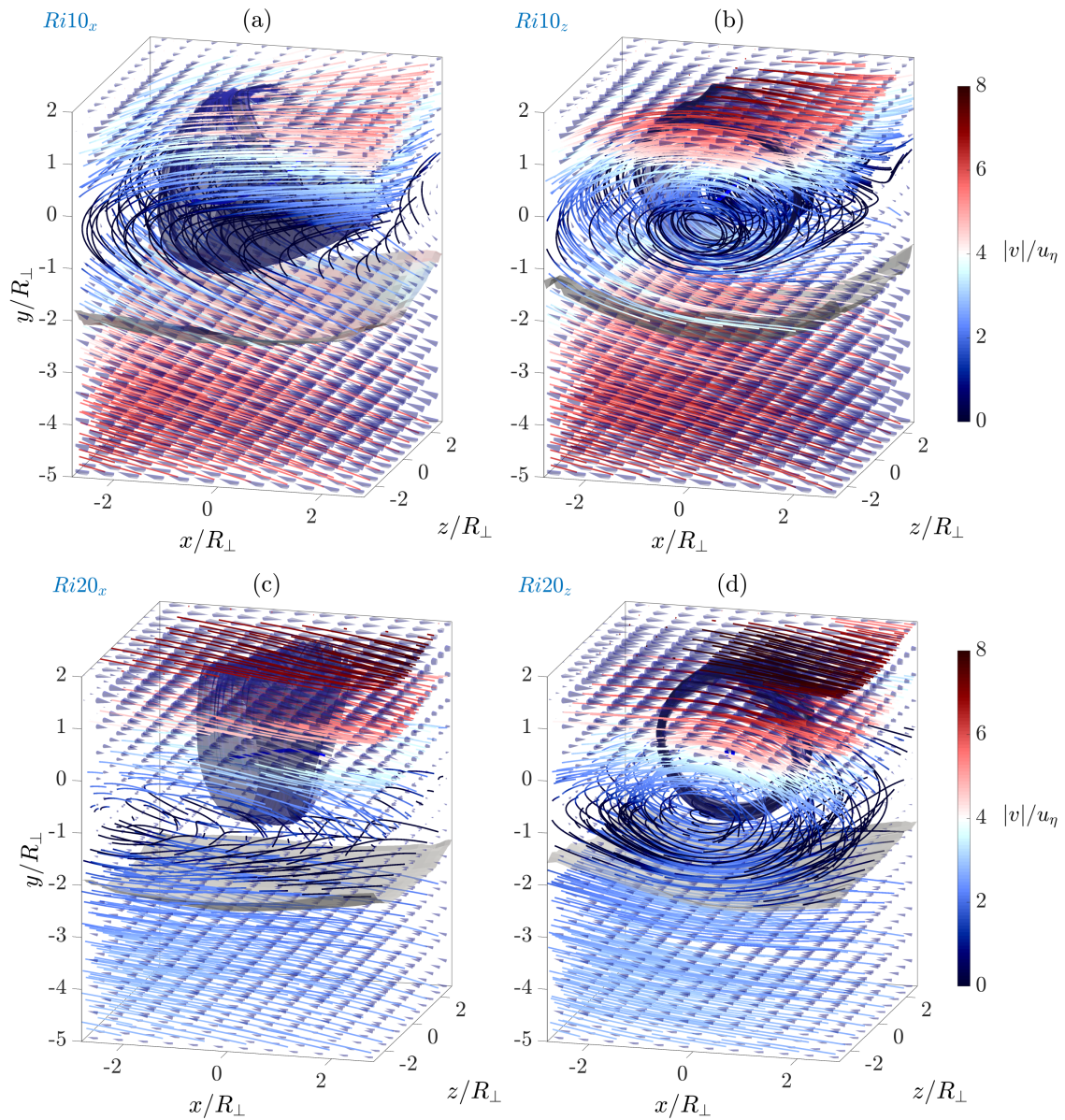


Figure 2.10: Flow visualization. Streamlines of figure 8, color-coded with the average velocity magnitude.

this behaviour can be observed without the need of conditioning on the orientation of the VLCs (figure 2.8d). However, this flow pattern is reinforced when only spanwise-oriented structures are considered (figure 2.8f).

For a clearer visualization, we display in figure 2.10 the streamlines of the average flow fields around the conditionally oriented structures shown in figure 2.8. Here, the streamlines are colour-coded with the local velocity magnitude and the TNTI is represented by the

gray transparent open surface, positioned below the VLCS. For the structures oriented in the streamwise direction (figure 2.10a,c), the streamlines in the non-turbulent zone appear to be rather horizontal, curving in the proximity of the VLCS ($y/R_{\perp} \approx 0$) and following the direction of the mean flow in the turbulent region. In both cases, the magnitude of the velocity field is higher far from the TNTI, in both the non-turbulent and the turbulent regions. When the spanwise-oriented structures are considered (figure 2.10b,d), a different flow organization arises. Outside the turbulent zone, far from the TNTI, the streamlines are again almost horizontal, similar to those close to the streamwise-oriented structures in figure 2.10(a,c). However, in the turbulent side, they follow the rotational motion induced by the VLCSs, curling up around the structures. This is evident in figure 2.10(c,d), where the swirling motion due to the presence of the structures can be clearly distinguished. For Ri20 (figure 2.10d), the streamlines follow the TNTI almost tangentially. The velocities along the streamlines forming the swirling motion inside the turbulent zone are higher for both Ri10 and Ri20 on the upper side of the structures ($y/R_{\perp} \approx \pm 1$), decreasing in the proximity of the centre of the structures and increasing again in the non-turbulent side.

2.4 Discussion and summary

In this paper, we focused on the detection and characterization of Lagrangian vortical coherent structures (VLCSs) and their influence on the turbulent/non-turbulent interface (TNTI) and entrainment of a gravity current. Using 3D-PTV data, the VLCSs were deduced by means of the so-called Lagrangian-averaged vorticity deviation (LAVD) method. The TNTI was identified using an enstrophy threshold, whereas its entrainment velocity was computed through a direct method described in Wolf *et al.* (2012).

In §2.3.1, we described the geometrical characteristics of the VLCSs. In particular, in figure 2.5(a) we observed that the average cross-sectional dimensions of the VLCSs are of the order of the integral length scale of the turbulence L . By normalizing them with L , almost no variation of their size with increasing stratification was noticed. Thus, the size of the VLCSs appeared to scale with integral length scale. A similar observation was made for the largest vortical structures near the TNTI of a turbulent jet by da Silva & dos Reis (2011). Using a low-pressure iso surface for the structure eduction, the authors found that the radius of what they call large-scale vortical structures is of the order of the Taylor microscale. Furthermore, analysing the growth rates of the dimensions of the VLCSs, we noticed that VLCSs are predominantly stretched and in time their cross-sections tend towards a rather isotropic shape. This is reminiscent of the predominant vortex stretching mechanism (Tsinober, 2000), which has been well known since, for example, the initial studies by Chong *et al.* (1990), Cantwell (1993) and Soria *et al.* (1997) on the invariants of the velocity gradient tensor. Through coarse-grained and filtered velocity gradient tensors, Meneveau (2011) demonstrated that predominant stretching is discernible also at larger flow scales that are well in the inertial range, as is in the case for the ones investigated here.

In figure 2.6 and 2.7, we showed that on average the VLCSs are of tubular shape oriented mainly in the streamwise direction. The fact that the structures are prevalently oriented

in the streamwise direction is interesting, given that, in our flow, the mean vorticity is oriented in the spanwise direction. A well-known picture in wall-bounded turbulence is that an initially spanwise-oriented vortex, formed near the wall of the boundary layer, is disturbed by an ejection event that raises part of the vortex tube to a height where the mean flow is faster. The mean flow advects this coherent mass faster than the vortex tube near the wall tilting its legs towards vertical planes, in which they are stretched by the mean shear (Kim & Adrian, 1999). We speculate that a similar mechanism may be at the base of formation of the VLCSs investigated here. In the mixing layer of the gravity current, initial vortices form via a Kelvin-Helmholtz type of mechanism and are then tilted by turbulence and the mean shear. In figure 2.6, we also noted that, as the stratification increases, more structures tend to be oriented in the spanwise direction. We associate this with the mechanism described before. Indeed, as the stratification increases, the vertical motion of the fluid is known to be reduced. This attenuates sweeps and ejections, with the consequence that the probability to observe spanwise-oriented structures may be higher. Moreover, the orientation of the structures close to the TNTI was shown to be almost horizontal. This is a consequence of the fact that the VLCSs cannot cross the interface and cannot finish or start on it. This is in line with the findings of da Silva & dos Reis (2011) in the case of a planar turbulent jet.

In §2.3.2, we investigated the interaction between large-scale VLCSs and the TNTI, with a focus on both elements constituting the entrainment process, namely, the TNTI area and the local entrainment velocity. We showed that the VLCSs modulate the TNTI height, thereby increasing the TNTI surface area. A similar observation was done by Lee *et al.* (2017) for the TNTI height of a turbulent boundary layer. Here the authors conducted a conditional analysis based on the position of LSMs, showing that the interface is locally contorted by the LSMs. In both examples, the gravity current and the turbulent boundary layer, it is demonstrated that the large-scale flow structures enhance the TNTI area thereby augmenting the entrainment flux. Moreover, we showed that the local entrainment velocity at the smaller scales of the turbulence is modulated by the large-scale VLCSs (figure 2.8). In particular, the local entrainment velocity was seen to be higher downstream with respect to the position of the VLCSs, decreasing and becoming even positive (detrainment) just beneath the centre of the structure. We hypothesize that this might be connected to the presence of the VLCS, which induces a motion tangent to the surface of the TNTI locally reducing the entrainment rate. The visualization of streamlines of the mean velocity field supports this idea. A similar remark was made by Bisset *et al.* (2002) for the instantaneous streamlines near a bulge of the TNTI of a turbulent wake. Here the authors observed that the streamlines enter it on the turbulent side (high entrainment) only in regions with a convex curvature of the surface as seen from the turbulent side (see figure 15 in Bisset *et al.*, 2002), whereas beneath the bulge the streamlines are almost horizontal (low entrainment or detrainment). In figure 2.2, we observed that part of these bulges hosts a VLCS, which is compatible with findings in Bisset *et al.* (2002). A more recent work by Mistry *et al.* (2019), which discusses the existence of instantaneous detrainment zones in a turbulent jet, further supports our observations on the detrainment near the VLCSs. Here, the authors show that similarly to our findings high detrainment

is observed when the fluid moves tangentially to the interface on both sides of the TNTI.

We are grateful for financial support from DFG priority program SPP 1881 under grant number HA 7497/1-1.

Bibliography

- BISSET, D. K., HUNT, J. C. R. & ROGERS, M. M. 2002 The turbulent/non-turbulent interface bounding a far wake. *J. Fluid Mech.* **451**, 383–410. pages 35
- CANTWELL, B. J. 1993 On the behavior of velocity gradient tensor invariants in direct numerical simulations of turbulence. *Phys. Fluids A* **5** (8), 2008–2013. pages 34
- CHONG, M. S., PERRY, A. E. & CANTWELL, B. J. 1990 A general classification of three-dimensional flow fields. *Phys. Fluids A* **2** (5), 765–777. pages 17, 34
- CORRSIN, S. & KISTLER, A. L. 1955 Free-stream boundaries of turbulent flows . pages 16
- DIMOTAKIS, P. E. 2000 The mixing transition in turbulent flows. *J. Fluid Mech.* **409**, 69–98. pages 16
- ELLISON, T. H. & TURNER, J. S. 1959 Turbulent entrainment in stratified flows. *J. Fluid Mech.* **6** (3), 423–448. pages 18
- HADJIGHASEM, A. & HALLER, G. 2016 Geodesic transport barriers in jupiter’s atmosphere: A video-based analysis. *SIAM Rev.* **58** (1), 69–89. pages 17
- HALLER, G. 2015 Lagrangian coherent structures. *Annu. Rev. Fluid Mech.* **47**, 137–162. pages 16, 17, 24
- HALLER, G. 2016 Dynamic rotation and stretch tensors from a dynamic polar decomposition. *J. Mech. Phys. Solids* **86**, 70–93. pages 17
- HALLER, G. & BERON-VERA, F. J. 2013 Coherent lagrangian vortices: The black holes of turbulence. *J. Fluid Mech.* **731**. pages 17
- HALLER, G., HADJIGHASEM, A., FARAZMAND, M. & HUHN, F. 2016 Defining coherent vortices objectively from the vorticity. *J. Fluid Mech.* **795**, 136–173. pages 17, 22, 23, 25

- HALLER, G. & YUAN, G. 2000 Lagrangian coherent structures and mixing in two-dimensional turbulence. *Physica D* **147** (3-4), 352–370. pages 16
- HOLZNER, M., LIBERZON, A., NIKITIN, N., LÜTHI, B., KINZELBACH, W. & TSINOBER, A. 2008 A lagrangian investigation of the small-scale features of turbulent entrainment through particle tracking and direct numerical simulation. *J. Fluid Mech.* **598**, 465–475. pages 16, 20
- HOLZNER, M. & LÜTHI, B. 2011 Laminar superlayer at the turbulence boundary. *Phys. Rev. Lett.* **106** (13), 134503. pages 16, 31
- HUNT, J. C. R., WRAY, A. A. & MOIN, P. 1988 Eddies, streams, and convergence zones in turbulent flows . pages 17
- JEONG, J. & HUSSAIN, F. 1995 On the identification of a vortex. *J. Fluid Mech.* **285**, 69–94. pages 17
- KIM, K. C. & ADRIAN, R. J. 1999 Very large-scale motion in the outer layer. *Phys. Fluids* **11** (2), 417–422. pages 35
- KRUG, D., CHUNG, D., PHILIP, J. & MARUSIC, I. 2017a Global and local aspects of entrainment in temporal plumes. *J. Fluid Mech.* **812**, 222–250. pages 31
- KRUG, D., HOLZNER, M., LÜTHI, B., WOLF, M., KINZELBACH, W. & TSINOBER, A. 2013 Experimental study of entrainment and interface dynamics in a gravity current. *Exp. Fluids* **54** (5), 1530. pages 17, 18
- KRUG, D., HOLZNER, M., LÜTHI, B., WOLF, M., KINZELBACH, W. & TSINOBER, A. 2015 The turbulent/non-turbulent interface in an inclined dense gravity current. *J. Fluid Mech.* **765**, 303–324. pages 20, 31
- KRUG, D., HOLZNER, M., LÜTHI, B., WOLF, M., TSINOBER, A. & KINZELBACH, W. 2014 A combined scanning ptv/lif technique to simultaneously measure the full velocity gradient tensor and the 3d density field. *Meas. Sci. Technol.* **25** (6), 065301. pages 17
- KRUG, D., HOLZNER, M., MARUSIC, I. & VAN REEUWIJK, M. 2017b Fractal scaling of the turbulence interface in gravity currents. *J. Fluid Mech.* **820**. pages 18, 20
- LEE, J., SUNG, H. J. & ZAKI, T. A. 2017 Signature of large-scale motions on turbulent/non-turbulent interface in boundary layers. *J. Fluid Mech.* **819**, 165–187. pages 16, 35
- LÜTHI, B., TSINOBER, A. & KINZELBACH, W. 2005 Lagrangian measurement of vorticity dynamics in turbulent flow. *J. Fluid Mech.* **528**, 87–118. pages 20
- MATHEW, J. & BASU, A. J. 2002 Some characteristics of entrainment at a cylindrical turbulence boundary. *Phys. Fluids* **14** (7), 2065–2072. pages 16

- MATHUR, M., HALLER, G., PEACOCK, T., RUPPERT-FELSOT, J. E. & SWINNEY, H. L. 2007 Uncovering the lagrangian skeleton of turbulence. *Phys. Rev. Lett.* **98** (14), 144502. pages 22
- MENEVEAU, C. 2011 Lagrangian dynamics and models of the velocity gradient tensor in turbulent flows. *Annu. Rev. Fluid Mech.* **43**, 219–245. pages 34
- MISTRY, D., PHILIP, J. & DAWSON, J. R. 2019 Kinematics of local entrainment and detrainment in a turbulent jet. *J. Fluid Mech.* **871**, 896–924. pages 31, 35
- NEGRETTI, M. E., FLÒR, J. B. & HOPFINGER, E. J. 2017 Development of gravity currents on rapidly changing slopes. *J. Fluid Mech.* **833**, 70–97. pages 18
- ODIER, P., CHEN, J. & ECKE, R. E. 2014 Entrainment and mixing in a laboratory model of oceanic overflow. *J. Fluid Mech.* **746**, 498–535. pages 18
- OUELLETTE, N. T. 2012 On the dynamical role of coherent structures in turbulence. *C. R. Phys.* **13**, 866–877. pages 20
- VAN REEUWIJK, M., HOLZNER, M. & CAULFIELD, C. P. 2019 Mixing and entrainment are suppressed in inclined gravity currents. *J. Fluid Mech.* **873**, 786–815. pages 18
- DA SILVA, C. B., HUNT, J. C. R., EAMES, I. & WESTERWEEL, J. 2014 Interfacial layers between regions of different turbulence intensity. *Annu. Rev. Fluid Mech.* **46**, 567–590. pages 16
- DA SILVA, C. B. & DOS REIS, R. J. N. 2011 The role of coherent vortices near the turbulent/non-turbulent interface in a planar jet. *Phil. Trans. R. Soc. A* **369** (1937), 738–753. pages 16, 34, 35
- SILVA, T. S., ZECCHETTO, M. & DA SILVA, C. B. 2018 The scaling of the turbulent/non-turbulent interface at high reynolds numbers. *J. Fluid Mech.* **843**, 156–179. pages 16
- SORIA, J., OOI, A. & CHONG, M. S. 1997 Volume integrals of the qa-ra invariants of the velocity gradient tensor in incompressible flows. *Fluid Dyn. Res.* **19** (4), 219–233. pages 34
- SREENIVASAN, K. R., RAMSHANKAR, R. & MENEVEAU, C. H. 1989 Mixing, entrainment and fractal dimensions of surfaces in turbulent flows. *Proc. R. Soc. Lond. A* **421** (1860), 79–108. pages 16
- TOWNSEND, A. A. R. 1980 *The structure of turbulent shear flow*. Cambridge university press. pages 16
- TRITTON, D. J. 1988 *Physical fluid dynamics, Clarendon.* pages 16
- TSINOBER, A. 2000 *Vortex stretching versus production of strain/dissipation. Turbulence Structure and Vortex Dynamics pp. 164–191.* pages 34

-
- TSINOBER, A. 2009 An informal conceptual introduction to turbulence, , vol. 483. Springer. pages 16
- WATANABE, T., SAKAI, Y., NAGATA, K., ITO, Y. & HAYASE, T. 2014 *Enstrophy and passive scalar transport near the turbulent/non-turbulent interface in a turbulent planar jet flow*. *Phys. Fluids* **26** (10), 105103. pages 31
- WESTERWEEL, J., FUKUSHIMA, C., PEDERSEN, J. M. & HUNT, J. C. R. 2005 *Mechanics of the turbulent-nonturbulent interface of a jet*. *Phys. Rev. Lett.* **95** (17), 174501. pages 16
- WESTERWEEL, J., FUKUSHIMA, C., PEDERSEN, J. M. & HUNT, J. C. R. 2009 *Momentum and scalar transport at the turbulent/non-turbulent interface of a jet*. *J. Fluid Mech.* **631**, 199–230. pages 16
- WOLF, M., LÜTHI, B., HOLZNER, M., KRUG, D., KINZELBACH, W. & TSINOBER, A. 2012 *Investigations on the local entrainment velocity in a turbulent jet*. *Phys. Fluids* **24** (10), 105110. pages 20, 31, 34

Chapter 3

Connecting the time evolution of the turbulence interface to coherent structures

This chapter consists of a manuscript accepted for publication in Journal of Fluid Mechanics, 2020:

M. Neamtu, D. Krug, J.P. Mollicone, M. van Reeuwijk, G. Haller, and M. Holzner (2020). Connecting the time evolution of the turbulence interface to coherent structures.

Abstract: The surface area of turbulent/non-turbulent interfaces (TNTIs) is continuously produced and destroyed via stretching and curvature/propagation effects. Here, the mechanisms responsible for TNTI area growth and destruction are investigated in a turbulent flow with and without stable stratification through the time evolution equation of the TNTI area. We show that both terms have broad distributions and may locally contribute to either production or destruction. On average, however, the area growth is driven by stretching, which is approximately balanced by destruction by the curvature/propagation term. To investigate the contribution of different length scales to these processes, we apply spatial filtering to the data. In doing so, we find that the averages of the stretching and the curvature/propagation terms balance out across spatial scales of TNTI wrinkles and this scale-by-scale balance is consistent with an observed scale invariance of the nearby coherent vortices. Through a conditional analysis, we demonstrate that the TNTI area production (destruction) localizes at the front (lee) edge of the vortical structures in the interface proximity. Finally, we show that while basic mechanisms remain the same, in-

creasing stratification reduces the rates at which TNTI surface area is produced as well as destroyed. We provide evidence that this reduction is largely connected to a change in the multiscale geometry of the interface, which tends to flatten in the wall-normal direction at all active length scales of the TNTI.

3.1 Introduction

In unbounded (e.g. jets, wakes, mixing layers) and semi-bounded (e.g. boundary layers) turbulent flows, a sharp and highly contorted interface separates the turbulent flow region from the non-turbulent ambient flow (Corrsin & Kistler, 1955; Dimotakis, 2000; da Silva *et al.*, 2014). Across this so-called turbulent/non-turbulent interface (TNTI), surrounding irrotational fluid is continuously incorporated into the turbulent flow. This process, known as turbulent entrainment, is of importance in many practical applications, in that it governs the spreading rate, mixing and reactions in a wide range of industrial and environmental flows (Davidson, 2015; Simpson, 1999; Murthy, 2013).

Commonly, the TNTI is identified through a threshold on a scalar quantity, such as vorticity magnitude or enstrophy (Bisset *et al.*, 2002), turbulent kinetic energy (Holzner *et al.*, 2006) or passive scalars (Westerweel *et al.*, 2005). From a local perspective, the entrained volume flux can be expressed as the product of $\langle v_n \rangle$, the average ‘local’ entrainment velocity, where $\langle \cdot \rangle$ denotes an average over the surface area of the TNTI, and A_η , the surface area of the TNTI (Sreenivasan *et al.*, 1989; Mathew & Basu, 2002). To date, it is widely accepted that A_η has a fractal shape (Sreenivasan *et al.*, 1989; de Silva *et al.*, 2013; Krug *et al.*, 2017b), that bears the multiscale properties of turbulence, while its propagation velocity relative to the fluid elements $\langle v_n \rangle$ is very slow and on the order of the Kolmogorov velocity scale (Holzner & Lüthi, 2011). Although the local propagation of the TNTI is of viscous nature, it is well-known that the overall entrainment rate is independent of viscosity (Morton *et al.*, 1956; Townsend, 1966; Tritton, 1988; Tsinober, 2009), viz. the Reynolds number. It thus follows that A_η plays a crucial role in setting the entrainment rate, canceling out the viscosity dependency of $\langle v_n \rangle$ (Townsend, 1966). To date, much of the research on the TNTI and associated entrainment process focused on vorticity transport across the TNTI (Westerweel *et al.*, 2005; Holzner & Lüthi, 2011; Silva *et al.*, 2018) and little is known about the mechanism that sets the surface area of the TNTI.

In his theoretical work, Phillips (1972) introduced an equation for the time evolution of the surface area of the TNTI (see §3.2), which demonstrated that the growth of the interface area is the result of the sum between a flow stretching term and a curvature/propagation term. Hypothesizing a constant entrainment velocity over the TNTI, he concluded that on average the curvature/propagation effect creates TNTI area along the bulges and destroys it in the valleys of the TNTI. While this is an important theoretical finding, the local entrainment velocity is known to vary significantly along the TNTI (Holzner & Lüthi, 2011; Wolf *et al.*, 2012; Watanabe *et al.*, 2014), with a predominance of negative values implying entrainment that alternate with sporadic positive values representing de-entrainment zones (Wolf *et al.*, 2012; Krug *et al.*, 2017a; Mistry *et al.*, 2019). In this work,

we evaluate locally the stretching and the curvature/propagation terms on the TNTI in order to assess their role in the time evolution of surface area of the TNTI.

In the last decade, an effort has been made to define the role of coherent structures in the entrainment process. da Silva & dos Reis (2011) used direct numerical simulation (DNS) data of a turbulent planar jet to show that the large-scale vortices near the TNTI define the shape of the interface area. Related findings were presented by Lee *et al.* (2017), who used conditional analysis to show that the surface area of the TNTI increases in the vicinity of large scales motions of a turbulent boundary layer. More recently, vortical structures near the TNTI have been shown to influence both the intensity of the local entrainment velocity and the mean curvature of the TNTI (Mistry *et al.*, 2019; Neamtu-Halic *et al.*, 2019). This suggests that vortical structures may impact the evolution of the TNTI area. Besides, it was also observed that the coherent vortices near the TNTI distort the mean flow in their proximity (Lee *et al.*, 2017; Watanabe *et al.*, 2017), which indicates that they may also influence the stretching of the TNTI. However, to date, the role of coherent flow structures on the time evolution of the TNTI area is largely unknown. Contrary to previous approaches, it is our goal to identify Eulerian vortical structures in a systematic, observer-independent fashion. To this end we detect objective (i.e. frame-independent) Eulerian coherent structures (OECSs) (Haller *et al.*, 2016; Serra & Haller, 2016) and elucidate their role on the time evolution of the TNTI area.

Due to their relevance in many geophysical scenarios, turbulent flows with stable stratification have received substantial attention from the scientific community. Examples of such flows include river plumes (MacDonald *et al.*, 2013), cloud-top mixing layers (Melado, 2010) and oceanic overflows (Legg *et al.*, 2009). For these flows, the entrainment coefficient is known to diminish with increasing ratio between buoyancy and the shear strength of flow, represented by the Richardson number Ri (Ellison & Turner, 1959). Recently, it has been demonstrated (Krug *et al.*, 2015; van Reeuwijk *et al.*, 2018) that the reduction of the entrainment coefficient with increasing Ri is associated with the decrease of both $\langle v_n \rangle$ and A_η . In particular, Krug *et al.* (2017b) showed that the reduction of A_η is caused by the decrease of its fractal scaling exponent, while the scaling range remains largely unaffected. Here, we explore how varying Ri affects the role of stretching and curvature/propagation for the time evolution of the TNTI area.

The main scope of the present work is to investigate the mechanisms that continuously produce and destroy the turbulence interface in flows with and without stable stratification with a particular regard to the role played in this process by coherent flow structures and the degree of stratification.

The analysis will be carried out using a DNSs of a temporal wall-jet and gravity currents, details of which will be presented in §3.2. This is followed by the presentation of the results in §2.3, while concluding remarks are given in §3.4.

	$\alpha(\text{deg.})$	Ri_0	Re_0	$Re_\lambda = \sqrt{15/\nu\epsilon}^{1/2}$	$N_x N_y N_z$	$L_x L_y L_z / h_0^3$
$Ri0$	–	0	3700	115	$1536^2 \times 1152$	$20^2 \times 10$
$Ri11$	10	0.11	3700	105	$1536^2 \times 1152$	$20^2 \times 10$
$Ri22$	5	0.22	3700	70	$1536^2 \times 1152$	$20^2 \times 10$

Table 3.1: Simulation parameters: N_i and L_i denote the number of grid points and the size along i -direction respectively. The subscript 0 indicates the inflow parameters. Results for Re_λ are averaged over $110 < t < 120$.

3.2 Methods

3.2.1 Direct numerical simulations

In the present paper, we use DNSs of temporal gravity currents and of a temporal wall-jet for which there is no stratification. Temporally evolving flows are ideally suited for obtaining converged statistics relatively inexpensively since they are homogeneous in wall parallel planes (van Reeuwijk *et al.*, 2018). For the simulations, we solve the Navier–Stokes equations in the Boussinesq approximation with a fourth-order accurate finite volume discretization scheme (Craske & van Reeuwijk, 2015) on a cuboidal volume of $1536 \times 1536 \times 1152$ cells. Periodic boundary conditions are applied both in y (the spanwise) and in x (streamwise) directions. In the z (vertical) direction, at the wall ($z = 0$) and at the top of the simulation domain, no slip respectively free slip velocity boundary conditions are imposed for the velocity, whereas Neumann (no-flux) boundary conditions are imposed for buoyancy. As schematically represented in figure 3.1(a), for the initial conditions (indicated by subscript 0), a uniform distribution of both the streamwise velocity u_0 and the buoyancy $b_0 < 0$ up to a height h_0 above the bottom wall is used.

The size of the domain in the z direction is $L_z = 10h_0$, whereas in x and in y directions it is $L_x = L_y = 20h_0$. In order to simulate a sloping bottom, the buoyancy vector $\mathbf{b} = b\hat{\mathbf{g}}$ is tilted at an angle α with respect to the vertical. Here b is a scalar with Schmidt number $Sc = 1$ and $\hat{\mathbf{g}} = (\sin \alpha, 0, -\cos \alpha)g$. In this way, the component $b \sin(\alpha)$ drives the flow along x , while $b \cos(\alpha)$ is causing a stable stratification in the wall-normal direction. For a more detailed discussion on the DNSs concept and numerical configuration we refer to van Reeuwijk *et al.* (2018), whereas the adequacy of the grid resolution is verified in van Reeuwijk *et al.* (2019).

The different flow cases investigated here differ in the initial Richardson number $Ri_0 = -B_0 \cos(\alpha) / u_0^2$, whereas the initial bulk Reynolds number $Re_0 = u_0 h_0 / \nu$, where ν is the kinematic viscosity, is kept constant.

To compute the time evolution of $Ri = -B_0 \cos(\alpha) / u_T^2$, we use the following top-hat

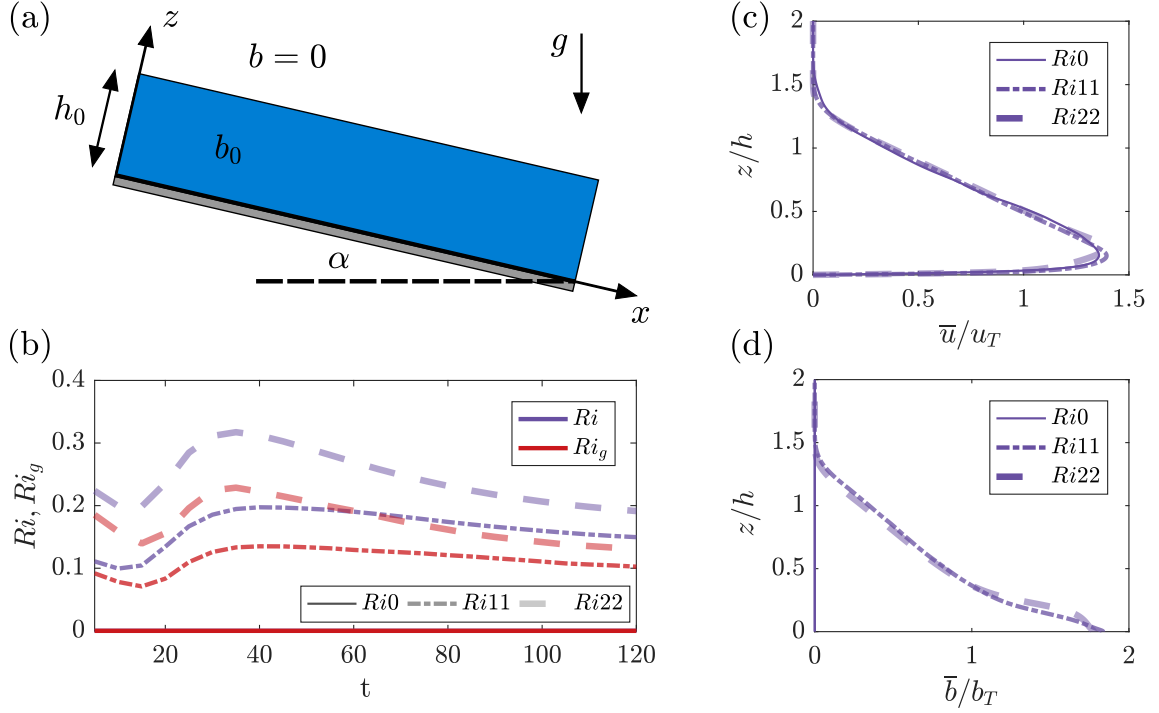


Figure 3.1: Schematic representation of the simulation setup (a). Time variation of the bulk Richardson number (purple) and the gradient Richardson number (red) (b). Vertical profiles of the mean streamwise velocity (c) and mean buoyancy (d).

definitions

$$u_T h = \int_0^\infty \bar{u} dz, \quad u_T^2 h = \int_0^\infty \bar{u}^2 dz \quad \text{and} \quad B_0 = b_T h = \int_0^\infty \bar{b} dz, \quad (3.1)$$

where B_0 is a conserved quantity in the temporal problem (van Reeuwijk *et al.*, 2018) and u is the streamwise velocity (the over-line indicates averaging in wall-parallel planes; the corresponding fluctuations are given by $u' = u - \bar{u}$). The components of the velocity vector \mathbf{u} along the y - and z -axes are denoted by v and w respectively. Table 3.1 summarizes the parameters of the simulations employed in this study. To compute Re_λ , we average the turbulent kinetic energy e and the rate of turbulent dissipation ϵ in horizontal planes, which were limited at $0.3 < z/h < 1.2$ in order to avoid the influence of the near-wall region (Krug *et al.*, 2017b). Note that the label of the flow cases indicates the value of Ri_0 . For the gravity currents (Ri_{11} and Ri_{22}), Ri_0 is varied by changing the inclination angle α while keeping the integral forcing $\sin(\alpha)B_0$ in the x -direction constant. In addition, we ran a simulation with the buoyancy term switched off, resulting in an unstratified (temporal) wall jet (Ri_0) that is driven by initial momentum only. Apart from the section §3.3.1, where the whole domain was used, results will be based on data over six independent

xz -planes, which are spaced equally in the y -direction, amounting to 250 snapshots over a period of $120h_0/u_0$. Throughout the paper, the time t is normalized by h_0/u_0 .

For a flow characterization, the time evolution of the gradient Richardson number $Ri_g = (\overline{N}/\overline{S})^2$ is shown in figure 3.1(b). In this definition, $\overline{N}^2 = d\overline{b}/dz$ is the buoyancy frequency and $\overline{S} = d\overline{u}/dz$ is the mean shear. As can be seen from the figure, after an initial transient Ri_g stabilizes and tends asymptotically towards two different constant values for the gravity current simulations. This behavior resembles that of the bulk Ri however with slightly lower magnitudes (figure 3.1b). It is important to note that for $Ri_g < 1/4$, the flow is expected to be ‘shear-dominated’ according to the classification by Mater & Venayagamoorthy (2014), which has indeed been confirmed for the simulations presented here by Krug *et al.* (2017b). Moreover, as can be seen from figure 3.1(c), when normalized with the top hat definitions, the mean streamwise velocity profiles of all the flow cases collapse on a single curve. This indicates that although there are fundamental differences between the stratified and unstratified cases, the structure of the flows is indeed very similar among all the flow cases. It is noteworthy that also the mean buoyancy profile of the gravity currents collapses on a single curve when normalized with the top hat definitions (figure 3.1d).

3.2.2 TNTI identification and local entrainment velocity

In this study, the position of the TNTI is identified through a threshold on the enstrophy field $\omega^2 = \omega_i \omega_i$, where ω_i is the vorticity vector (Bisset *et al.*, 2002; Holzner *et al.*, 2007, 2008; Silva *et al.*, 2018; Wolf *et al.*, 2012; Neamtu-Halic *et al.*, 2019). Here, the threshold is the same for all flow cases and is set to $\omega_{thr}^2 = 10^{-3}u_0^2/h_0^2$, well within the interval of possible values identified by Krug *et al.* (2017b) for DNSs with the same code and parameters as the ones presented here. By identifying the TNTI through an iso-surface of the enstrophy field, the entrainment velocity can be evaluated using the transport equation for the enstrophy (Holzner & Lüthi, 2011; Krug *et al.*, 2015). In this case v_n is given by

$$v_n = -\frac{2\omega_i\omega_j S_{ij}}{|\nabla\omega^2|} - \frac{2\nu\omega_i\nabla^2\omega_i}{|\nabla\omega^2|} - \frac{2\epsilon_{ijk}\omega_i\frac{\partial b_k}{\partial x_j}}{|\nabla\omega^2|}, \quad (3.2)$$

where ϵ_{ijk} is the Levi-Civita operator and $S_{ij} = 1/2(\partial u_i/\partial x_j + \partial u_j/\partial x_i)$ is the strain rate tensor. Throughout the paper, we make use of both fully three-dimensional (3D) data, as well as two-dimensional (2D) data from vertical planes. In the case of the 2D approach, the entrainment velocity is determined through interface tracking, with a procedure similar to the one used by Wolf *et al.* (2012) in which, v_n is computed as

$$v_n = v_I - u_n, \quad (3.3)$$

where v_I is the local normal velocity of the TNTI and $u_n = \mathbf{u}_f \cdot \mathbf{n}$, with \mathbf{u}_f , the flow velocity at the location of the TNTI and \mathbf{n} , the unit vector normal to the surface of the TNTI pointing towards the turbulent flow region. v_I is computed by tracking the position of ω_{thr}^2 -isosurfaces in time.

3.2.3 Equation for the time evolution of the TNTI area

In the present work, we investigate in detail the time evolution of the TNTI area. Initially introduced by Phillips (1972), the equation for the time evolution of a non-material infinitesimal surface element of area δA reads

$$\frac{1}{\delta A} \frac{d\delta A}{dt} = (\delta_{ij} - n_i n_j) S_{ij} + v_n \nabla \cdot \mathbf{n}, \quad (3.4)$$

where δ_{ij} is the Kronecker operator, n_i are the components of \mathbf{n} , the unit vector normal to δA , S_{ij} is the strain rate tensor and $\nabla \cdot \mathbf{n}$ is the mean curvature of the surface. In this study, \mathbf{n} points outward towards the non-turbulent side. The first term on the right hand side (rhs) of (3.4) is the *area stretch term*, whereas the second term, hereinafter referred to as *curvature/propagation term*, arises from the combined effect of curvature and propagation velocity. Even though (3.4) was initially introduced in the context of studying TNTIs, it has since received more extensive attention from the reactive flows community (Candel & Poinso, 1990; Dopazo *et al.*, 2006). In this field, the equation (3.4) is known as the *flame stretch equation*.

Since in this work, also 2D data from vertical planes is employed, we note that by passing from a 3D to a 2D approach, the TNTI reduces from a 2D surface to a 1D line and accordingly the symbol A is substituted with the symbol l for the length of a line element. In this case, the 1D analog of (3.4) reads

$$\frac{1}{\delta l} \frac{d\delta l}{dt} = (\delta_{ij} - n_i n_j) S_{ij} + v_n \nabla \cdot \mathbf{n}, \quad (3.5)$$

where \mathbf{n} is the 2D unit vector normal to the segment δl and S_{ij} is the 2D strain rate tensor.

3.2.4 Coherent flow structures extraction

For observer-independent vortical structure identification, we employ the recently developed instantaneous vorticity deviation (IVD) technique of Haller *et al.* (2016). Derived by Haller (2016) from a new, dynamic version of the classic polar decomposition, the IVD field represents an intrinsic material rotation rate in the fluid. Specifically, the IVD field, defined by the normed deviation of the vorticity vector $\boldsymbol{\omega}(\mathbf{x}, t)$ from its spatial mean $\bar{\boldsymbol{\omega}}(t)$ over an evolving fluid mass, i.e., by the formula

$$IVD(\mathbf{x}, t) = |\boldsymbol{\omega}(\mathbf{x}, t) - \bar{\boldsymbol{\omega}}(t)| \quad (3.6)$$

provides an observer-independent (objective) local angular velocity for each point of the fluid mass. Outermost tubular surfaces of the IVD, therefore, enable the identification of OECSs in an observer-independent manner, as required for experimentally reproducible coherent structure extraction (Haller, 2015). To find vortical OECSs in our data set, we

use the extraction algorithm developed in Neamtu-Halic *et al.* (2019), applied here to the IVD field. In this case, the center of the vortical structure is represented by a codimension-2 line that is the concatenation of local maxima of the IVD in planes perpendicular to the line itself, whereas the boundary of the structure is the union of the outermost almost-convex iso-contours of IVD encircling the local maxima in planes perpendicular to the center-line.

When 2D data from vertical planes is considered, a 2D OECS results from the intersection of a 3D structure with the plane itself. In this case we select only those OECSs with a limited intersection angle with respect to the normal unit vector of the plane. To this end, we impose an upper limit to the ratio between the two eigenvalues of the Hessian of IVD at the location of IVD maxima. The rationale behind this selection is based on the fact that most of the dynamics of tubular vortical structures happens in planes perpendicular to the center-line of the structure.

3.3 Results

3.3.1 Time evolution of the TNTI area

A visualization of the TNTI in a sub-domain of the gravity current for the *Ri*11 flow case at $t = 100$ is shown in figure 3.2. Here, the TNTI is color-coded with the terms of (3.4). In equation (3.4), positive values of the terms on the right-hand side contribute to the production of surface area of the TNTI, whereas negative values promote its destruction. As can be seen from figure 3.2(a-f), both $(\delta_{ij} - n_i n_j)S_{ij}$ and $v_n \nabla \cdot \mathbf{n}$ act to produce and destroy the TNTI area. In particular, $(\delta_{ij} - n_i n_j)S_{ij}$ is mainly positive at the leading edges (figure 3.2b) and negative at the trailing edges of the bulges of the TNTI (figure 3.2c).

Conversely, $v_n \nabla \cdot \mathbf{n}$ is particularly active in the valleys of the interface (see e.g. figure 3.2(e) and 3.2(f) and the zoom of figure 3.2(e)), where strong negative values can be observed. This is expected, given that the valleys of the TNTI are regions with high curvature. Moreover, $v_n \nabla \cdot \mathbf{n}$ appears to have positive values on the bulges, but at a lower intensity as compared to the valleys. The sum of the two terms, which describes the time evolution of a non-material infinitesimal element of area δA , is mostly dominated by $(\delta_{ij} - n_i n_j)S_{ij}$ on the bulges and by $v_n \nabla \cdot \mathbf{n}$ in the valleys (see figure 3.2h and i). Interestingly, we note that the sign of the patches, especially for $(\delta_{ij} - n_i n_j)S_{ij}$ and $1/\delta A \cdot d(\delta A)/dt$, seems to correlate with the geometry of the bulges.

From figure 3.2, there appears to be a spatial organization of the terms in equation (3.4) with respect to the TNTI bulges. Neamtu-Halic *et al.* (2019) showed that TNTI bulges are populated by OECSs. In figure 3.3, we show part of the OECSs extracted from a subvolume of the flow field shown in figure 3.2.

Here, the OECSs are composed by tubular surfaces, that constitute the boundaries of the structures. These surfaces enclose 1D-curves, which represent the center of the structures. In addition to the OECSs, we also display the nearby TNTI (yellow transparent open-surface) along with a vertical xz -plane (at $y = 9.75$) color-coded with intensity of the

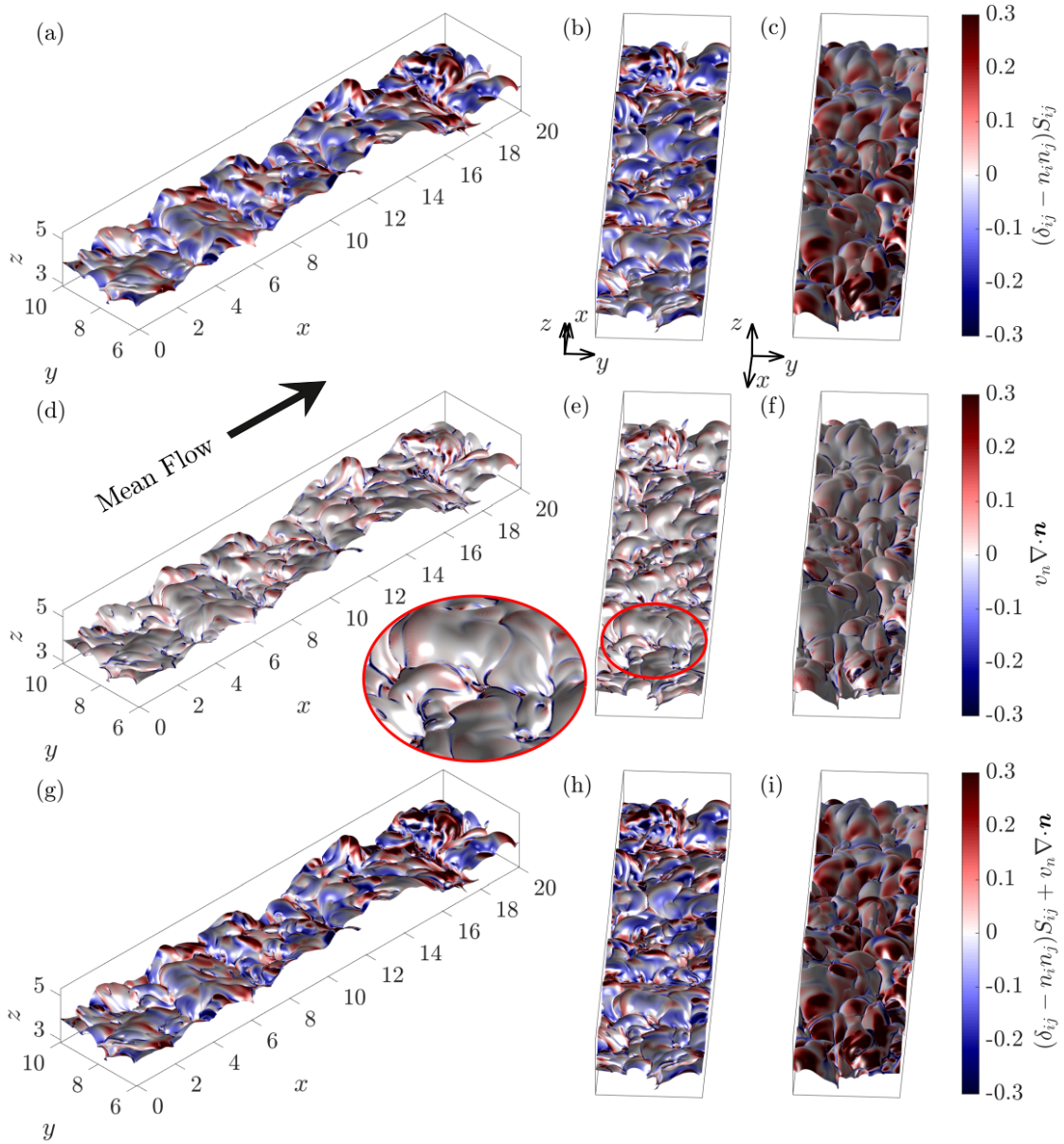


Figure 3.2: Visualization of the stretching term (a-c), curvature/propagation term (d-f) and the time evolution of a non-material infinitesimal element of area δA , $1/\delta A \cdot d(\delta A)/dt$ (g-h) of the TNTI for different view angles as captured from a snapshot of the *Ri11* flow case at $t = 100$. The black arrow indicates the mean flow direction.

IVD. As observed in Neamtu-Halic *et al.* (2019), most of the bulges are filled with OECSs that appear to shape the nearby TNTI. To investigate the local effect of the OECSs on the TNTI area production/destruction, we use the conditional analysis of Neamtu-Halic *et al.*

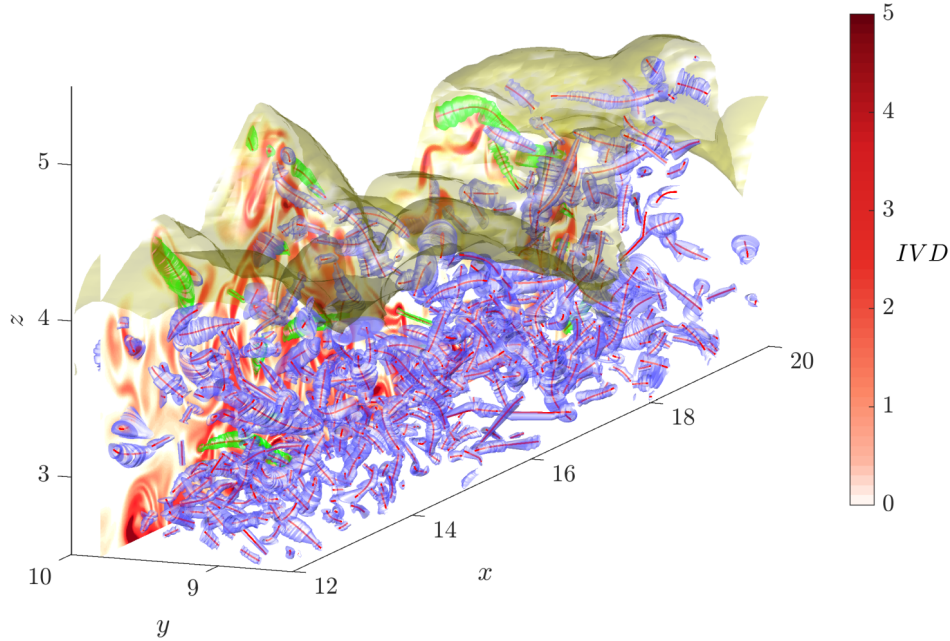


Figure 3.3: Visualization of the OECSs and the TNTI from *Ri11* at $t = 100$. The OECSs are represented by blue tubular surfaces (boundaries) surrounding one-dimensional curves (centers), whereas the TNTI is represented by the yellow open-surface. The region above the TNTI is irrotational, whereas below the surface, the flow is turbulent. The OECSs with green boundaries cross the vertical plane at $y = 9.75$ almost perpendicularly. On the vertical plane at $y = 9.75$ the IVD field is shown in red contourplot.

(2019), and explore the impact of the coherent structures on $(\delta_{ij} - n_i n_j)S_{ij}$ and $v_n \nabla \cdot \mathbf{n}$.

To simplify the analysis and manage the computational cost, we perform the subsequent analysis in 2D. Using the selection criterion described in §3.2.4, in figure 3.3, we highlight the 3D OECSs (green boundaries) that are considered for the further 2D analysis in the case of the vertical plane at $y = 9.75$.

Before proceeding, the accuracy of the 2D approach as compared to the 3D approach is addressed in terms of probability density functions (PDFs) of the three terms of (3.4). In figure 3.4, we show the results for the *Ri11* flow case. As can be seen from the figure, in all three PDFs, the two approaches provide very similar results.

In general, the PDF of the stretching term (figure 3.4a) has a higher positive tail and the overall distribution is slightly shifted towards positive values. Conversely, the PDF of the curvature/propagation term (figure 3.4b) has a higher negative tail and has a strong peak at $v_n \nabla \cdot \mathbf{n} = 0$. Moreover, the variance of the two aforementioned PDFs is different. In fact, the PDF of the curvature/propagation term presents a much narrower distribution as compared to the PDF of the stretching term. The PDF of the sum of the two terms (figure 3.4c) shows characteristics of the PDFs of both $(\delta_{ij} - n_i n_j)S_{ij}$ and $v_n \nabla \cdot \mathbf{n}$, in that

it has a positive peak and a slightly higher negative tail.

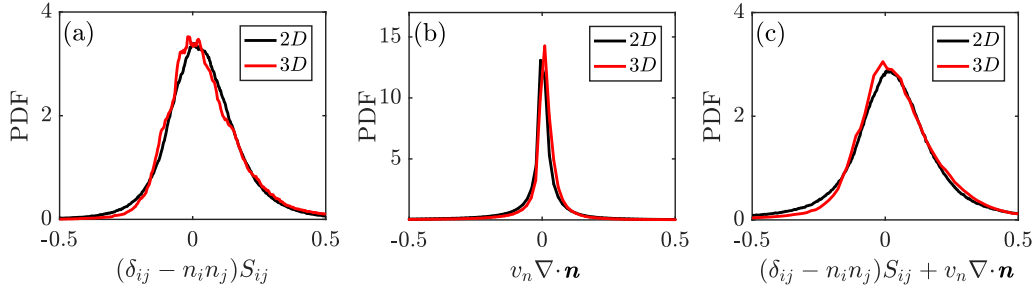


Figure 3.4: PDFs of stretching (a) and curvature/propagation terms (b) and their sum (c) from 2D (black) and 3D data (red) for $Ri11$.

3.3.2 Time evolution of the TNTI area: a 2D approach

In the following, only results from 2D data are presented. In figure 3.5, we show the time evolution of the spatial averages of the terms in (3.4) for each of the flow cases. Note that, $1/\delta l \cdot d(\delta l)/dt$ can be computed locally as a sum of $(\delta_{ij} - n_i n_j) S_{ij}$ and $v_n \nabla \cdot \mathbf{n}$ only. However, since we consider average values over the entire box, an estimation of the average of $1/\delta l \cdot d(\delta l)/dt$ can be made by taking for δl the entire length of TNTI. This can be formalized according to

$$\left\langle \frac{1}{\delta l} \frac{d\delta l}{dt} \right\rangle = \frac{1}{\sum_l \delta l} \frac{d(\sum_l \delta l)}{dt} = \langle (\delta_{ij} - n_i n_j) S_{ij} \rangle + \langle v_n \nabla \cdot \mathbf{n} \rangle. \quad (3.7)$$

As can be seen for all the flow cases, the stretching term is positive on average and decays in time from about 0.1 at $t = 25$ to 0.01 at $t = 120$. Conversely, the curvature/propagation term is negative on average and its magnitude decays in time similar to the stretching term from about -0.1 at $t = 25$ to -0.01 at $t = 120$. We note that several turbulent time scales were tested for the scaling of these trends, namely, the Kolmogorov time scale $(\nu/\epsilon)^{1/2}$, the mean shear time scale \bar{S}^{-1} , the turbulence time scale ϵ/ϵ and the integral time scale h/u_T . However, none of these time scales were able to collapse rates in time and across Ri hinting thus at a multiscale nature of the terms in (3.4). As Ri increases, both the average stretching and curvature/propagation terms decrease. Moreover, the spatial average growth of the TNTI surface, $1/\delta l \cdot d(\delta l)/dt$, results to be very small for all the time steps between $t = 25$ and $t = 120$. That is, the two terms on the rhs of equation (3.4) approximately balance each other out for all the time steps shown in figure 3.5.

In order to understand how the two terms on the rhs of equation (3.4) balance out on average, we show in figure 3.6 the joint PDFs of all possible couples of the terms in equation (3.4) for $Ri0$ (a-c), $Ri11$ (d-f) and $Ri22$ (g-h).

The joint PDF of $(\delta_{ij} - n_i n_j) S_{ij}$ and $v_n \nabla \cdot \mathbf{n}$ (first column of figure 3.6) has a vertically elongated shape with a distinguishable horizontally elongated peak. This demonstrates that the stretching term dominates over the curvature/propagation term for small values

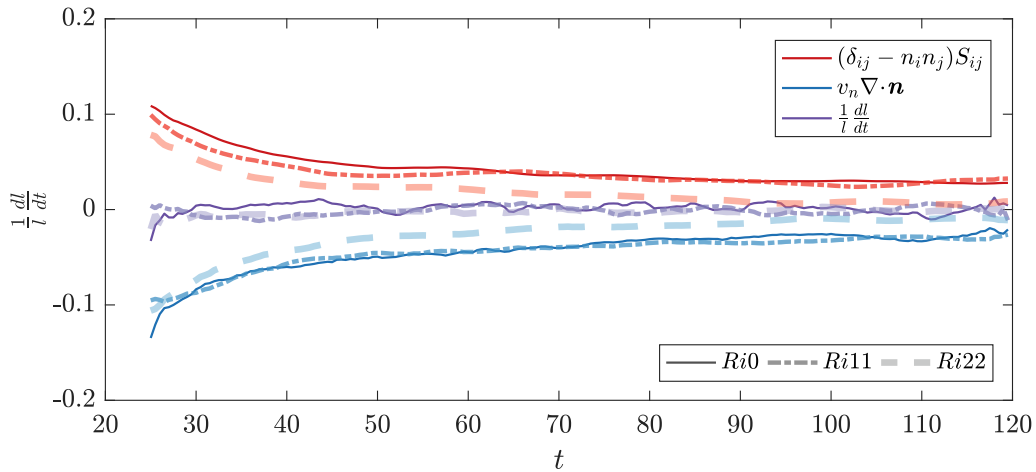


Figure 3.5: Time evolution of the spatial average of stretching term (red), curvature/propagation term (blue) and $1/\delta l \cdot d(\delta l)/dt$ (purple) for $Ri0$ (continuous line), $Ri11$ (dash-dotted line) and $Ri22$ (dashed line).

of $(\delta_{ij} - n_i n_j) S_{ij}$ and $v_n \nabla \cdot \mathbf{n}$ (between ± 0.1), whereas the curvature/propagation term has longer tails. Furthermore, the joint PDF shows higher probability for positive values of $(\delta_{ij} - n_i n_j) S_{ij}$ and negative values of $v_n \nabla \cdot \mathbf{n}$. As Ri increases the tails of the curvature/propagation term are reduced, whereas the stretching term shows a slightly broader distribution and a more centered peak. The joint PDF of $(\delta_{ij} - n_i n_j) S_{ij}$ and $1/\delta l \cdot d(\delta l)/dt$ (sum of the two terms on rhs of (3.4)) is shown in the second column of figure 3.6. A high degree of correlation between the $(\delta_{ij} - n_i n_j) S_{ij}$ and $1/\delta l \cdot d(\delta l)/dt$ can be noticed for small values (between ± 0.1), whereas for higher values the PDF is elongated in the vertical direction, a sign of weaker correlation between the two terms. Again, as Ri increases the tails of $1/\delta l \cdot d(\delta l)/dt$ reduce. The joint PDF between $v_n \nabla \cdot \mathbf{n}$ and $1/\delta l \cdot d(\delta l)/dt$ is shown in the last column of figure 3.6. In this case, the two quantities correlate very well for intense values, whereas they appear to be almost uncorrelated near origin. In conclusion, the area growth is mostly driven by the strain term for weak to moderate events that tends to produce interface area. However, the large tails of the curvature/propagation term dominate the extreme events and has a negative mean, so that on average this term counterbalances the positive stretching. As Ri increases the curvature/propagation term has a narrower distribution, whereas the peak of the stretching term tends to move closer to the origin. A physical interpretation of this latter observation is provided in §3.3.3, where we connect the interface evolution to the presence of coherent structures.

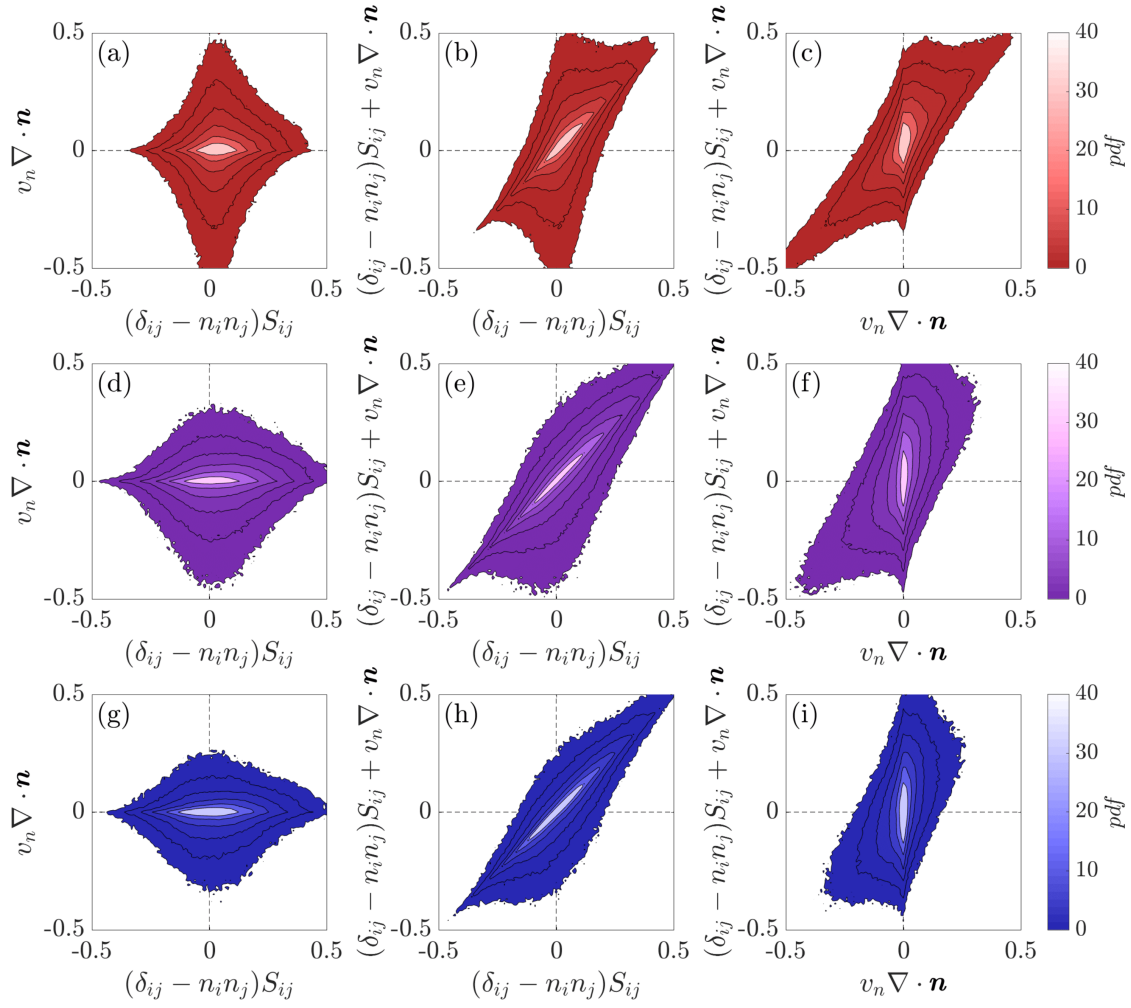


Figure 3.6: Joint PDFs of $(\delta_{ij} - n_i n_j) S_{ij}$, $v_n \nabla \cdot \mathbf{n}$ and their sum for $Ri0$ (a-c), $Ri11$ (d-f) and $Ri22$ (g-h) for $30 < t < 120$. The corresponding values of the black contour lines increase with logarithmic intervals.

Effect of the stable stratification on the production/destruction process of the TNTI area

In the following we investigate the effect of the stable stratification on the terms of (3.4). Initially, we focus on the stretching term, that in 2D can be written as:

$$(\delta_{ij} - n_i n_j) S_{ij} = (1 - n_x^2) \frac{\partial u}{\partial x} - n_x n_z \left(\frac{\partial u}{\partial z} + \frac{\partial w}{\partial x} \right) + (1 - n_z^2) \frac{\partial w}{\partial z}. \quad (3.8)$$

In figure 3.7, we show PDFs of the three components of $(\delta_{ij} - n_i n_j)$ and of the three components of S_{ij} . As can be seen, a significant effect of the stable stratification can be noticed on the three coefficients $(\delta_{ij} - n_i n_j)$ of (3.8) (figure 3.7a-c). While $(1 - n_x^2)$ shows

a higher probability for values close to unity with increasing Ri (figure 3.7a), $(1 - n_z^2)$ is seen to diminish as the stratification increases (figure 3.7c). Also, as Ri increases, $-n_x n_z$ shows a higher probability for values close to 0. These observations indicate that $n_x \rightarrow 0$ while $n_z \rightarrow 1$ as the stratification increases, that is, the interface tends to flatten with increasing Ri .

To better understand the effect of the stratification on the components of $(\delta_{ij} - n_i n_j)$ tensor, we use the fractal scaling theory for the geometry of the TNTI (Sreenivasan *et al.*, 1989). According to the theory, the length of the TNTI depends on l_i/l_o , the inner and the outer cutoffs of the scaling range and on β , the fractal scaling exponent. In their work, Krug *et al.* (2017b) showed that for gravity currents, l_i/l_o is essentially constant for $0 < Ri < 0.22$, whereas β decreases with increasing stratification. Moreover, the authors observed that the convolutions of the TNTI are anisotropic, scaling with l_{sk} in the wall-normal and with h in the streamwise direction. Based on the observation that the ratio $r = l_{sk}/h$ decreases with increasing stratification, they implemented a model for $\beta = f(r)$, that was able to reproduce the trends of the fractal scaling exponent β with increasing Ri . The model is based on a simple fractal model where in subsequent iterations line segments with length l_{n+1} are placed at distance rl_n from the center of l_n (Krug *et al.*, 2017b). Here we use this model to check quantitatively if the trends observed in figure 3.7(a-c) can also be related to the anisotropy of the interface bulges. In figure 3.7(d), we display the geometry of the modeled interface where $l_i/l_o \approx 100$, chosen according to our Reynolds number, and r has the values indicated in the caption. As can be noticed, for $Ri22$ the fluctuations of the TNTI position in the wall-normal direction are much lower as compared to the wall-jet and thus the interface tends to flatten with increasing stratification. A comparison between the fractal model and the DNS data in terms of average value of $(\delta_{ij} - n_i n_j)$ components against Ri is shown in figure 3.7(e). Notably, the model reproduces rather well the average of $(\delta_{ij} - n_i n_j)$, especially for $(1 - n_x^2)$ and $(1 - n_z^2)$, the two terms that vary more significantly with Ri . We therefore conclude that, in agreement with the model, the stratification impacts the interface geometry at all ‘active’ length scales of the TNTI between l_i and l_o .

In figure 3.7(f-h), we show PDFs of the components of the rate of strain. All three PDFs are only weakly affected by increasing stratification, which is reflected in a moderate increase of the weight of the tail and an associated decrease of the peak at small magnitudes. While in the PDFs of $\partial u/\partial x$ and $\partial w/\partial z$ the skewness reduces (figure 3.7f and h), the PDF of $\partial u/\partial z + \partial w/\partial x$ is more negatively skewed with increasing Ri . The latter is consistent with a stronger mean velocity gradient, i.e. smaller h at similar u_T , and therefore stronger $\partial u/\partial z$ at increasing Ri .

The average values of the terms in equation (3.8) against Ri are shown in figure 3.7(k). Although the PDF of $\partial u/\partial x$ presents a slightly higher negative tail, the average of $(1 - n_x^2)\partial u/\partial x$ is positive. This means that there is coupling between high values of $(1 - n_x^2)$ and positive values of $\partial u/\partial x$. As the stratification increases, $(1 - n_x^2)\partial u/\partial x$ increases slightly. The average of $-n_x n_z(\partial u/\partial z + \partial w/\partial x)$ is positive as expected from the PDFs in figure 3.7(b) and (c). As the stratification increases, $-n_x n_z(\partial u/\partial z + \partial w/\partial x)$ increases slightly at $Ri = 0.11$, to decrease afterwards at $Ri = 0.22$. In particular, the smaller

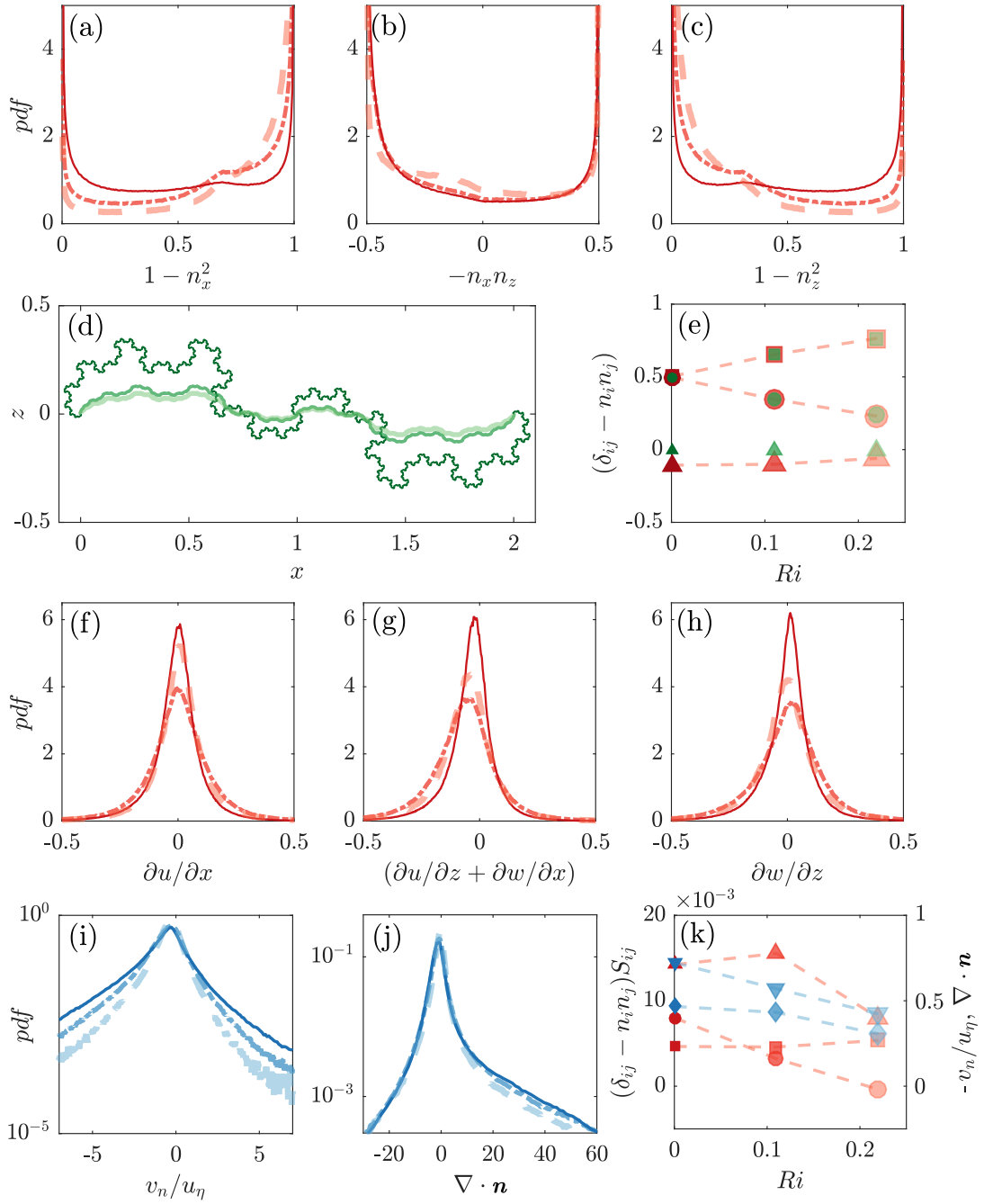


Figure 3.7: PDFs of the three components of $(\delta_{ij} - n_i n_j)$ (a-c) for $Ri0$ (continuous line), $Ri11$ (dash-dotted line) and $Ri22$ (dashed line). TNTI surface as obtained from the fractal model of (Krug *et al.*, 2017b) for $r = 0.3$ ($Ri0$), $r = 0.12$ ($Ri11$) and $r = 0.09$ ($Ri22$) (d). The thickness of the lines increases with Ri . Average value of $(1 - n_x^2)$ (squares), $-n_x n_z$ (triangles) and $(1 - n_z^2)$ (circles) from the fractal model (green) and from the DNS data (red) with $30 < t < 120$ (e). PDFs of the three rate of strain components (f-h) of the stretching term and PDFs of the entrainment velocity (i) and of the curvature of the TNTI (j) for $30 < t < 120$. Average values of $(1 - n_x^2) \partial u / \partial x$ (square symbols), $-n_x n_z (\partial u / \partial z + \partial w / \partial x)$ (red triangle symbols), $(1 - n_z^2) \partial w / \partial z$ (circles) and of $\nabla \cdot \mathbf{n}$ (blue diamonds) and $-v_n / u_\eta$ (blue triangles) against the Ri number (j).

value $-n_x n_z (\partial u / \partial z + \partial w / \partial x)$ at $Ri = 0.22$ might be related to a higher probability of $-n_x n_z = 0$ as compared to the other flow cases, given that the PDF of $\partial u / \partial z + \partial w / \partial x$ for $Ri22$ is comparable to the one of $Ri11$ and exhibits even a higher negative tail as compared to the one of $Ri0$. Also the average of $(1 - n_z^2) \partial w / \partial z$ is positive, meaning that, as for the other terms, there is a coupling of high values of $1 - n_z^2$ and positive values of $\partial w / \partial z$. As the Ri increases, $1 - n_z^2$ tends towards smaller values and the average of $(1 - n_z^2) \partial w / \partial z$ decreases.

In conclusion, most of the reduction in the stretching term of (3.4) with increasing stratification is related to a change in the components of $(\delta_{ij} - n_i n_j)$ tensor as a result of a change in the multiscale geometry of the TNTI which tends to flatten out with increasing Ri .

Furthermore, in figure 3.7 we show the impact of the stable stratification on the curvature/propagation term. As can be gleaned from the presented PDFs, the stable stratification reduces the magnitude of both v_n and $\nabla \cdot \mathbf{n}$. In particular, while the reduction of the v_n (figure 3.7i) with increasing Ri is well-documented (see e.g. Krug *et al.*, 2015; van Reeuwijk *et al.*, 2019), it can be seen from figure 3.7(j) that the stratification reduces also the probability to observe strong convex regions, associated with positive values of $\nabla \cdot \mathbf{n}$. This is not unexpected, given the changes in the geometry of the TNTI discussed above. The average values of the two terms against Ri is shown in figure 3.7(k) and as expected the magnitude of both the terms decrease on average with increasing stratification.

Multiscale nature of the production/destruction of the TNTI area

As observed in figure 3.2, the positive and the negative patches of the terms in (3.4) appear to correlate with the orientation of the TNTI bulges. Since the TNTI surface has a fractal shape, in figure 3.8 we investigate the scale dependence of the terms in (3.4). Following the procedure used in Krug *et al.* (2017b), we use a box filter to eliminate the effect of the spatial scales smaller than the size of the filter length. To find the position of the interface in the filtered field, we first convert the enstrophy field ω^2 to a binary field I , where $I = 1$ if $\omega^2 > \omega_{thr}^2$ and $I = 0$ if $\omega^2 < \omega_{thr}^2$. We then filter I according to $\tilde{f} = \int f(\mathbf{x} - \mathbf{x}') G(\mathbf{x}') d\mathbf{x}'$, where \tilde{f} is the filtered quantity and G denotes the kernel of a square box filter of width Δ . We then define the position of the filtered interface as the isocountour $I = 0.5$. Contrary to filtering the enstrophy field directly, this procedure has the advantage that it preserves the mean position of the TNTI. As highlighted by Krug *et al.* (2017b), this is a necessary condition to keep the entrained flux across scales constant. Moreover, to compute the filtered terms in equation (3.4), we apply the same filter to the streamwise and the wall-normal velocity fields and evaluate the quantities in equation (3.4) at the location of the filtered interface.

In figure 3.8, we display the time and space averages of the filtered quantities of equation (3.4) for different sizes of the filter length Δ , here normalized with the Kolmogorov length scale η . All three-flow cases shown here display a similar behavior, with decaying magnitude of the stretching and the curvature/propagation terms with increasing filter size. Initially for Δ/η smaller than ≈ 10 the decay is very slow. Conversely, for Δ/η larger than $\approx 10^2$ the magnitude of the stretching and the curvature/propagation terms

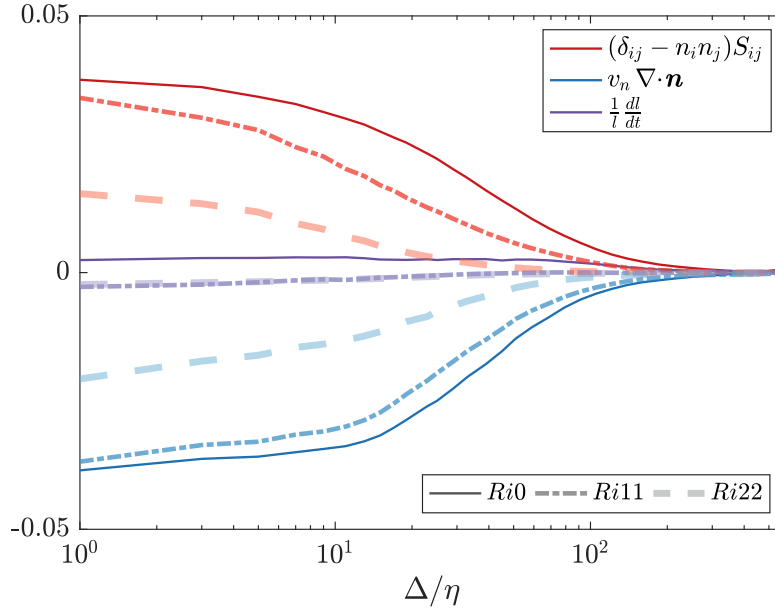


Figure 3.8: Box and time averages of space-filtered stretching term (red), curvature/propagation term (blue) and the time evolution of a non-material infinitesimal element of area δl (purple) for $30 < t < 120$.

is negligible, while for Δ/η between ≈ 10 and $\approx 10^2$ a strong reduction of the two terms can be observed. We note that the limits of the latter region are consistent with the inner ($\approx 10\eta$) and the outer ($\approx 0.6 - 0.8h$) cutoffs of the scaling range of A_η observed by Krug *et al.* (2017b). Again, as seen in figure 3.5, when Ri increases, the terms on the rhs of equation (3.4) are smaller. The sum of the two terms of (3.4), the variation of the infinitesimal area, remains constant and close to 0 for all the filter sizes. That is to say, the two terms on the rhs of equation (3.4) not only balance out overall, but this balance holds also on a scale by scale basis.

In conclusion, we observe that the difficulty on finding a time scaling for the stretching and the curvature/propagation term discussed in the context of figure 3.5 is in agreement with the results presented here, in that we showed how these terms are the result of multiscale process. They can therefore not be characterized by a single time scale.

3.3.3 Impact of OECSs on the production/destruction of TNTI area

A connection between local interface shape and nearby vortical structures was already established in Neamtu-Halic *et al.* (2019). This is confirmed in figure 3.3 where we observed that part of the bulges of the TNTI are filled with OECSs. We now examine how the area change of the TNTI is related to the nearby coherent structures.

As a first step, we focus only on the structures that shape the TNTI, that is, on the structures that are positioned ‘sufficiently’ close to the TNTI. To this end, we compare

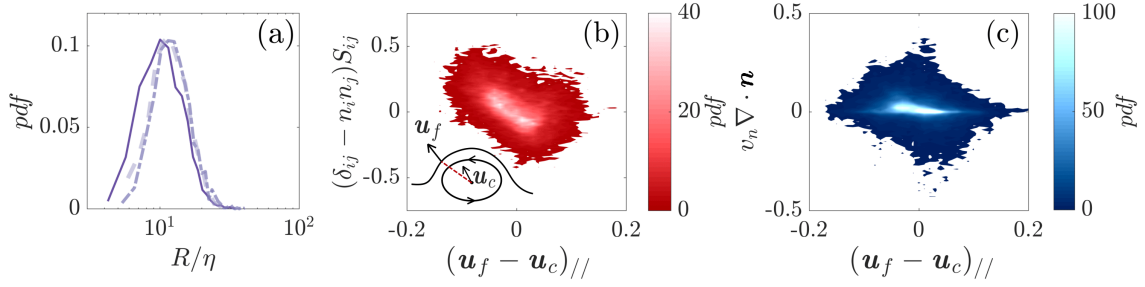


Figure 3.9: PDF of the size (a) of the structures in the proximity of the TNTI. Increasing thickness and transparency of the curves corresponds to increasing Ri . Joint PDF of the stretching (b) and curvature/propagation terms (c) with respect to the relative velocity between the OECS and the TNTI for $Ri=11$. The inset in (b) shows schematically where \mathbf{u}_f and \mathbf{u}_c are computed.

the size R of the structures with the minimum distance $\min(d)$ between the boundary of the structure and the TNTI. If the ratio $\min(d)/R$ is smaller than a threshold (here fixed at 1.5), the structure is selected and discarded otherwise. The particular value of the threshold was chosen by observing that beyond this limit, the correlation between the structure position and the local interface evolution weakens considerably. In order to determine R , we fit an ellipse to the boundary of each structure and compute R as the mean of the minor- and the major-axis of the ellipse. To give an impression of the typical size of the structures, we show the PDFs of the size of OECSs near the TNTI, normalized with the Kolmogorov length scale η for all the flow cases in figure 3.9(a). As can be seen, all three PDFs have a similar behavior, increasing rapidly from the minimum value of $R/\eta \approx 5$ to the position of the peak at about $R/\eta \approx 10$. The PDFs then decrease more slightly up to the highest values at about $R/\eta \approx 50$. Thus, the size of the OECSs covers a rather broad range of ‘active scales’ over one order of magnitude, which may suggest an important role played by these structures in the multiscale aspects discussed in relation to figure 3.8.

In order to understand the role of the OECSs on the evolution of the area of the TNTI, we examine whether the relative motion of the coherent structures with respect to the TNTI has an impact on the stretching, and the curvature/propagation term respectively. To this end, for each selected structure, we isolate a region of the TNTI in the neighborhood of the structure that lies within a distance from the center of the structure of about $5R$. This value was chosen in order to select most of the points of the bulge formed by the TNTI in the proximity of the OECS. We then compute the relative velocity $\mathbf{u}_f - \mathbf{u}_c$ between each of these points of the TNTI and the center of the OECS. Here \mathbf{u}_f denotes the fluid velocity at the location of the TNTI and \mathbf{u}_c the one at the location of the center of the OECS. We then project this velocity difference along the connection segment between each point of the TNTI and the center of the OECS to obtain $(\mathbf{u}_f - \mathbf{u}_c)_{//}$. In figure 3.9, we show the joint PDF of $(\mathbf{u}_f - \mathbf{u}_c)_{//}$ against the strength of $(\delta_{ij} - n_i n_j) S_{ij}$ (figure 3.9b) respectively $v_n \nabla \cdot \mathbf{n}$ (figure 3.9c). As can be gleaned from figure 3.9(b), $(\mathbf{u}_f - \mathbf{u}_c)_{//}$ and

$(\delta_{ij} - n_i n_j)S_{ij}$ are anti-correlated. That is, when $(\mathbf{u}_f - \mathbf{u}_c)_{//}$ is negative, and thus the OECS approaches the TNTI, the stretching term is positive, whereas when $(\mathbf{u}_f - \mathbf{u}_c)_{//}$ is positive the $(\delta_{ij} - n_i n_j)S_{ij}$ contributes to the TNTI compression. This is not entirely unexpected given that the motion of the OECS towards (away from) the interface implies a compression (stretching) normal to the interface and hence, by incompressibility of water, stretching (expansion) in the tangential plane. A similar behavior is encountered for the curvature/propagation term and $(\mathbf{u}_f - \mathbf{u}_c)_{//}$ (figure 3.9c), although less pronounced than in the previous case. Also here, when the OECS approaches the TNTI the curvature/propagation term produces area, whereas when the OECS moves away from the interface, the TNTI area is decreased. Both the joint PDFs shown in figure 3.9 indicate that the motion of the OECS near the TNTI have an influence on the time evolution of the area of the TNTI.

Self similarity of the flow fields around OECSs near the TNTI

In the following, we demonstrate that the flow fields around the OECSs near the TNTI are self similar with respect to the size of the structures by means of a conditional analysis. In particular, we re-sample the velocity, the enstrophy and the IVD fields onto a uniform grid, frame referenced at the center of the OECSs, and normalized in x and z directions with the average size of the structures R . The rationale here is to have a common frame of reference for all the OECSs and to compare flow fields around OECSs of the same normalized size. By taking the average of the IVD fields around the OECSs, we extract a mean representative OECS, that is, we apply the extraction algorithm to the conditional average of the IVD field. To compute the conditional average of the TNTI position, we apply the same change of the coordinate system to the TNTI position near each selected OECS. By defining a curvilinear coordinate s/R along the TNTI which has its origin at the same x coordinate of the highest point on the boundary of the OECS, we compute $\tilde{x}_i(s)$ and $\tilde{z}_i(s)$, the normalized coordinates of the TNTI position near the i -th OECS. In this way, the mean position of the TNTI is computed by taking the average of $\tilde{x}_i(s)$ and $\tilde{z}_i(s)$ over i conditioning with respect to s/R . The same procedure is used also for the terms in (3.4), as well as for the entrainment velocity v_n .

The normalization used here for the spatial coordinates presupposes self similarity of the velocity and the enstrophy fields in the proximity of the OECSs, as well as of the TNTI position and of the terms in (3.4) with respect to the size of the structures R . In order to demonstrate this self similarity, we subdivide the selected structures near the TNTI (of the $Ri11$ flow case) in four different groups with similar cardinality based on their size (with the limits indicated in the caption of figure 3.10) and we conduct a conditional analysis using the spatial normalization indicated above.

In figure 3.10, we present the results of the conditional analysis. Here, the mean position of the TNTI is color-coded with the conditional average of the time evolution of the surface area of the TNTI. Moreover, in the background the conditional average of the enstrophy field is shown, while the arrows indicate the average velocity field relative to the velocity at the center of the OECS. Focusing on figure 3.10(a), the first observation that emerges is that the conditional average position of the TNTI is shaped by the nearby OECSs. Also,

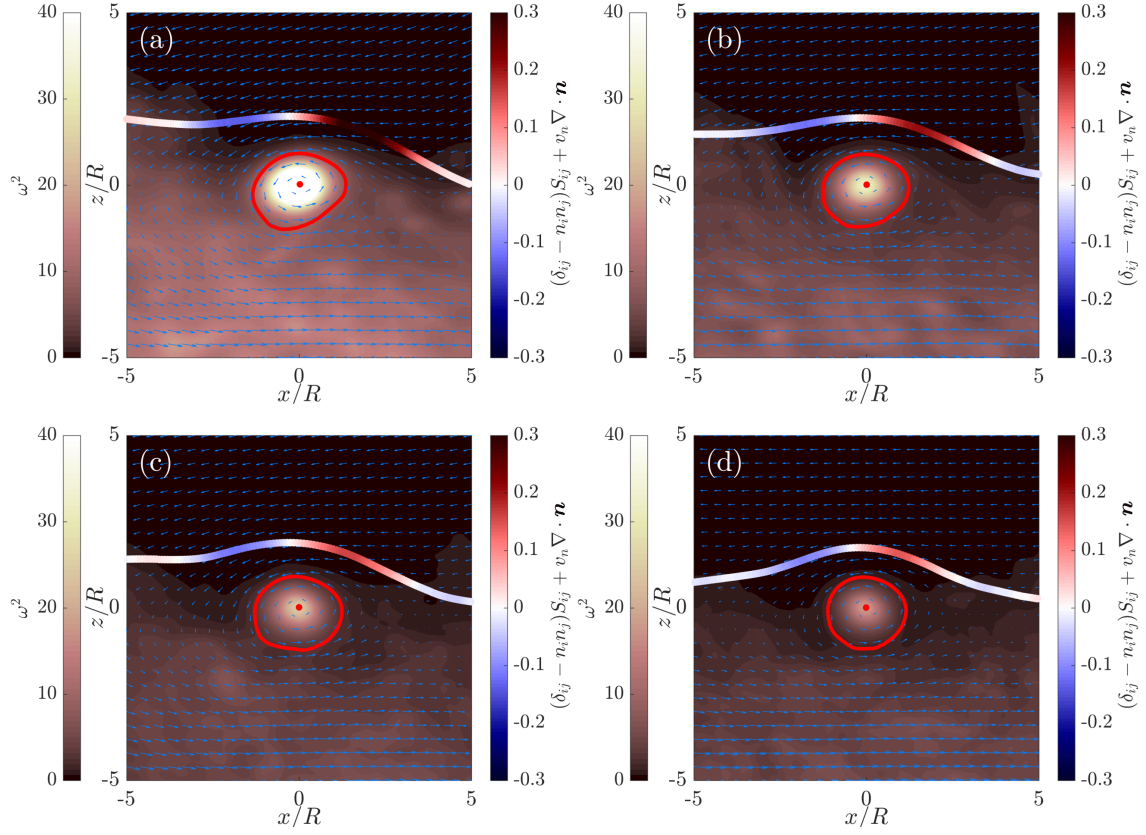


Figure 3.10: Mean OECS and conditional average position of the TNTI for Ri_{11} . The boundary of the mean OECS is constituted by the red closed-curve. The open curve is the conditional average position of the TNTI, color-coded with the time evolution of a non-material infinitesimal element of area δl . The direction and the size of the vectors represent the conditional average velocity field relative to the velocity at the center of the OECSs, whereas in the background the conditional average of the enstrophy field is shown. The conditional analysis is limited to structures near the TNTI with respectively $R/\eta < 10.5$ (a), $10.5 < R/\eta < 12.75$ (b), $12.75 < R/\eta < 15$ (c) and $R/\eta > 15$ (d).

the mean flow around the OECS in the frame of reference co-moving with the center of the structures indicates a rotational fluid motion. The average enstrophy field is particularly high at the center of the mean OECS, decreasing radially towards the boundaries of the OECS. Furthermore, the conditional average of the infinitesimal area variation (shown in colors at the mean position of the TNTI) displays a clear pattern: positive at the leading edge and negative at the trailing edge. As can be seen in figure 3.10(b-d), all the groups show identical patterns and there is a striking similarity in all the aspects discussed for figure 3.10(a). However, as the size of the structures increases (from figure 3.10a to figure 3.10d), both the intensities of the enstrophy field inside the boundaries of the OECS and of the flow field around the OECS decrease. This means that the smaller the structures

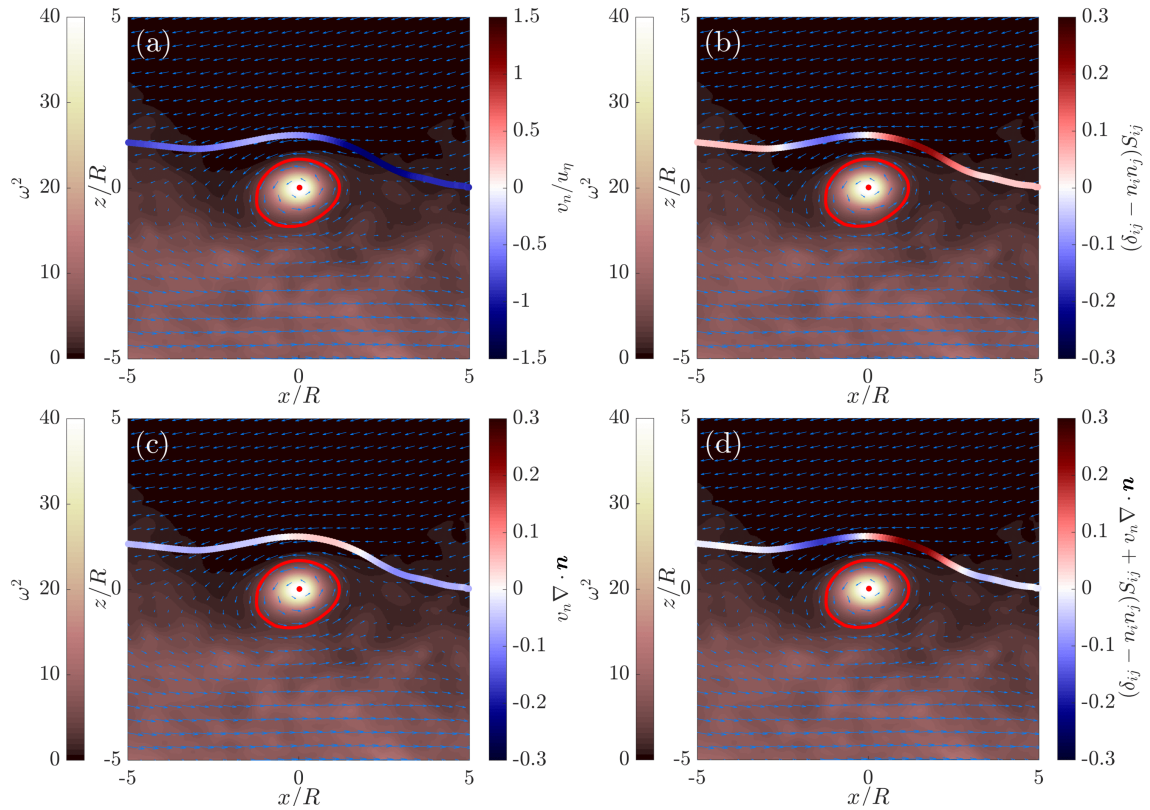


Figure 3.11: Same conditional average shown in figure 3.10 for $Ri11$. In this case, the conditional average position of the TNTI is color-coded with the average entrainment velocity (a), stretching (b) and curvature/propagation terms (c) and the time evolution of a non-material infinitesimal element of area δl .

are, the faster is their rotational motion. Moreover, also the typical pattern shown by the conditional average of the time evolution of the TNTI appears to weaken, when the size of the structures is larger. In conclusion, the results shown in figure 3.10 demonstrate clearly that the vortical structures near the TNTI exhibit a scale-invariant behavior.

Conditional analysis of the time evolution of the TNTI

The effect of the OECSs on the terms of (3.4) is investigated in the following through the conditional analysis presented in section §3.3.3. In figure 3.11, we present the results of the conditional analysis for $Ri11$ in which all the selected structures near the TNTI are considered. In particular, in figure 3.11(a), the mean TNTI is color-coded with the conditional average of the entrainment velocity conditioned with respect to the position on the TNTI. As can be seen, v_n varies along the TNTI and in particular, it is negative at the leading edge, where it reaches values as high as $v_n/u_\eta = -1$, whereas it decreases (in magnitude) at the trailing edge. This result is consistent with the findings from the

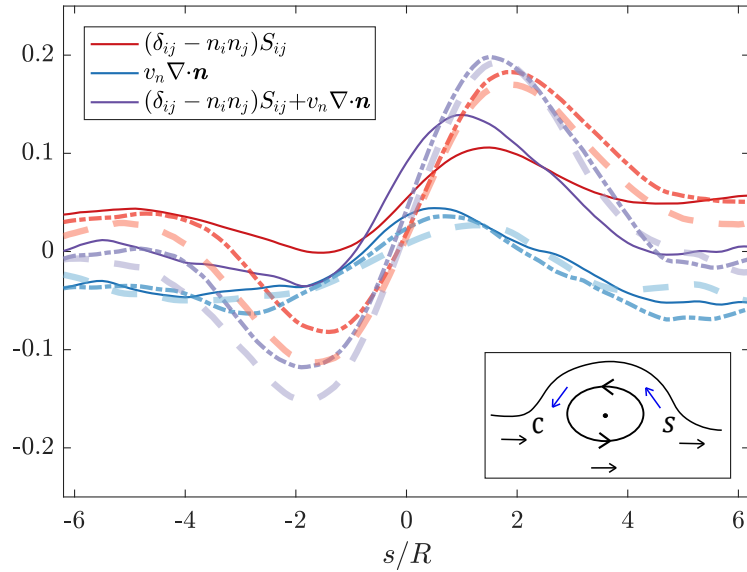


Figure 3.12: Conditional average of the stretching (blue) and the curvature/propagation term (red) and of their sum (purple) in the proximity of the OECS against the curvilinear abscissa s/R for $Ri0$ (continuous line), $Ri11$ (dash-dotted line) and $Ri22$ (dashed line). In the inset, a schematic of the conditional average flow direction around the OECS in the proximity of the interface is shown. The arrows indicate the flow direction between the boundary of the OECS and the TNTI (blue) and in the turbulent region below the OECS (black). ‘C’ denotes the compression, whereas ‘S’ denotes the stretching.

experimental work by Neamtu-Halic *et al.* (2019), where a very similar pattern for v_n was observed. In figure 3.11(b), we display the conditional average of the stretching term of equation (3.4). Here, the mean stretching term has a clear pattern along the TNTI. Indeed, it has positive values at the leading edge respectively negative values at the trailing edge. On the tails, far from the center of the structure, it shows smaller and positive values recovering the unconditioned average value. The surface of the TNTI shown in figure 3.11(c) is color-coded the conditional average of the curvature/propagation term of equation (3.4). The mean curvature/propagation term exhibits a similar behavior as the stretching term, being slightly positive at the leading edge and negative at the trailing edge. The sum of the two terms is plotted in figure 3.11(d). The average infinitesimal area growth rate shown here is positive at the leading edge and negative at the trailing edge. That is, the interface area is produced at the leading edge and destroyed at the trailing edge, whereas far from the structure is negligible reaching the unconditioned average value.

In the following, a comparison of the conditional averages of terms in (3.4) among the different flow cases is presented. For an easier quantitative analysis, in figure 3.12 the conditional averages are shown against the curvilinear abscissa s/R . As can be noticed, all three terms of equation (3.4) have similar trends independently of the flow cases. In particular, moving from $s/R = -6$ in the direction of increasing s/R , the stretching term

decreases, reaching a minimum at about $s/R \approx -2$. Continuing in the in the direction of increasing s/R , $(\delta_{ij} - n_i n_j)S_{ij}$ starts to increase and after an inflection point at $s/R = 0$, it reaches a maximum at $s/R \approx +2$ and then it decreases again. The behavior just described is more intense for the stratified cases, where the minimum of $(\delta_{ij} - n_i n_j)S_{ij}$ at $s/R \approx -2$ is negative. For $Ri0$, the $(\delta_{ij} - n_i n_j)S_{ij}$ has the same behavior but it never reaches negative values. Interestingly, the inflection point of $(\delta_{ij} - n_i n_j)S_{ij}$ happens exactly at $s/R = 0$. A possible mechanism that generates the tangential stretching/compression at the leading/trailing edge of the TNTI surface near the vortical structures is schematically depicted in the inset of figure 3.12. Here the arrows indicate the conditional average flow direction of the fluid motion between boundary of the OECS and the TNTI (blue) and in the turbulent region below the OECS (black). As can be seen, at the leading edge the flow tends to stretch fluid elements, when projected on the tangent to the TNTI surface. Conversely, at the trailing edge, fluid elements are compressed along the direction tangent to the TNTI. In the mechanism just described, the faster the fluid layers beneath the structures, the higher the difference between the relative maximum and minimum of the stretching term. As Ri increases, faster and more horizontal layers of fluid are known to form in the turbulent region. These layers might be responsible for the observed difference among the flow cases. We also note that in the conditional average stretching shown in figure 3.12, the positive contribution of the larger scales is superimposed to the mechanism just described. This is why, for $Ri0$ the relative minimum of the stretching term never reaches negative values. Finally, it is worth noting that the formation of the positive-negative double-peak seen for $Ri22$ is compatible with the more symmetric stretching observed in figure 3.6.

Starting from $s/R = -6$ where it is negative and moving into direction of positive s/R , the conditional average of the curvature/propagation term increases, reaching a positive maximum at $s/R \approx 1$, and decreases, turning again negative at about $s/R = 2$. To explain this behavior, we notice that on both sides of a bulge the curvature is positive (valleys), whereas the entrainment velocity is negative (ambient fluid is entrained). Thus their product is negative and it contributes to the destruction of the area of the TNTI. This is why, negative values of the curvature/propagation term are observed at both sides of the OECSs. Moving from downstream to the leading edge, the curvature of the interface changes the sign (at about $s/R \approx 2$) becoming negative (concave shape as seen from the turbulent side). The entrainment velocity is still negative here, and thus the curvature/propagation term becomes positive. A weak effect of the stratification can be noticed also here where a higher positive value for the maximum of $v_n \nabla \cdot \mathbf{n}$ can be observed for the unstratified case.

The sum of the two terms, the time variation of the infinitesimal area, shows a profile that is similar to the stretching term. Indeed in the proximity of the structure, $(\delta_{ij} - n_i n_j)S_{ij}$ dominates the time evolution of the interface area, dominating over $v_n \nabla \cdot \mathbf{n}$. Thus, the time variation of the infinitesimal area is positive at the leading edge, it has an inflection point at about $s/R \approx 0$ and it becomes negative at the trailing edge. That is, the area of the TNTI is produced at the leading edges and destroyed at the trailing edges. This behavior is clearly consistent with the trends observed qualitatively in figure 3.2.

3.4 Concluding remarks

In this paper, we investigated the production/destruction process of the TNTI area of gravity current flows. We showed that a curvature/propagation term, which is particularly active in the valleys of the TNTI (figure 3.2), contributes on average to the destruction of the TNTI area (figure 3.5), while this is counterbalanced by a flow stretching which on average produces interface area (figure 3.5). In particular, the stretching drives the time evolution of the TNTI area for weak to moderate events, whereas the curvature/propagation term dominates the extreme events (figure 3.6). Very similar results have been found by Wang *et al.* (2017) in the case of a premixed jet flame. In their work, the authors report that the tangential strain produces interface in regions with low curvature, whereas the curvature/propagation term destroys flame surface area in high curvature regions.

The multiscale aspects of the production/destruction of the TNTI area were investigated by filtering the scales smaller than a filter length Δ (figure 3.8). We showed that the stretching and the curvature/propagation terms balance each other at all scales and that the magnitude of the two terms decreases with increasing Δ . Recently, Mistry *et al.* (2016) showed that the mass-flux rate of entrained fluid across the TNTI is constant across all the scales Δ , as envisaged by Meneveau & Sreenivasan (1990). That is, the reduction of A_η with increasing Δ is balanced by the enhancement of v_n at the larger scales. In our case, $v_n \nabla \cdot \mathbf{n}$ reduces with increasing filter length, which means that the increment of v_n is smaller than the rapid decrease of curvature with increasing Δ .

We showed that increasing stratification reduces the averages of both the stretching and the curvature/propagation terms (figure 3.5), while maintaining the same trends for their time variation (figure 3.5) and their filtered values (figure 3.8). In particular, we showed that the reduction of the stretching term is largely attributable to changes in $\delta_{ij} - n_i n_j$ tensor (figure 3.7) and we associated this with the tendency of the interface to flatten with increasing stratification. Indeed, as shown by Krug *et al.* (2017b), for the same flows investigated here, the convolutions of the TNTI scale with the shear length scale $l_{sk} = e^{1/2}/\bar{S}$ in the vertical direction respectively with h in the streamwise direction. While the range of the length scales of the TNTI convolutions impacted by the stable stratification remains the same, it is the growing anisotropy implied by different scalings that modify the geometry of the interface with increasing Ri . Moreover, this change of the TNTI geometry is also compatible the observation that the positive tail of the interface curvature reduces with increasing Ri , which together with the entrainment velocity reduction explains the reduction of the curvature/propagation term.

The local effect of the coherent structures on the TNTI area production/destruction process was investigated through a conditional analysis similar to Neamtu-Halic *et al.* (2019). The conditional analysis showed that both stretching and the curvature/propagation terms produce TNTI area at the leading edge and to destroy it at the trailing edge of the TNTI in proximity of vortical structures. In particular, we inferred that the behavior of the stretching term is related to the mean rotational motion induced by the vortical structures (figure 3.12). A similar mechanism for the tangential stretch of a premixed flame was described in Sinibaldi *et al.* (2003), where the authors observed that

toroidal vortices near the flame boundaries induce a rotational motion that stretches the boundaries on one side of the vortices and compresses it on the other.

Using the conditional analysis, we demonstrated the existence of a scale invariant behavior of the vortices near the TNTI (figure 3.10). A self-similarity of the shapes of the TNTI has been observed a long time ago (Sreenivasan *et al.*, 1989), however a similar observation for the coherent structures near the TNTI is missing up to date in the literature. Moreover, we showed that also the conditional average of the time evolution of the TNTI is self-similar with respect to the size of the OECS. In particular, the time evolution of the TNTI area exhibits lower values for increasing size of the OECS. In figure 3.12, we displayed that near the vortical structures, the time evolution of the interface is mostly dominated by the stretching term. This together with the observation that the rotational motion of the OECS is slower for increasing size of the OECSs (figure 3.10) lends support to the interpretation that the stretching mechanism of the interface is related to the rotation of the OECSs.

In conclusion, to our knowledge, the detailed analysis presented here constitutes a first tentative to describe the evolution of the surface area of the TNTI in the case of turbulent stably stratified shear flows. This work may motivate further studies into the production/destruction mechanisms of the TNTI of other types of turbulent shear flows, such as turbulent jets and wakes and turbulent boundary layers. In particular, it may be of interest to understand whether the vortical structures near the TNTI of these flows have a similar impact on the time evolution of the TNTI and universally apply to all shear flows with an interface. A further issue that may deserve further study is how stratification acts to suppress stretching at large inertial scales.

Acknowledgements

We are grateful for financial support from DFG priority program SPP 1881 under grant number HA 7497/1-1.

J.-P.M. and M.v.R. were supported by the EPSRC project Multi-scale Dynamics at the Turbulent/Non-turbulent Interface of Jets and Plumes (grant number EP/R043175/1) and the UK Turbulence consortium (grant number EP/R029326/1).

Bibliography

- BISSET, D. K., HUNT, J. C. R. & ROGERS, M. M. 2002 The turbulent/non-turbulent interface bounding a far wake. *J. Fluid Mech.* **451**, 383–410. pages 42, 46
- CANDEL, S. M. & POINSOT, T. J. 1990 Flame stretch and the balance equation for the flame area. *Combust. Sci. Technol.* **70** (1-3), 1–15. pages 47
- CORRSIN, S. & KISTLER, A. L. 1955 Free-stream boundaries of turbulent flows . pages 42
- CRASKE, J. & VAN REEUWIJK, M. 2015 Energy dispersion in turbulent jets. part 1. direct simulation of steady and unsteady jets. *J. Fluid Mech.* **763**, 500–537. pages 44
- DAVIDSON, P. A. 2015 *Turbulence: an introduction for scientists and engineers*. Oxford University Press. pages 42
- DIMOTAKIS, P. E. 2000 The mixing transition in turbulent flows. *J. Fluid Mech.* **409**, 69–98. pages 42
- DOPAZO, C., MARTÍN, J. & HIERRO, J. 2006 Iso-scalar surfaces, mixing and reaction in turbulent flows. *C. R. Mech.* **334** (8-9), 483–492. pages 47
- ELLISON, T. H. & TURNER, J. S. 1959 Turbulent entrainment in stratified flows. *J. Fluid Mech.* **6** (3), 423–448. pages 43
- HALLER, G. 2015 Lagrangian coherent structures. *Annu. Rev. Fluid Mech.* **47**, 137–162. pages 47
- HALLER, G. 2016 Dynamic rotation and stretch tensors from a dynamic polar decomposition. *J. Mech. Phys. Solids* **86**, 70–93. pages 47
- HALLER, G., HADJIGHASEM, A., FARAZMAND, M. & HUHN, F. 2016 Defining coherent vortices objectively from the vorticity. *J. Fluid Mech.* **795**, 136–173. pages 43, 47

- HOLZNER, M., LIBERZON, A., GUALA, M., TSINOBER, A. & KINZELBACH, W. 2006 Generalized detection of a turbulent front generated by an oscillating grid. *Exp. Fluids* **41** (5), 711–719. pages 42
- HOLZNER, M., LIBERZON, A., NIKITIN, N., KINZELBACH, W. & TSINOBER, A. 2007 Small-scale aspects of flows in proximity of the turbulent/nonturbulent interface. *Phys. Fluids* **19** (7), 071702. pages 46
- HOLZNER, M., LIBERZON, A., NIKITIN, N., LÜTHI, B., KINZELBACH, W. & TSINOBER, A. 2008 A lagrangian investigation of the small-scale features of turbulent entrainment through particle tracking and direct numerical simulation. *J. Fluid Mech.* **598**, 465–475. pages 46
- HOLZNER, M. & LÜTHI, B. 2011 Laminar superlayer at the turbulence boundary. *Phys. Rev. Lett.* **106** (13), 134503. pages 42, 46
- KRUG, D., CHUNG, D., PHILIP, J. & MARUSIC, I. 2017a Global and local aspects of entrainment in temporal plumes. *J. Fluid Mech.* **812**, 222–250. pages 42
- KRUG, D., HOLZNER, M., LÜTHI, B., WOLF, M., KINZELBACH, W. & TSINOBER, A. 2015 The turbulent/non-turbulent interface in an inclined dense gravity current. *J. Fluid Mech.* **765**, 303–324. pages 43, 46, 56
- KRUG, D., HOLZNER, M., MARUSIC, I. & VAN REEUWIJK, M. 2017b Fractal scaling of the turbulence interface in gravity currents. *J. Fluid Mech.* **820**. pages 42, 43, 45, 46, 54, 55, 56, 57, 64
- LEE, J., SUNG, H. J. & ZAKI, T. A. 2017 Signature of large-scale motions on turbulent/non-turbulent interface in boundary layers. *J. Fluid Mech.* **819**, 165–187. pages 43
- LEGG, S., BRIEGLEB, B., CHANG, Y., CHASSIGNET, E. P., DANABASOGLU, G., EZER, T., GORDON, A. L., GRIFFIES, S., HALLBERG, R., JACKSON, L. & OTHERS 2009 Improving oceanic overflow representation in climate models: the gravity current entrainment climate process team. *B. Am. Meteorol. Soc.* **90** (5), 657–670. pages 43
- MACDONALD, D. G., CARLSON, J. & GOODMAN, L. 2013 On the heterogeneity of stratified-shear turbulence: Observations from a near-field river plume. *J. Geophys. Res.* **118** (11), 6223–6237. pages 43
- MATER, B. D. & VENAYAGAMOORTHY, S. K. 2014 A unifying framework for parameterizing stably stratified shear-flow turbulence. *Phys. Fluids* **26** (3), 036601. pages 46
- MATHEW, J. & BASU, A. J. 2002 Some characteristics of entrainment at a cylindrical turbulence boundary. *Phys. Fluids* **14** (7), 2065–2072. pages 42

- MELLADO, J. P. 2010 The evaporatively driven cloud-top mixing layer. *J. Fluid Mech.* **660**, 5–36. pages 43
- MENEVEAU, C. & SREENIVASAN, K. R. 1990 Interface dimension in intermittent turbulence. *Phys. Rev. A* **41** (4), 2246. pages 64
- MISTRY, D., PHILIP, J. & DAWSON, J. R. 2019 Kinematics of local entrainment and detrainment in a turbulent jet. *J. Fluid Mech.* **871**, 896–924. pages 42, 43
- MISTRY, D., PHILIP, J., DAWSON, J. R. & MARUSIC, I. 2016 Entrainment at multi-scales across the turbulent/non-turbulent interface in an axisymmetric jet. *J. Fluid Mech.* **802**, 690–725. pages 64
- MORTON, B. R., TAYLOR, G. I. & TURNER, J. S. 1956 Turbulent gravitational convection from maintained and instantaneous sources. *Proc. R. Soc. Lond. A* **234** (1196), 1–23. pages 42
- MURTHY, S. 2013 *Turbulent mixing in nonreactive and reactive flows*. Springer Science & Business Media. pages 42
- NEAMTU-HALIC, M. M., KRUG, D., HALLER, G. & HOLZNER, M. 2019 Lagrangian coherent structures and entrainment near the turbulent/non-turbulent interface of a gravity current. *J. Fluid Mech.* **877**, 824–843. pages 43, 46, 48, 49, 57, 62, 64
- PHILLIPS, O. M. 1972 The entrainment interface. *J. Fluid Mech.* **51** (1), 97–118. pages 42, 47
- VAN REEUWIJK, M., HOLZNER, M. & CAULFIELD, C. P. 2019 Mixing and entrainment are suppressed in inclined gravity currents. *J. Fluid Mech.* **873**, 786–815. pages 44, 56
- VAN REEUWIJK, M., KRUG, D. & HOLZNER, M. 2018 Small-scale entrainment in inclined gravity currents. *Environ. Fluid Mech.* **18** (1), 225–239. pages 43, 44, 45
- SERRA, MATTIA & HALLER, GEORGE 2016 Objective eulerian coherent structures. *Chaos* **26** (5), 053110. pages 43
- DA SILVA, C. B., HUNT, J. C. R., EAMES, I. & WESTERWEEL, J. 2014 Interfacial layers between regions of different turbulence intensity. *Annu. Rev. Fluid Mech.* **46**, 567–590. pages 42
- DA SILVA, C. B. & DOS REIS, R. J. N. 2011 The role of coherent vortices near the turbulent/non-turbulent interface in a planar jet. *Phil. Trans. R. Soc. A* **369** (1937), 738–753. pages 43
- DE SILVA, C. M., PHILIP, J., CHAUHAN, K.L, MENEVEAU, C. & MARUSIC, I. 2013 Multiscale geometry and scaling of the turbulent-nonturbulent interface in high reynolds number boundary layers. *Phys. Rev. Lett.* **111** (4), 044501. pages 42

- SILVA, T. S., ZECCHETTO, M. & DA SILVA, C. B. 2018 The scaling of the turbulent/non-turbulent interface at high reynolds numbers. *J. Fluid Mech.* **843**, 156–179. pages 42, 46
- SIMPSON, J. E. 1999 *Gravity currents: In the environment and the laboratory*. Cambridge university press. pages 42
- SINIBALDI, J. O., DRISCOLL, J. F., MUELLER, C. J., DONBAR, J. M. & CARTER, C. D. 2003 Propagation speeds and stretch rates measured along wrinkled flames to assess the theory of flame stretch. *Combust. Flame* **133** (3), 323–334. pages 64
- SREENIVASAN, K. R., RAMSHANKAR, R. & MENEVEAU, C. H. 1989 Mixing, entrainment and fractal dimensions of surfaces in turbulent flows. *Proc. R. Soc. Lond. A* **421** (1860), 79–108. pages 42, 54, 65
- TOWNSEND, A.A. 1966 The mechanism of entrainment in free turbulent flows. *J. Fluid Mech.* **26** (4), 689–715. pages 42
- TRITTON, D. J. 1988 *Physical fluid dynamics, Clarendon*. pages 42
- TSINOBER, A. 2009 An informal conceptual introduction to turbulence, , vol. 483. Springer. pages 42
- WANG, H., HAWKES, E. R., CHEN, J. H., ZHOU, B., LI, Z. & ALDÉN, M. 2017 Direct numerical simulations of a high karlovitz number laboratory premixed jet flame—an analysis of flame stretch and flame thickening. *J. Fluid Mech.* **815**, 511–536. pages 64
- WATANABE, T., JAULINO, R., TAVEIRA, R.R., DA SILVA, C.B., NAGATA, K. & SAKAI, Y. 2017 Role of an isolated eddy near the turbulent/non-turbulent interface layer. *Phy. Rev. Fluid* **2** (9), 094607. pages 43
- WATANABE, T., SAKAI, Y., NAGATA, K., ITO, Y. & HAYASE, T. 2014 Enstrophy and passive scalar transport near the turbulent/non-turbulent interface in a turbulent planar jet flow. *Phys. Fluids* **26** (10), 105103. pages 42
- WESTERWEEL, J., FUKUSHIMA, C., PEDERSEN, J. M. & HUNT, J. C. R. 2005 Mechanics of the turbulent-nonturbulent interface of a jet. *Phys. Rev. Lett.* **95** (17), 174501. pages 42
- WOLF, M., LÜTHI, B., HOLZNER, M., KRUG, D., KINZELBACH, W. & TSINOBER, A. 2012 Investigations on the local entrainment velocity in a turbulent jet. *Phys. Fluids* **24** (10), 105110. pages 42, 46

Chapter 4

Role of vortical structures for enstrophy and scalar transport in a turbulent flow with and without stable stratification

This chapter consists of a manuscript submitted to Journal of Turbulence, 2020:

M. Neamtu, J.-P. Mollicone, M. van Reeuwijk, G. Haller, and M. Holzner (2020). Role of vortical structures on the terms of enstrophy and scalar transport equation.

Abstract: In this paper, we investigate the enstrophy dynamics in relation to objective Eulerian coherent structures (OECSs) and their impact on the enstrophy and scalar transport near the turbulent/non-turbulent interface (TNTI) in flows with and without stable stratification. We confirm that vortex-stretching produces enstrophy inside the boundaries of the OECSs, while viscous diffusion transfers the enstrophy across the boundaries of the structures. Although often overlooked in the literature, viscous dissipation of enstrophy within the boundaries of vortical structures is significant. Conversely, for the weakly stratified flows also investigated here, the effect of the baroclinic torque is negligible. We provide evidence that the OECSs advect the passive/active scalar and redistribute it via molecular diffusion. Finally, we use conditional analysis to show that the typical profiles of the enstrophy and scalar transport equation terms across the TNTI are compatible with the presence of OECSs positioned at the edge between the turbulent sublayer and the turbulent core region. We show that when these profiles are further conditioned to

the presence of OECSs, their magnitude is considerably higher.

4.1 Introduction

Vortical coherent structures have received considerable attention from the turbulence community over the last decades. Mostly defined as regions with concentrated vorticity and material coherence with a life time larger than the typical time scales of the flow Dubief & Delcayre (2000); Haller (2015), vortical structures constitute an appealing tool for understating complex turbulent flow phenomena (Lesieur, 1987). Moreover, vortical structures are valuable to investigate the mixing and the transport of mass, momentum and scalar (e.g. temperature or concentration) in turbulent flows (Haller, 2015).

In turbulent flows, a well-established convention divides vortical structures into two classes: the so-called large scale vortices (LSVs) and the intense vorticity structures (IVSs) (da Silva *et al.*, 2011). The LSVs originate from the particular instability of a certain type of flow and their characteristics such as size and lifetime are reported to be flow dependent (Frisch & Kolmogorov, 1995; Tsinober, 2009). On the other hand, IVSs have similar characteristics across a variety of flows. Mostly detected through a threshold on the vorticity (Jiménez *et al.*, 1993), IVSs are known in isotropic turbulence as “worms” (Siggia, 1981). Many studies dedicated to these worms showed that universally their size is of order of 5η , with η the Kolmogorov length scale, in isotropic turbulence (Siggia, 1981; Jiménez *et al.*, 1993; Jimenez & Wray, 1998; Vincent & Meneguzzi, 1991), in mixing layers (Tanahashi *et al.*, 2001), in channel flows (Kang *et al.*, 2007) and in jets (Ganapathisubramani *et al.*, 2008). In an early study by Jiménez *et al.* (1993), IVSs were observed to be rather stable structures and their dynamical behaviour was shown to be similar to that of a stable Burger vortex model, which is characterized by a radial balance inside a vortex tube between enstrophy production and enstrophy diffusion. However, a direct assessment of the enstrophy production and enstrophy diffusion mechanisms is still missing in the literature. Moreover, it is not clear how other mechanisms such as viscous dissipation of enstrophy or the baroclinic torque that is present in stratified flows may contribute to these. To date, research progress on the enstrophy transport by vortical structures has been hampered by arbitrariness in the detection methods, which are mostly based on thresholding either the vorticity field (Hussain, 1986; Jiménez *et al.*, 1993; da Silva *et al.*, 2011) or the vorticity relative to the strain field (Okubo, 1970; Hunt *et al.*, 1988; Weiss, 1991; Hua & Klein, 1998). Progress made in a recent string of research (Haller, 2015) allows to overcome the arbitrariness of the classic methods and permits to identify objective (i.e. observer-independent) coherent structures, as required for replicable experiments.

In the present work, we extract objective coherent structures and investigate the enstrophy dynamics inside vortical structures to shed a light on the mechanisms that govern the time evolution of the enstrophy contained in these structures. We use a newly developed extraction method to systematically identify objective Eulerian coherent structures (OECSs) (Haller *et al.*, 2016; Serra & Haller, 2016) and we apply it to direct numerical simulations (DNSs) data of a turbulent flow with and without stable stratification.

The impact of vortical structures on the transport of scalars, such as concentration

or temperature, have been matter of numerous studies in recent years (Kadoch *et al.*, 2011; Beta *et al.*, 2003). The main motivation has been to better understand the role of vortical structures in organizing scalar transport which is relevant in many practical applications, e.g. mixing of pollutants in atmosphere or heat-transfer in heat exchangers and gas turbines. In particular, Kadoch *et al.* (2011) showed that in homogeneous, isotropic turbulence vortical structures are mainly responsible for turbulent transport and mixing of passive scalars. The impact of vortical structures on heat transport was investigated by Dharmarathne *et al.* (2018) in a thermal turbulent channel flow. They observed that vortical structures near the wall contribute to the removal of hot fluid from the wall to outer region. Debusschere & Rutland (2004) studied heat transport in plane channel and Couette flows. Their results indicated that in channel flow the overall vertical heat transfer is lower as compared to Couette flow. They attributed this observation to the presence of large scale vortical structures in Couette flow that transport heat across the center line of the flow, while similar structures are missing in plane channel flow. Fröhlich *et al.* (2008) investigated the scalar transport in co-annular swirling jets. They found that 30 – 40% of the concentration fluctuation is carried by large-scale coherent flow structures. Here, we use conditional analysis to investigate the impact of OECSs on the transport and diffusion of the active/passive scalar of flows with and without stable stratification.

At the boundaries of turbulence, a sharp and highly contorted interface, so-called turbulent/non-turbulent interface (TNTI), is known to separate the turbulent region from the irrotational surrounding fluid (Corrsin & Kistler, 1955; Westerweel *et al.*, 2009; da Silva *et al.*, 2014). The ambient surrounding fluid is continuously entrained into the turbulent side through the TNTI, a phenomenon known as turbulent entrainment. It has been shown that turbulent entrainment is a two-stage process (Chauhan *et al.*, 2014; Mistry *et al.*, 2016; Watanabe *et al.*, 2016). Initially, at the outer edge of the TNTI, a non-turbulent fluid parcel acquires vorticity via viscous diffusion (Holzner & Lüthi, 2011) and subsequently, in the turbulent region vorticity is amplified through vortex stretching. The role played by the vortical structures along these two stages was recently investigated by Watanabe *et al.* (2017). The authors used a model to show that the average profile of enstrophy production and enstrophy viscous diffusion near the TNTI are compatible with the presence of Burger-type vortex near the interface. By positioning a Burger-vortex of the size of the IVSs at a distance of approximately 9η from the TNTI, they predicted reasonably well the profiles of the enstrophy production and enstrophy viscous diffusion across the TNTI of a free shear turbulent flow. However, in its present form their model lacks other effects such as viscous dissipation of enstrophy and baroclinic torque that may potentially be of significance. In this work, we compute the conditional profiles of the terms in the enstrophy transport equation across the TNTI and compare them to those crossing an OECS near the interface. The goal is to understand the impact of vortical structures as extracted from the flow on the dynamics of enstrophy near the TNTI. To identify the OECSs that are in proximity of the TNTI and to investigate their contribution to enstrophy and scalar transport, we use a recently developed conditional analysis by Neamtu-Halic *et al.* (2019).

The turbulent transport of the scalar across the TNTI is an important phenomenon for

many applications of practical interest (e.g. chemical reactors) (Dimotakis, 2000). In a recent work by Watanabe *et al.* (2015), it was shown that a large jump of passive scalar exists at the boundary of turbulent flow regions and that molecular diffusion exchanges the passive scalar between the turbulent region and the fluid in the TNTI proximity. Since vortical structures are known to carry large amount of scalar (Kadoch *et al.*, 2011), larger gradients of the scalar are expected in proximity of the TNTI when OECSs are present. Our aim is to understand how OECSs impact the transport of the scalar near the TNTI.

In nature, turbulent flows develop frequently in presence of stable stratification (e.g. cloud-top mixing layers, river plumes and oceanic overflows). In these flows, the entrainment rate is known to diminish with increasing Richardson number Ri , the ratio between the buoyancy and shear strength of the flow (Ellison & Turner, 1959). Nowadays, it is widely accepted that entrainment rate reduces with increasing stratification as a consequence of the reduction of both the local entrainment velocity and the area of the TNTI (Krug *et al.*, 2015; van Reeuwijk *et al.*, 2018, 2019). Recently, Neamtu-Halic *et al.* (2019) used experimental data of a gravity current to show that OECSs modulate the area of the TNTI and that their modulating capacity diminish with increasing stratification. Moreover, OECSs have been observed to organize the flow field on the TNTI proximity thereby imposing the local entrainment velocity (Neamtu-Halic *et al.*, 2019) and setting the mechanism that produces/destroys the surface area of the nearby TNTI (Neamtu-Halic *et al.*, 2020). It remains to be understood how OECSs affect the process of the entrainment and how do they adapt at different levels of stratification. To this end, we apply the conditional analysis of the enstrophy transport equation to the direct numerical simulations data of gravity currents and of a wall-jet. Moreover, we investigate how the diffusion of the active/passive scalar across the interface in the OECSs proximity varies with increasing stratification.

The main scope of the paper is to investigate the dynamics of the enstrophy inside the OECSs and to understand the role of the OECSs in the transport of the scalar, with a particular regard to the region in proximity of the TNTI.

The paper is organized as follows. In §4.2 we present the DNS data set. This is followed by the presentation of the results in §4.3, while a summary and concluding remarks are given in §4.4.

4.2 Methods

4.2.1 DNS data set

The data set employed in this work consists of DNSs of temporally evolving gravity currents and of a temporal turbulent wall-jet. These flows are particularly suitable to study the transport of enstrophy and scalar in that different intensities of vertical transport of these quantities can be obtained by varying the stratification level. It is thus possible to investigate how OECSs adapt to this change and contribute to transport. The simulations reproduce the classical experiment of Ellison & Turner (1959), in which a lighter turbulent fluid flows along the top of an inclined wall in a heavier ambient irrotational

	$\alpha(\text{deg.})$	Ri_0	Re_0	Re_λ	$N_x N_y N_z$	$L_x L_y L_z / h_0^3$
$Ri0$	–	0	3700	115	$1536^2 \times 1152$	$20^2 \times 10$
$Ri11$	10	0.11	3700	105	$1536^2 \times 1152$	$20^2 \times 10$
$Ri22$	5	0.22	3700	70	$1536^2 \times 1152$	$20^2 \times 10$

Table 4.1: Simulation parameters: N_i and L_i denote the number of grid points and the size along i -direction respectively. The subscript 0 indicates the inflow parameters. The Taylor Reynolds number $Re_\lambda = \sqrt{15/\nu\epsilon}e^{1/2}$ is computed averaging the rate of turbulent dissipation ϵ and the turbulent kinetic energy e over $120 < t < 130$.

fluid. As sketched in figure 4.1(a), we reverse the problem upside-down as we simulate the motion of a negatively buoyant fluid flowing down a slope inclined at an angle α . The physics of the problem is unaffected as we consider a Boussinesq fluid. The temporal problem is particularly suitable for obtaining converged statistics relatively inexpensively, as it is homogeneous in the wall-normal planes and the statistics depend only on time and wall normal direction. For the simulations, we employ SPARKLE, a code that solves the Navier–Stokes equations in the Boussinesq approximation (Craske & van Reeuwijk, 2015)

$$\frac{\partial \mathbf{u}}{\partial t} + \mathbf{u} \cdot \nabla \mathbf{u} = -\nabla p + \nu \nabla^2 \mathbf{u} + \mathbf{b}, \quad (4.1)$$

$$\frac{\partial c}{\partial t} + \mathbf{u} \cdot \nabla c = D \nabla^2 c, \quad (4.2)$$

$$\nabla \cdot \mathbf{u} = 0. \quad (4.3)$$

with a fourth-order accurate finite volume discretization scheme (Craske & van Reeuwijk, 2015) on a cuboidal domain. Here, $\mathbf{u} = (u, v, w)$ is the fluid velocity in the x streamwise, y spanwise and z wall-normal direction, p is the (modified) kinematic pressure, $\mathbf{b} = \beta \mathbf{g} c$ is the buoyancy, with $\mathbf{g} = (\sin\alpha, 0, \cos\alpha)$ to simulate the sloping bottom and $\beta = \rho_0^{-1} \partial \rho / \partial c|_{c_0}$, and ν, D are the kinematic and molecular diffusivity, respectively. For the wall jet c is a passive scalar (with Schmidt number $Sc = 1$), whilst for the gravity current c is an active scalar.

The boundary conditions are periodic in the streamwise and the spanwise direction, while in the vertical direction, at the wall ($z = 0$) and at the top of the simulation domain, no slip and free slip velocity boundary conditions are imposed respectively for the velocity and Neumann (no-flux) boundary conditions are imposed for scalar c . For the initial conditions (indicated by subscript 0), a uniform distribution of both the streamwise velocity u_0 and the scalar c_0 up to a height h_0 above the bottom wall are implemented. A schematic representation of the simulation set-up is shown in figure 4.1(a). The size of the domain is $L_x \times L_y \times L_z = 20h_0 \times 20h_0 \times 10h_0$ with a resolution of $1536^2 \times 1152$. For

a more detailed discussion on the DNSs concept and numerical configuration we refer to van Reeuwijk *et al.* (2018, 2019).

Following Neamtu-Halic *et al.* (2020), we simulated three different flow cases, namely a wall-jet ($\beta = 0$) and two different gravity currents ($\beta > 0$). The flow cases differ in the initial Richardson number $Ri_0 = B_0 \cos(\alpha)/u_0^2$, where $B_0 = \beta g c_0 h_0$ is a conserved quantity in the simulations, whereas the initial bulk Reynolds number $Re_0 = u_0 h_0/\nu$ is kept constant. Table 4.1 summarizes the parameters of the simulations employed in this study. Note that the label of the flow cases indicates the value of Ri_0 . The results presented here are based on data over six independent xz -planes, which are equally spaced in the y -direction, amounting to 280 snapshots over a period of $140\tilde{t}$, with $\tilde{t}h_0/u_0$.

Throughout the paper, we use the following top-hat definitions

$$u_T h = \int_0^\infty \bar{u} dz, \quad u_T^2 h = \int_0^\infty \bar{u}^2 dz \quad \text{and} \quad c_T h = \int_0^\infty \bar{c} dz, \quad (4.4)$$

where \bar{u} and \bar{c} are the mean streamwise velocity respectively the mean concentration, computed averaging in wall-parallel planes.

To characterize the structure of the flows, in figure 4.1(b) the mean profile of the streamwise velocity are normalized with the top hat definitions, showing a collapse on a single curve for all flow cases in the outer layer of the flow. That is, although there are fundamental differences between the gravity currents and the wall-jet, the structure of the flows is similar. The mean profile of the scalar concentration is shown in figure 4.1(c). Again, when normalized with the top hat definitions, the profiles collapse on a single curve, although c has a different physical interpretation in the stratified cases as compared to the unstratified one. We note that the similarities of the flow structure shown here are due to the fact that although the gravity currents presented here are buoyancy driven, the turbulence characteristics are shear dependent (Krug *et al.*, 2017b).

The time evolution of the top-hat definitions is shown in figure 4.1(d-f). After an initial transition, the current height h grows linearly for the gravity currents and $h \propto \tilde{t}^{1/2}$ for the wall-jet, while u_T is constant for the gravity currents and $u_T \propto \tilde{t}^{-1/2}$ for Ri_0 (van Reeuwijk *et al.*, 2018). As Ri increases, h decreases while u_T increases. On the other hand, $c_T \propto \tilde{t}^{-1}$ for the gravity currents and $c_T \propto \tilde{t}^{-1/2}$ for the wall-jet, with c_T increasing with decreasing stratification.

4.2.2 OECSs eduction and TNTI identification

The identification method used in this work to extract vortical structures is based on the so-called instantaneous vorticity deviation (IVD). The IVD is an observer-independent scalar field that measures an intrinsic material rotation rate of fluid elements (Haller *et al.*, 2016). Derived from a new dynamic version of the classic polar decomposition (Haller, 2016), the IVD field is defined by

$$IVD(\mathbf{x}, t) = |\boldsymbol{\omega}(\mathbf{x}, t) - \bar{\boldsymbol{\omega}}(t)| \quad (4.5)$$

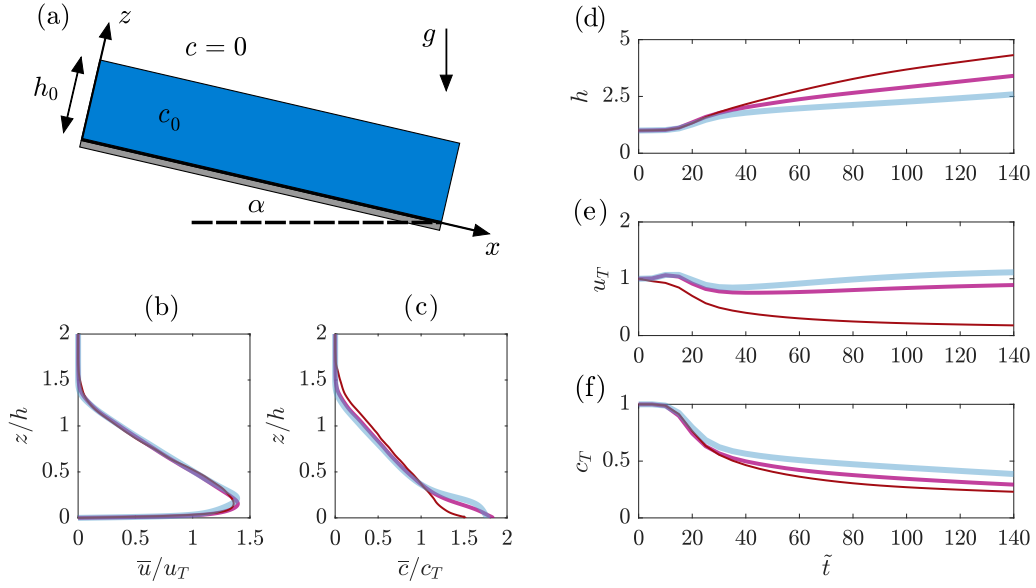


Figure 4.1: Schematic representation of the simulation setup (a). Vertical profiles of the mean streamwise velocity (b) and mean concentration (c) for $Ri0$ (red), $Ri11$ (purple) and $Ri22$ (light blue). Time variation of current height (d), top-hat velocity (e) and top-hat concentration (f).

where $\omega(\mathbf{x}, t)$ is the vorticity vector and $\bar{\omega}(t)$ is its spatial mean. In particular, the *IVD* provides an observer-independent local angular velocity for each point of the fluid mass and therefore, enables the identification of OECSs in an observer-independent manner, as required for reproducible coherent structure extraction (Haller, 2015). Local maxima of the *IVD* field identify the center of the OECSs, while the outermost almost convex contour of the *IVD* encircling a local maximum represents the boundary of the structure. To contain the computational costs, we extract 2D OECSs from vertical planes of 3D data. We use a criterion defined in Neamtu-Halic *et al.* (2020) in which a maximum of the *IVD* field is selected only if the ratio between the two eigenvalues of the Hessian of *IVD* at the location of *IVD* maxima is below a threshold. The rationale behind this criterion is based on the fact that a 2D OECS in a slice results from the intersection of the tubular structures with the plane itself. Since most of the dynamics of tubular vortical structures happens in planes perpendicular to the center-line of the structure, we select only structures that are perpendicular to the plane (Neamtu-Halic *et al.*, 2020). The results presented throughout the paper corresponds to $120 < \tilde{t} < 130$.

To identify the position of the TNTI, we impose a threshold on the enstrophy field $\omega^2 = \omega_i \omega_i$ (Bisset *et al.*, 2002; Holzner *et al.*, 2007, 2008; Silva *et al.*, 2018; Neamtu-Halic *et al.*, 2019). Here, the threshold is selected as $\omega_{thr}^2 = 10^{-3} \bar{\omega}^2$, where $\bar{\omega}^2$ is the space average of the enstrophy. Following a criterion by Taveira *et al.* (2013), the threshold values were verified to lie within the interval of possible values in which there is no appreciable variation of the volume fraction of the turbulent region with ω_{thr}^2 .

4.2.3 Radial profiles and conditional profiles.

We investigate the radial profiles inside the OECSs of the terms of the enstrophy transport equation

$$\frac{D\omega^2}{Dt} = 2\omega_i\omega_j S_{ij} + \nu\nabla \cdot (\nabla\omega^2) - 2\nu\nabla\omega_i : \nabla\omega_i + 2\epsilon_{ijk}\omega_i \frac{\partial g'_k}{\partial x_j} \quad (4.6)$$

where $\mathcal{P}_{\omega^2} = 2\omega_i\omega_j S_{ij}$ is the the enstrophy production, with S_{ij} the rate of strain tensor, $\mathcal{D}_{\omega^2} = \nu\nabla \cdot (\nabla\omega^2)$ is the viscous diffusion of enstrophy, $\mathcal{E}_{\omega^2} = -2\nu\nabla\omega_i : \nabla\omega_i$ is the viscous dissipation term, $\mathcal{B}_{\omega^2} = 2\epsilon_{ijk}\omega_i \frac{\partial g'_k}{\partial x_j}$ is the baroclinic torque, and of the scalar transport equation

$$\frac{Dc}{Dt} = D\nabla \cdot (\nabla c). \quad (4.7)$$

In order to compute these profiles, for each selected structure we connect the center of the structure with the points on the boundaries (figure 4.2a) with a segment and interpolate the scalar terms of (4.6,4.7) above on the points of the segment. The distance from the center of the OECS is then normalized with the distance between the center and the boundary R . Note that the material derivatives are computed from the terms on the right hand side of (4.6,4.7).

In the TNTI proximity, average values of the terms in equations (4.6) and (4.7) are also computed conditioned with respect to the position of the TNTI. As consolidated in the literature (Krug *et al.*, 2015; da Silva *et al.*, 2014), these terms are computed along lines that are normal to the TNTI itself, as schematically shown in figure 4.2(b), with the distance from the interface normalized by the Kolmogorov length scale η . Here the normal to the interface points in the direction of the turbulent region. In a second set of results presented in this work, we use a further condition. That is, we compute the conditional averages of the quantities in equations (4.6) and (4.7) with respect to the TNTI along lines that are approximately perpendicular ($90^\circ \pm 30^\circ$) to the TNTI and passing through the center of OECSs near the TNTI. A sketch of this concept is illustrated in figure 4.2(b). Also in this case the origin is fixed at the TNTI position.

4.3 Results

4.3.1 General description of coherent structures

In the following we provide a general description of the OECSs extracted from the three flow cases. In figure 4.3(a), we show the probability density function (PDF) of the size of the structures D , normalized by the Kolmogorov length scale $\eta = (\nu\epsilon)^{1/4}$. To compute D we fit an ellipse on the boundaries of the OECSs and calculate D as the mean value between the minor and the major axes of the fitting ellipse. Note that the use of a single size to express the dimension of the OECSs is justified by the fact the aspect ratio of the structures is not far from 1, with an average value of approximately 0.8. The PDF of the OECSs size shows a sharp increase from approximately 3η to 7η where it presents

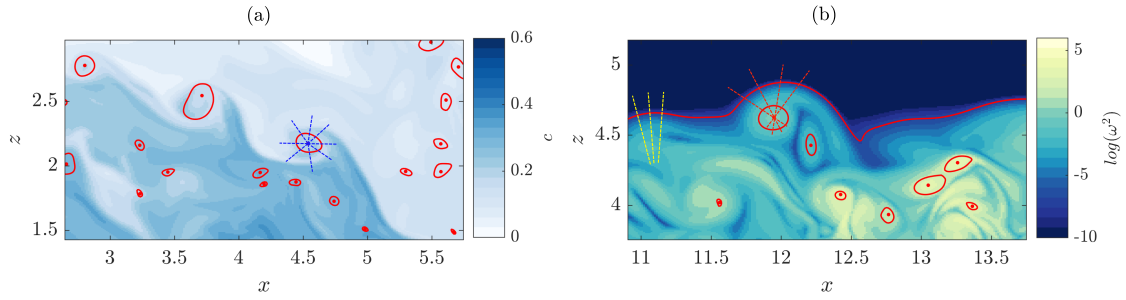


Figure 4.2: (a) OECSs (red) and radial lines (dashed blue lines), with the scalar field in the background. Local normal lines (yellow) to the TNTI (red open curve) and local approximately-normal lines (red dashed lines) passing through the center of an OECSs, with the enstrophy field in the background.

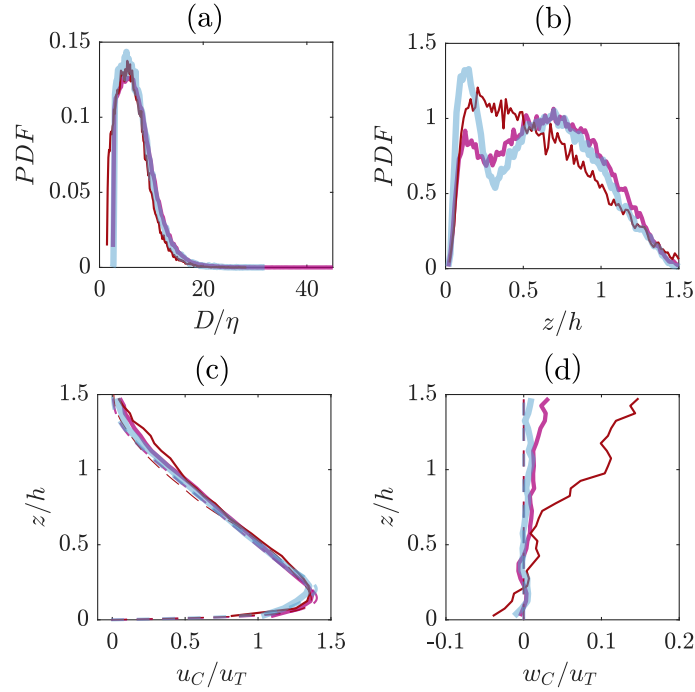


Figure 4.3: PDFs of size of the OECSs (a) and of the position of their center (b). Mean streamwise (c) and wall-normal (d) velocities at the center of the OECSs (continuous) against the mean velocity profiles (dashed) for $Ri0$ (red), $Ri11$ (purple) and $Ri22$ (light blue).

a maximum, to decrease more gradually up to 40η . As the Ri number increases, there is no significant difference in terms of the size distribution of the structures.

The position of the center of the structures normalized by the current height h is shown in figure 4.3(b). For all flow cases, in the wall proximity, the PDFs grow approximately

linearly up to $z/h \approx 0.15$, where the PDF shows a peak. Interestingly, this height corresponds to the position of the maximum of the mean stream-wise velocity profile, which means that this region is a particularly active region for the formation of coherent flow structures. From the maximum towards larger wall distance, a different behaviour can be noticed for the unstratified case compared to the stratified ones. For $Ri0$, the PDF decreases monotonically towards the outer region of the current at $z/h \approx 1.5$. Conversely, for the gravity currents, the PDFs show a second peak in the center of the mixing layer region at about $z/h = 0.7$. The two peaks of the PDFs of the gravity currents indicate that two different population of OECSs are present in the flow. As discussed in (van Reeuwijk *et al.*, 2018), the turbulence production is zero at the velocity maximum, implying that the boundary layer becomes ‘decoupled’ from the outer layer. This is corroborated in figure 4.1 by the increasing concentration difference between the boundary layer and outer layer with increasing stratification.

The mean streamwise and wall-normal velocity profiles built with the velocities at the center of the structures are shown in figure 4.3(c) and (d). For a comparison, we show also the unconditioned mean velocity profiles. As shown in figure 4.3(c), the structures follow the mean flow for $z/h < 0.5$, while they are on average somewhat faster than the mean flow in the streamwise direction near the outer region of the current. This is consistent with the behaviour in the wall-normal direction. For $z/h > 0.5$, the OECSs tend, on average, to move upwards. This means that they move from a region with a higher streamwise velocity to a region with a lower one, which makes them faster than the mean flow. Note that the upward movement of the OECSs is consistent with the growth in time of the current depth in the temporal problem. Since the structures are identified uniquely in the turbulent region, they tend to move away from the wall as the current depth grows in time. Since the vertical movement of the fluid is suppressed by stable stratification (Ellison, 1957; Townsend, 1958), this effect is less pronounced as Ri increases. This average movement away from the wall of vortical fluid does not violate conservation of mass as non-turbulent fluid moves on average inward. That is, due to the external intermittency of these flows, the turbulent fraction moves on average outwards, while the non-turbulent fraction move inward. Conversely, the unconditioned vertical mean velocity is zero everywhere.

In the following, we display the spanwise component of the vorticity ω_y at the center of the structures. We present results for $Ri11$ flow case; however qualitatively similar results can be found for the other flow cases (not shown). A joint PDF (JPDF) of ω_y and of the position of the center of the structures is shown in figure 4.4(a). Two distinctive elongated zones of high probability can be observed. Both zones have a peak at about $z/h = 0.7$, but they have opposite signs of the vorticity component. That is, the structures in this region possess either a clockwise and an anticlockwise rotations. As the outer-shape of the JPDF suggests, on average the structures tend to rotate in the counterclockwise direction (negative ω_y) in the outer and in the mixing-layer region while they tend to rotate in the clockwise direction (positive ω_y) in the near-wall region, which is consistent with the sign of the mean velocity gradient in these regions.

The joint PDF of ω_y at the center of the structures with respect to their size is shown in figure 4.4(b). While the two probability peaks of ω_y of opposite sign are positioned at

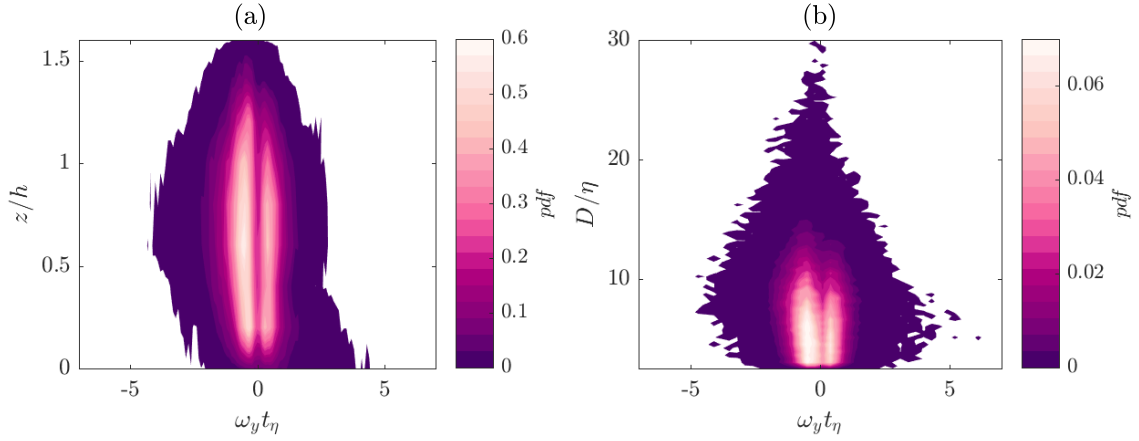


Figure 4.4: JPDFs of the spanwise component of the vorticity at the center of the OECSs and the position of their center (a), respectively their size (b) for Ri_{11} flow case.

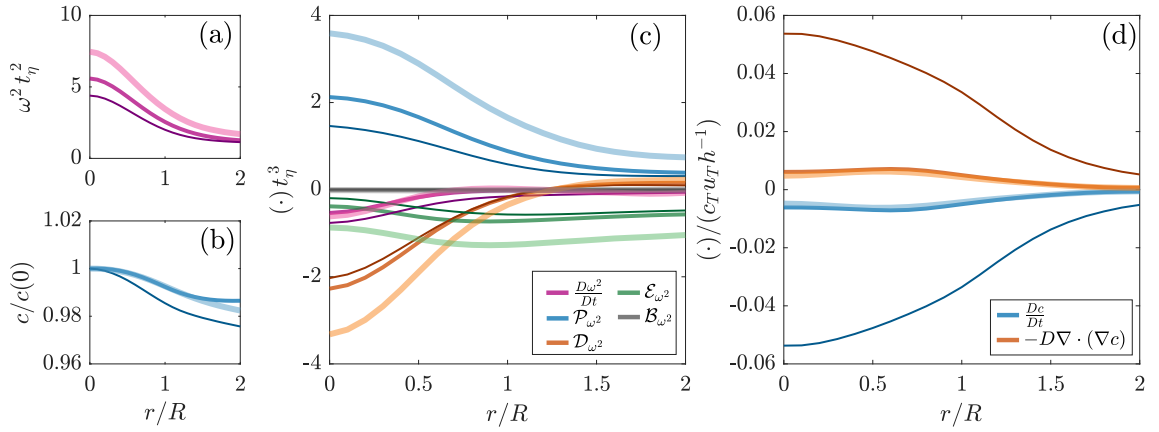


Figure 4.5: Radial profiles of the enstrophy (a) and of the scalar (b) and of the terms in transport equation of enstrophy (c), respectively of the scalar (d). Increasing thickness and transparency of the lines corresponds to increasing Ri .

about 5η , the highest vorticity is associated with structures with a size of $\approx 8 - 10\eta$.

4.3.2 Radial profiles of the terms of enstrophy and scalar transport equations

In this section, we present results for the radial profiles of the terms of the enstrophy and concentration transport equations. As explained in section §4.2, in these profiles the distance from the center of the OECSs is normalized with the distance R between the center of the structures and their boundaries.

In figure 4.5, we show the radial profiles averaged over all the structures in the flow. Figure 4.5(a) shows that the profile of the enstrophy has a bell shape with a maximum at the center of the structure, followed by a sharp decrease towards the boundary at

$r/R = 1$, reaching the unconditioned average value outside the boundaries of the structure at $r/R = 2$. The shape of the enstrophy profile is fundamental to understand how the OECSs are sustained, in that it results from a balance of inertial and viscous effects as shown below. As Ri increases, the profile flattens. This is not unexpected given the smaller magnitude of the vorticity in the whole flow with decreasing stratification. In figure 4.5(b), we also show the radial profile of the scalar normalized with the value at the center of the structures c_0 . The radial profile of c/c_0 shows a similar profile as the enstrophy, although much less steep since it decreases only by a few per cent over the same span.

In figure 4.5(c), the radial profile of the terms in the enstrophy transport equation are shown. The production term \mathcal{P}_{ω^2} is positive with a maximum at the center of the structure and it decreases sharply towards the boundary. This is in agreement with the well-known vortex stretching mechanism, in which the enstrophy is on average produced by the interaction between vorticity ω and rate of strain S_{ij} . Note that \mathcal{P}_{ω^2} has a maximum at the center of the OECSs which is consistent with the radial profile of ω^2 shown in figure 4.5(a). The viscous diffusion of the enstrophy \mathcal{D}_{ω^2} is negative inside the boundaries of the structure and changes sign outside the boundaries. This means that the enstrophy inside the OECSs is diffused through the boundaries of the structures to the surrounding flow. Note that the trend of \mathcal{D}_{ω^2} is also consistent with the radial profile of ω^2 , which shows a negative curvature for $r/R < 1$ and a positive one for $r/R > 1$. The viscous dissipation of the enstrophy \mathcal{E}_{ω^2} is negative everywhere with a minimum (in magnitude) coinciding with the center of the structures. This is again expected based on the radial profile of ω^2 , which shows little variation in the proximity of $r/R = 0$, while it has a sharper decrease towards the boundaries. It is important to note that this view holds for little variation of enstrophy in the axial direction, that is for vortical structures with an elongated shape. In (Neamtu-Halic *et al.*, 2019), we showed that 2D OECSs in vertical planes results as the intersection of tubular structures with the plane itself, justifying thereby our perspective.

The radial profile of the baroclinic torque \mathcal{B}_{ω^2} shows that this term is negligible in comparison with the other terms. This means that on average, \mathcal{B}_{ω^2} has no relevant impact on the enstrophy transport for OECSs. The sum of all the terms, the material derivative of the enstrophy, shows a negative value inside the OECSs with a minimum at $r/R = 0$, reaching an unconditioned negligible value outside the OECSs. The fact that $D\omega^2/Dt$ is negative inside the boundaries of the OECSs means that on average the structures decrease their enstrophy content over their evolution. In particular, it is the negative viscous diffusion of enstrophy in addition to enstrophy dissipation inside the OECSs, which is only partially balanced by the enstrophy production, that causes the decrease of ω^2 over time. As stratification increases, all the terms of the enstrophy transport equation increase in magnitude, which is consistent with the increase of the mean enstrophy at the center of the OECSs with increasing stratification.

In figure 4.5 (d), we show the radial profiles of the terms of the transport equation for the concentration. The diffusion of the concentration $D\nabla \cdot (\nabla c)$ is positive inside the structure which means that the concentration decreases in magnitude. Note that this is also consistent with the radial profile of the concentration (figure 4.5 b) which shows a

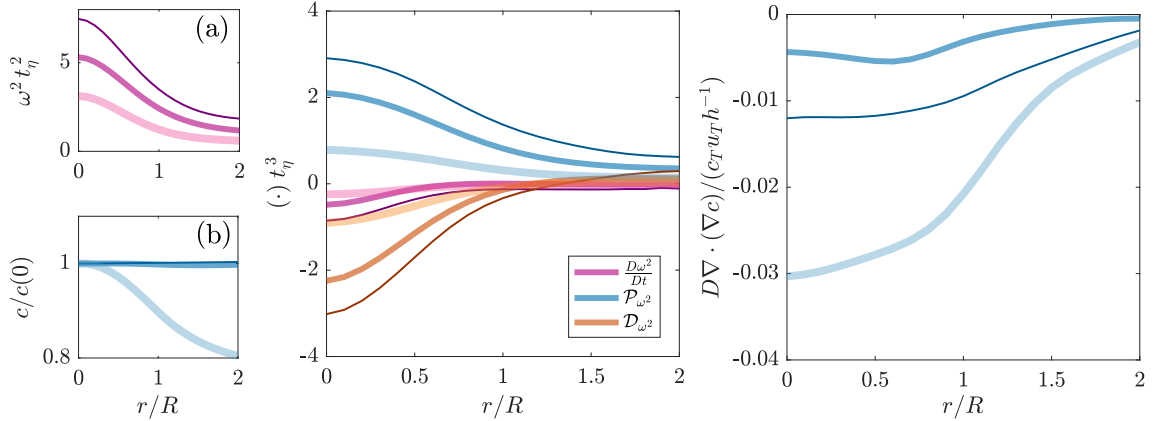


Figure 4.6: Radial profiles of the enstrophy (a) and of the scalar (b) and of the terms in transport equation of enstrophy (c) and of the scalar (d) for $Ri11$ conditioned with respect to the distance of the OECSs from the wall. The thickness and the transparency of the curves increase with the distance from the wall as indicated in the text.

strong positive curvature at $r/R = 0.5$ that decreases towards the boundaries. Moreover, as Ri increases, the diffusion is damped.

In the following we display the same profiles shown in figure 4.5 conditioned with respect to the distance of the center of structures from the wall. We selected three regions: a near-wall region ($z/h < 0.3$), a region where the mean shear is constant ($0.3 < z/h < 1.2$) and a region near the outer boundary of the current ($z/h > 1.2$). In figure 4.6 (c), the profiles of the terms in the enstrophy transport equation show a similar behaviour to the ones presented in figure 4.5(c), although with a different magnitude. They are more intense in the near-wall region and decrease with increasing distance from the wall. This is in agreement with the radial profiles of enstrophy (figure 4.6a), which show more intense values in the near-wall region. Indeed, as observed above, the intensity of mean velocity gradient is maximum near the wall ($z/h < 0.15$), it decreases in the mixing layer ($0.3 < z/h < 1.2$) and it is minimum in the outer region. Differently, the radial profile of the scalar diffusion is more intense in the outer region and is minimum in the region between $0.3 < z/h < 1.2$ (figure 4.6d).

The radial profiles of the terms of enstrophy and scalar transport equation conditioned with respect to the size of the structures are shown in figure 4.7. The limits of the intervals in which the OECSs are grouped are the following: $D/\eta < 4.5$, $4.5 < D/\eta < 8$, $8 < D/\eta < 12$ and $D/\eta > 12$. In figure 4.7(a), we show the radial profiles of the enstrophy. The enstrophy at the center of OECSs increase with the size of the structures to reach a maximum for $8 < D/\eta < 12$, to then decrease again for $D/\eta > 12$. The average size of former interval is 10η , which is the average size of the most intense vortical structures in this work and observed by others (Jiménez *et al.*, 1993; da Silva *et al.*, 2011). The profiles of the terms of the enstrophy transport equation follow a similar trend in which the most "active" OECSs are those in the interval $8 < D/\eta < 12$ (figure 4.7 c). These

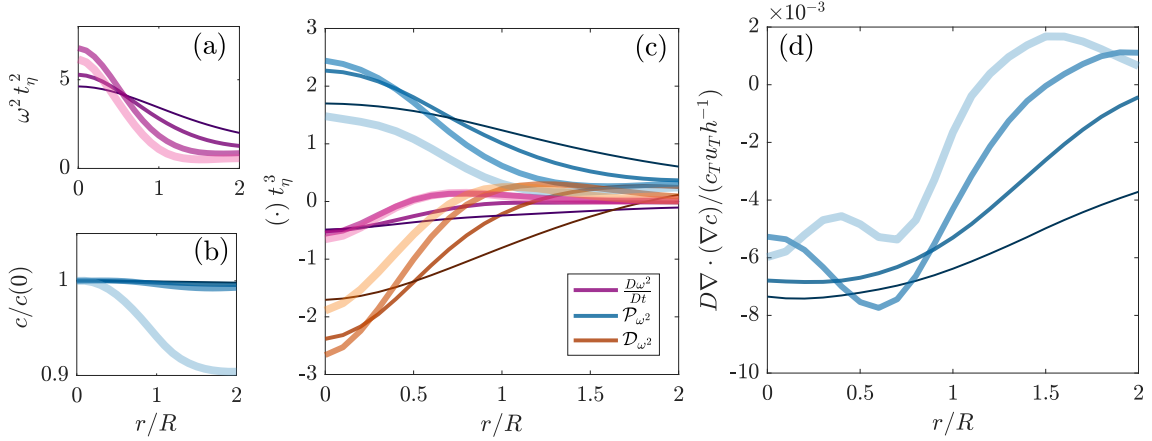


Figure 4.7: Radial profiles of the enstrophy (a) and of the scalar (b) and of the terms in budget equation of enstrophy (c) and of the scalar (d) for $Ri11$ conditioned with respect to the size of the OECSs. The thickness and the transparency of the curves increase with increasing size of the structures, which are divided in the following groups: $D/\eta < 4.5$, $4.5 < D/\eta < 8$, $8 < D/\eta < 12$ and $D/\eta > 12$.

OECSs are also the more stable structures, in that they present a minimum of Dw^2/Dt . A different trend can be observed for the scalar diffusion. The radial profiles of the scalar transport equation show that the magnitude of the scalar molecular diffusion decreases with increasing size of the structures (figure 4.7 d). At first sight, this result seems to be in contradiction with the curvature of the radial profiles of the scalar (figure 4.7 b). However, note that while the radial profiles are normalized with R , the curvature of the profile it is not. That is, a match between the profile of the scalar and the magnitude of the scalar molecular diffusion cannot be expected. The results are qualitatively similar for $Ri0$ and $Ri22$ (not shown).

4.3.3 Impact of coherent structures on the enstrophy and concentration transport near the TNTI

In the following, we investigate the impact of the OECS on the terms of the enstrophy and scalar transport terms conditioned with respect to the TNTI position. The normal distance \tilde{z} from the TNTI is normalized by the Kolmogorov length scale η as it is common in the literature (da Silva *et al.*, 2014; Krug *et al.*, 2015; Silva *et al.*, 2018) and the normal to the interface is oriented in the turbulent direction such that \tilde{z}/η is positive inside the turbulent region and negative outside.

In figure 4.8 (a), we show the conditional average of the enstrophy with respect to the TNTI position. The enstrophy has the typical profile described in the literature, with a sharp increase between $\tilde{z}/\eta = 0$ and $\tilde{z}/\eta \approx 10$. As the stratification increases this jump is less sharp.

The conditional average profiles across the TNTI of the terms of the enstrophy transport

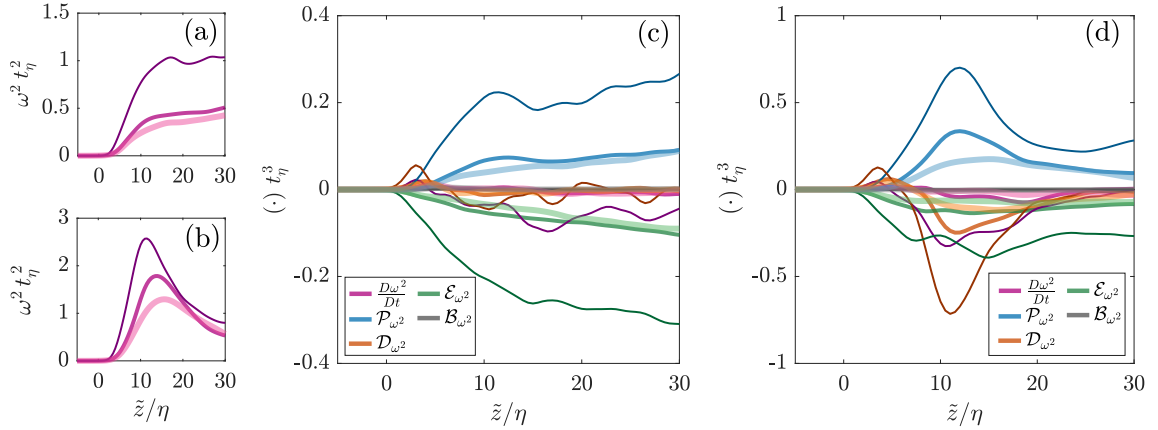


Figure 4.8: Conditional average of the enstrophy (a) and of the terms in the enstrophy transport equation (b) with respect to the TNTI position. Conditional average of the enstrophy (c) and of the terms in the enstrophy transport equation (d) with respect to the presence of an OECS near the TNTI position. The thickness and the transparency of the lines increases with Ri .

equation are shown in figure 4.8. The profiles present the typical shape described in the literature with the presence of three distinct regions. Near the TNTI, the vortex-stretching is negligible and the enstrophy increases due to viscous diffusion. This region, also known as the viscous superlayer (VSL), extends to $\tilde{z}/\eta \approx 4$ where viscous diffusion is maximal. Further inside the turbulent region, the vortex stretching term increases and dominates the enstrophy growth, reaching a maximum at about $\tilde{z}/\eta \approx 11$, where the viscous diffusion shows a minimum, while the dissipation term shows an inflection. The region between $\tilde{z}/\eta \approx 4$ and $\tilde{z}/\eta \approx 11$ is known as the turbulent sublayer (TSL). From here onwards, the viscous diffusion becomes negligible and the vortex stretching is balanced by the viscous dissipation. This region is known as the turbulent core (TC). As also shown by Krug *et al.* (2015), at these Ri the baroclinic torque is negligible near the TNTI.

In the recent literature (Watanabe *et al.*, 2017), it has been inferred that the typical shape of the profiles of the enstrophy transport equation terms across the interface is compatible with the presence of vortical structures at about $\tilde{z}/\eta \approx 9$. This distance was obtained by Watanabe *et al.* (2017), as the sum between the radius $D/2 \approx 5\eta$ of a Burger vortex modelling IVSs and the average size $\delta_v \approx 4\eta$ of the VSL. By superimposing the profiles of enstrophy transport equation terms conditioned with respect to the TNTI to those from the model, they observed a reasonable agreement. To test if the TNTI profiles are compatible with the presence of coherent structures, in figure 4.8 (d), we show the same conditional analysis presented above, this time conditioned with respect to the presence of an OECS. All the terms of the enstrophy transport equation exhibit the same trends shown in figure 4.8(c) although with a different magnitude. Note the different vertical axis limits in figures 4.8(c) and 4.8(d). In particular, in the VSL and the TSL, all the terms are magnified up to one order of magnitude with respect to the levels when conditioned on the

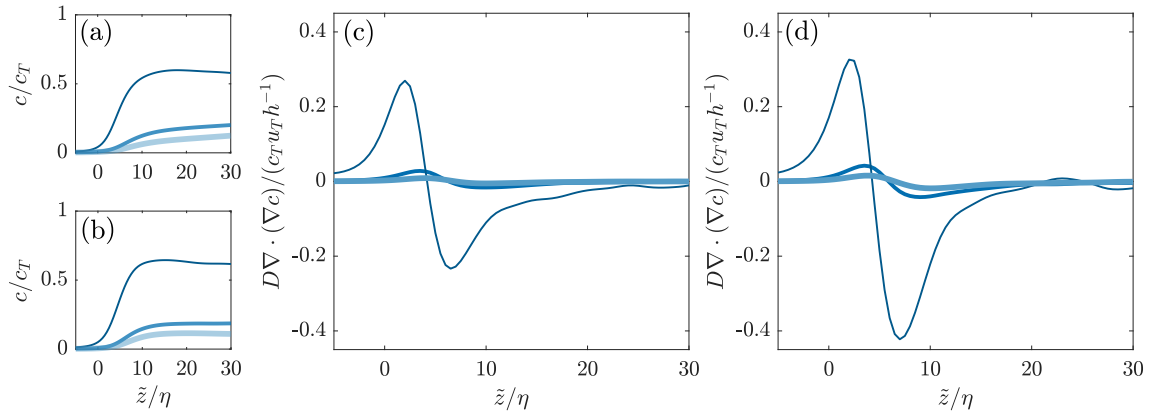


Figure 4.9: Conditional average of the scalar (a) and of the terms in the scalar transport equation (c) with respect to the TNTI position. Conditional average of the scalar (b) and of the terms in the scalar transport equation (d) with respect to the presence of an OECS near the TNTI position.

TNTI only. The shape of the profiles shown in figure 4.8 (d) is consistent with the radial profiles of a coherent structure positioned at a mean distance of $\tilde{z}/\eta \approx 11$. This is further supported by figure 4.8(b), in which we display the conditioned profile of the enstrophy with respect to the TNTI position and the presence of the OECSs. The enstrophy profiles have a peak at about $\tilde{z}/\eta \approx 11$. As shown in Watanabe *et al.* (2017), this position is close to the center of the most dominant vortical structures in the proximity of the TNTI. As the stratification increases, the peak position is slightly farther from the TNTI, which indicates that on average the OECSs are more distant from the TNTI. The results presented here clearly indicate that a large amount of the intensity of the enstrophy transport equation terms near the TNTI is attributable to the OECSs in the interface proximity.

The same analysis conducted above is reproduced for the transport equation of the scalar. Figure 4.9(a) shows that the scalar increases sharply from the non-turbulent to the turbulent side, which is steeper in the presence of OECSs (figure 4.9 b). That is, given that OECSs contain a higher scalar concentration as compared to the background, they also enhance the gradient of the scalar in the proximity of the TNTI. As the stratification increases, the concentration jump is less sharp. The conditional average of the scalar diffusion is shown in figure 4.9 (c). Notably, $D\nabla \cdot (\nabla c)$ is negative in the TC and positive in the TSL. It then changes sign and it shows a positive peak in the VSL. This means that $D\nabla \cdot (\nabla c)$ transports scalar from the TC to the outer fringes of the TNTI. Compatible with the curvature of the scalar profile, this is most effective for the unstratified case when compared to the gravity currents. By conditioning the profile of $D\nabla \cdot (\nabla c)$ with respect to the presence of an OECS, it can be seen that magnitude of the positive and negative peaks near the interface are approximately twice as high. This shows that the OECSs contribute to enhance the scalar diffusion near TNTI.

4.4 Summary and conclusions

We investigated the role of vortical structures on the transport of the enstrophy and of the scalar concentration. To educe vortical structures we employed an objective Eulerian coherent structures (OECSs) extraction method based on the instantaneous vorticity deviation field (IVD).

We showed that high levels of enstrophy can be found within the boundaries of the OECSs. In particular, we showed that the radial profile of the enstrophy has a shape that is reminiscent of a half-Gaussian curve with a maximum at the center of the OECS followed by a sharp decrease towards the boundaries. For highly stable vortical structures, as in the case of the worms investigated by Jiménez *et al.* (1993); da Silva *et al.* (2011) the radial profile of enstrophy has been shown to be Gaussian. In their work, Jiménez *et al.* (1993) identify these worms as regions of space that possess the highest vorticity in the flow (1% of of the total volume). In our approach, even though the vortical structures are identified through a different extraction method that is independent of the vorticity magnitude, the results are very similar to those of Jiménez *et al.* (1993).

The shape of the radial profile of the enstrophy is crucial to understand the time evolution of OECSs, in that it is at the base of the various terms of the enstrophy transport equation. The shape of the stretching and of the viscous diffusion terms are similar to those described in the literature for IVSS Jiménez *et al.* (1993), in which viscous diffusion of enstrophy is balanced by the vortex stretching. While in the previous literature these terms were only inferred based on a fitting to the Burgers model (Jiménez *et al.*, 1993; da Silva *et al.*, 2011), here these terms were computed directly from the flow fields. Moreover, contrary to the Burgers model, we showed that the viscous dissipation of enstrophy is not negligible. We also found that $D\omega^2/Dt$ is on average negative inside the OECSs. This can be explained in terms of vertical movement of the OECSs. By moving upwards, the structures carry enstrophy towards the outer layer of the current where on average enstrophy production cannot sustain the combined effect of viscous diffusion and destruction. As Ri increases, the depth of the current is lower and the mean vorticity is higher. This is reflected on the OECSs enstrophy content which is higher for higher Ri . As a consequence, both the radial gradient and the radial curvature of enstrophy are higher and thus the magnitude of terms of the enstrophy transport equation is stronger. Importantly, we observed that for the gravity currents, the baroclinic torque is negligible in comparison to the other terms of the enstrophy equation.

By investigating the radial profile of the scalar, we showed that it resembles that of the enstrophy except that it is flatter. This means that, the OECSs on average carry a slightly higher scalar concentration compared with the background fluid. This can be explained in terms of material barriers. Since, on average, OECSs move upwards (figure 4.3) and thus towards regions with a lower average concentration, a higher content of the scalar is expected within their boundaries as compared to the fluid around them. As the stratification increases, the radial profile of the scalar is less steep. This may, at first sight, be counter intuitive as c is a passive scalar for $Ri0$, while it is an active one for $Ri11$ and $Ri22$. In the gravity currents, fluid parcels that possess a higher concentration are

lighter and thus one might expect that these lighter parcels migrate towards the center of the OECSs due to centrifugal effects, which should result in a steeper radial profile as compared to $Ri0$. The apparent contradiction may be again explained by vertical movement of the OECSs. Since the structures move on average away from the wall faster in the unstratified case and traverse a steeper concentration gradient, higher differences between the concentration at the center of the OECSs and the surrounding fluid are seen for $Ri0$ as compared to $Ri11$ and $Ri22$. Consistent with the radial profiles of concentration (i.e. their curvature), we also observed that the diffusion of the concentration is positive inside the boundaries of the OECSs, that is, these structures contribute to redistribute the scalar across their boundaries.

Conditioning on the wall-normal position of OECSs center, we observed that the structures near the wall are the most active ones in terms of enstrophy transport. This is not unexpected given the highest gradient of the mean flow in this region. However, a difference we show is that the scalar diffusion is maximum in the outer region. This region corresponds to the maximum upward average velocity of the OECSs, which lends further support to the view that the scalar diffusion is connected to the vertical movement of the structures away from the wall.

The effect of vortical structures on the typical profiles of the enstrophy transport equation conditioned with respect to the TNTI position was investigated by further conditioning the analysis to the presence of OECSs. We showed that with this further condition, the intensity of the terms in the enstrophy transport equation can be one order of magnitude higher. This means that the shape of these profiles across the TNTI might be attributable to vortical structures near the interface. Recently, Watanabe *et al.* (2017) used a stable Burgers vortex positioned at approximately 9η from TNTI to reconstruct relatively well the vortex-stretching and the viscous diffusion profiles across the TNTI. However, in their model the viscous dissipation of enstrophy and the effect of the baroclinic torque are missing. As a difference, with their model we used conditional analysis to assess the impact of the OECSs on all the terms of the enstrophy transport equation near the TNTI. We confirmed their findings related to the vortex-stretching and the viscous diffusion of enstrophy profiles, even though the profiles are compatible with an OECSs positioned a little farther away from the TNTI, i.e. at approximately 11η . This difference may be related to the fact that their Burgers vortex models IVSs, while we employed OECSs that have a different size compared to IVSs. We also showed that while OECSs have no significant impact on the baroclinic torque which remains small in magnitude compared to the other terms, their footprint on the viscous dissipation is not negligible. This means that the model proposed by (Watanabe *et al.*, 2017) could be improved by further taking in account role of vortical structure on the viscous dissipation of enstrophy. Furthermore, compatible with the observations of previous literature (Krug *et al.*, 2015; van Reeuwijk *et al.*, 2019), as the stratification increases, the magnitude of the enstrophy transport equation terms decreases, that is, the OECSs are less 'active' and entrainment process is less effective.

We showed that similar considerations made for the enstrophy transport equation also hold for the scalar transport equation. When the profiles computed by conditioning to the TNTI position are further conditioned to the presence of OECSs, their magnitude is

approximately double. Therefore, the OECSs also play an important role on the diffusion of the scalar across the TNTI by maintaining a steep concentration profile of the scalar.

The methodology used in this work to describe the enstrophy dynamics inside OECSs can be easily extended to other flows. It would be useful to understand if some characteristics of OECSs educed from the flows investigated here share common features with OECSs in other flows. We expect that for free shear flows such as wakes and jets or flows with weak unstable stratification such as turbulent convections in which the baroclinic torque has a weak influence on the enstrophy transport (Holzner & van Reeuwijk, 2017), the enstrophy dynamics of OECSs may be similar to that described here. When the baroclinic torque starts to acquire importance with respect to the other terms of the enstrophy transport equation, as in the case of turbulent plumes (Krug *et al.*, 2017a), the analysis introduced here can be replicated to understand how this term affects the enstrophy dynamics of OECSs and how it impacts enstrophy, scalar transport and the entrainment process near the TNTI.

Bibliography

- BETA, C., SCHNEIDER, K. & FARGE, M. 2003 Wavelet filtering to study mixing in 2d isotropic turbulence. *Comm. Nonlin. Sci. Num. Sim.* **8** (3-4), 537–545. pages 73
- BISSET, D. K., HUNT, J. C. R. & ROGERS, M. M. 2002 The turbulent/non-turbulent interface bounding a far wake. *J. Fluid Mech.* **451**, 383–410. pages 77
- CHAUHAN, K., PHILIP, J., DE SILVA, C. M., HUTCHINS, N. & MARUSIC, I. 2014 The turbulent/non-turbulent interface and entrainment in a boundary layer. *J. Fluid Mech.* **742**, 119–151. pages 73
- CORRSIN, S. & KISTLER, A. L. 1955 Free-stream boundaries of turbulent flows . pages 73
- CRASKE, J. & VAN REEUWIJK, M. 2015 Energy dispersion in turbulent jets. part 1. direct simulation of steady and unsteady jets. *J. Fluid Mech.* **763**, 500–537. pages 75
- DEBUSSCHERE, B. & RUTLAND, C.J. 2004 Turbulent scalar transport mechanisms in plane channel and couette flows. *Int. J. Heat Mass Transfer* **47** (8-9), 1771–1781. pages 73
- DHARMARATHNE, S., PULLETIKURTHI, V. & CASTILLO, L. 2018 Coherent vortical structures and their relation to hot/cold spots in a thermal turbulent channel flow. *Fluid* **3** (1), 14. pages 73
- DIMOTAKIS, P. E. 2000 The mixing transition in turbulent flows. *J. Fluid Mech.* **409**, 69–98. pages 74
- DUBIEF, Y. & DELCAYRE, F. 2000 On coherent-vortex identification in turbulence. *J. Turb.* **1** (1), 011–011. pages 72
- ELLISON, T.H. 1957 Turbulent transport of heat and momentum from an infinite rough plane. *J. Fluid Mech.* **2** (5), 456–466. pages 80
- ELLISON, T. H. & TURNER, J. S. 1959 Turbulent entrainment in stratified flows. *J. Fluid Mech.* **6** (3), 423–448. pages 74

- FRISCH, U. & KOLMOGOROV, A. N. 1995 *Turbulence: the legacy of AN Kolmogorov*. Cambridge university press. pages 72
- FRÖHLICH, J., GARCÍA-VILLALBA, M. & RODI, W. 2008 Scalar mixing and large-scale coherent structures in a turbulent swirling jet. *Flow Turbul. Combust.* **80** (1), 47–59. pages 73
- GANAPATHISUBRAMANI, B., LAKSHMINARASIMHAN, K. & CLEMENS, N. T. 2008 Investigation of three-dimensional structure of fine scales in a turbulent jet by using cinematographic stereoscopic particle image velocimetry. *J. Fluid Mech.* **598**, 141–175. pages 72
- HALLER, G. 2015 Lagrangian coherent structures. *Annu. Rev. Fluid Mech.* **47**, 137–162. pages 72, 77
- HALLER, G. 2016 Dynamic rotation and stretch tensors from a dynamic polar decomposition. *J. Mech. Phys. Solids* **86**, 70–93. pages 76
- HALLER, G., HADJIGHASEM, A., FARAZMAND, M. & HUHN, F. 2016 Defining coherent vortices objectively from the vorticity. *J. Fluid Mech.* **795**, 136–173. pages 72, 76
- HOLZNER, M., LIBERZON, A., NIKITIN, N., KINZELBACH, W. & TSINOBER, A. 2007 Small-scale aspects of flows in proximity of the turbulent/nonturbulent interface. *Phys. Fluids* **19** (7), 071702. pages 77
- HOLZNER, M., LIBERZON, A., NIKITIN, N., LÜTHI, B., KINZELBACH, W. & TSINOBER, A. 2008 A lagrangian investigation of the small-scale features of turbulent entrainment through particle tracking and direct numerical simulation. *J. Fluid Mech.* **598**, 465–475. pages 77
- HOLZNER, M. & LÜTHI, B. 2011 Laminar superlayer at the turbulence boundary. *Phys. Rev. Lett.* **106** (13), 134503. pages 73
- HOLZNER, M. & VAN REEUWIJK, M. 2017 The turbulent/nonturbulent interface in penetrative convection. *J. Turbul.* **18** (3), 260–270. pages 89
- HUA, B.L. & KLEIN, P. 1998 An exact criterion for the stirring properties of nearly two-dimensional turbulence. *Physica D* **113** (1), 98–110. pages 72
- HUNT, J. C. R., WRAY, A. A. & MOIN, P. 1988 Eddies, streams, and convergence zones in turbulent flows . pages 72
- HUSSAIN, A. K. M. F. 1986 Coherent structures and turbulence. *J. Fluid Mech.* **173**, 303–356. pages 72
- JIMENEZ, J. & WRAY, A. A. 1998 On the characteristics of vortex filaments in isotropic turbulence. *J. Fluid Mech.* **373**, 255–285. pages 72

- JIMÉNEZ, J., WRAY, A. A, SAFFMAN, P. G. & ROGALLO, R. S. 1993 The structure of intense vorticity in isotropic turbulence. *J. Fluid Mech.* **255**, 65–90. pages 72, 83, 87
- KADOCH, B., IYER, K., DONZIS, D., SCHNEIDER, K., FARGE, M. & YEUNG, P.K. 2011 On the role of vortical structures for turbulent mixing using direct numerical simulation and wavelet-based coherent vorticity extraction. *J.Turbul.* (12), N20. pages 73, 74
- KANG, S.J., TANAHASHI, M. & MIYAUCHI, T. 2007 Dynamics of fine scale eddy clusters in turbulent channel flows. *J. Turbul.* (8), N52. pages 72
- KRUG, D., CHUNG, D., PHILIP, J. & MARUSIC, I. 2017a Global and local aspects of entrainment in temporal plumes. *J. Fluid Mech.* **812**, 222–250. pages 89
- KRUG, D., HOLZNER, M., LÜTHI, B., WOLF, M., KINZELBACH, W. & TSINOBER, A. 2015 The turbulent/non-turbulent interface in an inclined dense gravity current. *J. Fluid Mech.* **765**, 303–324. pages 74, 78, 84, 85, 88
- KRUG, D., HOLZNER, M., MARUSIC, I. & VAN REEUWIJK, M. 2017b Fractal scaling of the turbulence interface in gravity currents. *J. Fluid Mech.* **820**. pages 76
- LESIEUR, M.L. 1987 *Turbulence in fluids: stochastic and numerical modelling*. Nijhoff Boston, MA. pages 72
- MISTRY, D., PHILIP, J., DAWSON, J. R. & MARUSIC, I. 2016 Entrainment at multi-scales across the turbulent/non-turbulent interface in an axisymmetric jet. *J. Fluid Mech.* **802**, 690–725. pages 73
- NEAMTU-HALIC, M. M., KRUG, D., HALLER, G. & HOLZNER, M. 2019 Lagrangian coherent structures and entrainment near the turbulent/non-turbulent interface of a gravity current. *J. Fluid Mech.* **877**, 824–843. pages 73, 74, 77, 82
- NEAMTU-HALIC, M. M., KRUG, D., MOLLICONE, J.P.AND VAN REEUWIJK, M., HALLER, G. & HOLZNER, M. 2020 Evolution of the turbulence interface in flows with and without stable stratification. *arXiv* . pages 74, 76, 77
- OKUBO, A. 1970 Horizontal dispersion of floatable particles in the vicinity of velocity singularities such as convergences. In *Deep-Sea Res.*, , vol. 17, pp. 445–454. Elsevier. pages 72
- VAN REEUWIJK, M., HOLZNER, M. & CAULFIELD, C. P. 2019 Mixing and entrainment are suppressed in inclined gravity currents. *J. Fluid Mech.* **873**, 786–815. pages 74, 76, 88
- VAN REEUWIJK, M., KRUG, D. & HOLZNER, M. 2018 Small-scale entrainment in inclined gravity currents. *Environ. Fluid Mech.* **18** (1), 225–239. pages 74, 76, 80
- SERRA, MATTIA & HALLER, GEORGE 2016 Objective eulerian coherent structures. *Chaos* **26** (5), 053110. pages 72

- SIGGIA, E. D. 1981 Numerical study of small-scale intermittency in three-dimensional turbulence. *J. Fluid Mech* **107**, 375–406. pages 72
- DA SILVA, C. B., DOS REIS, R.J.N. & PEREIRA, J.C.F. 2011 The intense vorticity structures near the turbulent/non-turbulent interface in a jet. *J. Fluid Mech.* **685**, 165–190. pages 72, 83, 87
- DA SILVA, C. B., HUNT, J. C. R., EAMES, I. & WESTERWEEL, J. 2014 Interfacial layers between regions of different turbulence intensity. *Annu. Rev. Fluid Mech.* **46**, 567–590. pages 73, 78, 84
- SILVA, T. S., ZECCHETTO, M. & DA SILVA, C. B. 2018 The scaling of the turbulent/non-turbulent interface at high reynolds numbers. *J. Fluid Mech.* **843**, 156–179. pages 77, 84
- TANAHASHI, M., IWASE, S. & MIYAUCHI, T. 2001 Appearance and alignment with strain rate of coherent fine scale eddies in turbulent mixing layer. *J. Turbul.* **2** (6), 1–17. pages 72
- TAVEIRA, R. R., D., J. S., LOPES, D. C. & DA SILVA, C. B. 2013 Lagrangian statistics across the turbulent-nonturbulent interface in a turbulent plane jet. *Phys. Rev. E* **88** (4), 043001. pages 77
- TOWNSEND, A.A. 1958 Turbulent flow in a stably stratified atmosphere. *J. Fluid Mech.* **3** (4), 361–372. pages 80
- TSINOBER, A. 2009 *An informal conceptual introduction to turbulence*, , vol. 483. Springer. pages 72
- VINCENT, A. & MENEGUZZI, M. 1991 The satial structure and statistical properties of homogeneous turbulence. *J. Fluid Mech.* **225**, 1–20. pages 72
- WATANABE, T., JAULINO, R., TAVEIRA, R.R., DA SILVA, C.B., NAGATA, K. & SAKAI, Y. 2017 Role of an isolated eddy near the turbulent/non-turbulent interface layer. *Phy. Rev. Fluid* **2** (9), 094607. pages 73, 85, 86, 88
- WATANABE, T., SAKAI, Y., NAGATA, K., ITO, Y. & HAYASE, T. 2015 Turbulent mixing of passive scalar near turbulent and non-turbulent interface in mixing layers. *Phys. Fluid* **27** (8), 085109. pages 74
- WATANABE, T., DA SILVA, C. B., SAKAI, Y., NAGATA, K. & HAYASE, T. 2016 Lagrangian properties of the entrainment across turbulent/non-turbulent interface layers. *Phys. Fluid.* **28** (3), 031701. pages 73
- WEISS, J. 1991 The dynamics of enstrophy transfer in two-dimensional hydrodynamics. *Physica D* **48** (2-3), 273–294. pages 72

- WESTERWEEL, J., FUKUSHIMA, C., PEDERSEN, J. M. & HUNT, J. C. R. 2009 Momentum and scalar transport at the turbulent/non-turbulent interface of a jet. *J. Fluid Mech.* **631**, 199–230. pages 73

Chapter 5

Summary and Conclusions

This dissertation investigates the characteristics and the dynamics of vortical coherent structures in a turbulent flow with and without stable stratification with a particular regard to their impact on the entrainment process. To this end, recently developed vortex identification methods are used (Haller *et al.*, 2016). The peculiarity of these methods is that they are observer-independent, as required for experimentally reproducible coherent structure extraction methods (Haller, 2015). The data used here combines experiments and numerical simulations. The experiments rely on three dimensional particle tracking velocimetry (3D-PTV) measurements of the flow near the turbulent-turbulent/non-turbulent interface (TNTI) of a gravity current, while numerical data constitutes of the direct numerical simulations (DNSs) of temporal gravity currents and of a temporal wall-jet. In the first part of this thesis, the effect of large-scale vortical structures on the turbulent/non-turbulent interface (TNTI) and entrainment of a gravity current is investigated. The vortical structures are deduced through the so-called Lagrangian coherent structures theory and a fully automated 3D extraction algorithm to identify vortical Lagrangian coherent structures (VLCSs) is implemented. The algorithm is applied to the particle trajectories obtained from a newly developed multivolume 3D-PTV measurement of an experimental gravity current. A geometrical description of the VLCSs in the mixing layer of the gravity current shows that the average cross-sectional dimension of the structures is of order of the integral length scale of the turbulence. Similarly to the flow structures described by others (Watanabe *et al.*, 2019), on average the VLCSs are of tubular-shape oriented mainly in the mean flow direction. Our results show that these characteristics depend only weakly from the strength of the stratification. The effect of the vortical structures on the

entrainment mechanism is assessed using a newly developed conditional analysis, based on the presence of the structures in the TNTI proximity. In particular, the VLCSs are observed to influence both the terms that constitute the entrainment flux, namely the area of the TNTI and the local entrainment velocity. On one hand, they modulate the TNTI height, thereby increasing the TNTI surface area, while on the other hand, they organize the flow field on both the turbulent and the non-turbulent regions, thereby modulating the local entrainment velocity. The results presented in this chapter show how the large-scale vortical structures interact with the TNTI in their proximity which is consistent with the cancellation of the dependence of the entrainment rate from the small viscous scales.

Stretching and curvature/propagation effects continuously produce and destroy the surface area of the TNTI. This mechanism is investigated at the TNTI of a temporal gravity current and of a wall-jet generated using DNSs. The results show that on average area production via the stretching mechanism is balanced by area destruction via curvature/propagation effects. This balance holds across several spatial scales of TNTI wrinkles and it is consistent with an observed scale invariance of the nearby coherent vortices. Objective Eulerian coherent structures (OECSs) are extracted from instantaneous snapshots of the DNS flow fields. Using conditional analysis, it is shown that the surface area is produced at the leading edge and destroyed at the trailing edge of the TNTI in the proximity of the OECS. This is interpreted as a consequence of the rotational motion induced by the OECSs to the flow near the TNTI. As the stratification increases, both the production and the destruction of the TNTI area decrease. This is largely connected to a change in the multiscale geometry of the interface which tends to flatten with increasing stratification. The analysis conducted in this chapter is not only a first tentative to describe how the time evolution of the TNTI area in turbulent flows with and without stable stratification, but it also clearly indicates that vortical structures do play an important role in setting the interface area.

Finally, the impact of OECSs on the transport of enstrophy and scalar is investigated using DNSs of temporal gravity currents and of a wall-jet. As a comparison with the previous literature (Jiménez *et al.*, 1993; da Silva *et al.*, 2011; Watanabe *et al.*, 2017) in which they were inferred based on vortex models, the radial profiles inside OECSs of the enstrophy and of the terms in the enstrophy transport equation are assessed directly from the flow fields of the DNSs data. It is shown that the enstrophy profile resembles that of a Gaussian curve with a sharp decrease towards the boundaries of the OECSs. The profile of the enstrophy is crucial to appreciate the shape of the radial profile of the terms of the enstrophy transport equation. The shape of the stretching and of the viscous diffusion are similar to those described in the literature for stable Burgers vortices Jiménez *et al.* (1993), in which viscous diffusion of enstrophy is balanced by enstrophy production via vortex stretching. However, as a difference with the model the viscous destruction of enstrophy is not negligible and the results indicate that OECSs tend on average to lose their enstrophy content. The coupling between the vorticity and the stratification gradient, represented by the baroclinic torque, appears to be negligible. Moreover, the OECSs are shown to trap and transport the scalar from regions with higher concentration to regions with a lower one. Through this mechanism, they enhance the redistribution of the scalar

via molecular diffusion through their boundaries. The profiles of the entropy transport terms across the TNTI are essential to understand how initially irrotational fluid parcels enter in the turbulent region, acquiring vorticity. It is shown that when these profiles are computed by further conditioning them to the presence of an OECS, their magnitude is considerably higher. This means that the shape of these profiles across the TNTI might be largely attributable to the presence of vortical structures near the interface. Lastly, the profile of the scalar across the interface is shown to steepen when an OECS is positioned near the TNTI and the resulting molecular diffusion of the scalar from the turbulent to the non-turbulent region is approximately twice compared with the unconditioned case. These results advance our understanding of the dynamics of OECSs and of their impact on the dynamics of the entrainment process.

5.1 Suggestions for future work

The work presented in this thesis could be extended in several directions.

Firstly, it can be noticed that the size of the structures extracted from the experimental data in the first chapter was about one integral length scale. Although, spanning one order of magnitude, the size of the OECSs extracted from the DNSs is much smaller. This apparent difference may be given by the different resolution of the data. In the experiments the mean interparticle distance between the tracers is about 10η , while the resolution of the DNSs was about 1η . But then which one is the characteristic size of these objective vortical structures? Is it closer to the dissipative scales or of the order of the integral scales? To our view none of two. As commonly accepted in the scientific community, eddies of different scales are superimposed in a turbulent flow. However, the theoretical framework of the extraction methods presented here does not allow the detection of superimposed structures. Thus, if the resolution of the data is sufficiently accurate, the size of the detectable structures is of order of the Kolmogorov microscale and up to one order of magnitude higher. At high enough Reynolds numbers, this size is much smaller than the integral scale. However, if the flow fields are filtered to eliminate the features of the smallest scales, the extraction method is able to identify the largest flow structures. Indeed, in the experimental data, the low resolution might be considered as a filter of the flow field. Thus, a further extension of this work could be a systematic analysis of vortical structures extracted from flow fields filtered with different filter lengths. On one hand, the same analysis presented here might be conducted to verify over how many scales (possibly all), between the dissipative and the integral length scale, the entrainment process and the dynamical behaviour of the structures are self-similar. On the other hand, it would be interesting to understand the relation between the structures at the different length scales. This may open a perspective on the turbulent kinetic energy transfer from the largest to the smallest length scales.

A further possible extension of this work is to apply the different tools here developed to different flow configurations. Indeed the algorithms and the analyses used here could be applied to any type of turbulent flow. It would be useful to understand whether the coherent structures share any common features across a multitude of flows. Remaining in

the context of stratified flows, an appealing configuration is that of an unstably stratified mixing layer. In this case, based on the Atwood number At the flow develops according to different regimes. While for low Atwood numbers the flow is shear dominated, and thus the transition to turbulence is connected to the large-scale Kelvin-Helmholtz structures, at higher At numbers the flow is buoyancy dominated and large-scale plumes guide the thickness of the layer. It is thus interesting to understand how the smallest scale vortices adjust to the different instability that generates the turbulent flow.

Bibliography

- ELSINGA, G.E. & DA SILVA, C.B. 2019 How the turbulent/non-turbulent interface is different from internal turbulence. *J. Fluid Mech.* **866**, 216–238. pages 95
- HALLER, G. 2015 Lagrangian coherent structures. *Annu. Rev. Fluid Mech.* **47**, 137–162. pages 95
- HALLER, G., HADJIGHASEM, A., FARAZMAND, M. & HUHN, F. 2016 Defining coherent vortices objectively from the vorticity. *J. Fluid Mech.* **795**, 136–173. pages 95
- JIMÉNEZ, J., WRAY, A. A., SAFFMAN, P. G. & ROGALLO, R. S. 1993 The structure of intense vorticity in isotropic turbulence. *J. Fluid Mech.* **255**, 65–90. pages 96
- DA SILVA, C. B., DOS REIS, R.J.N. & PEREIRA, J.C.F. 2011 The intense vorticity structures near the turbulent/non-turbulent interface in a jet. *J. Fluid Mech.* **685**, 165–190. pages 96
- WATANABE, T., JAULINO, R., TAVEIRA, R.R., DA SILVA, C.B., NAGATA, K. & SAKAI, Y. 2017 Role of an isolated eddy near the turbulent/non-turbulent interface layer. *Phy. Rev. Fluid* **2** (9), 094607. pages 96
- WATANABE, T., RILEY, J. J., NAGATA, K., MATSUDA, K. & ONISHI, R. 2019 Hairpin vortices and highly elongated flow structures in a stably stratified shear layer. *J. Fluid Mech.* **878**, 37–61. pages 95

Acknowledgements

Time has come to thank you all for contributing in this work and for supporting me all the way till the end of this journey.

Firstly, I would like to thank my Ph.D supervisor Markus Holzner. Your continuous help and support were fundamental for the development of this work. Not only. You carefully and patiently guided me through the vicissitudes of this journey and offered me the chance to cultivate my academic interests. The hours spent together discussing research topics flew by in no time. A special thank you goes to Dominik Krug. This work could not have been done without your advice, your help and your perpetual encouragement. I would like to thank George Haller for the useful suggestions and interesting discussions. I would also like to thank Maarten van Reeuwijk and Jean-Paul Mollicone for their help and incentives. Moreover, I am grateful to Prof. Dr. James Dawson for serving as a referee for my Ph.D defense.

A big thank you goes to all my Ph.D colleagues. I would like to thank Daniel, Maxence and Utku for their kind "welcome" into the group. A particular thank you is reserved for Lukas, who initially introduced me to the lab and with whom I shared the football pitch several times. I would like to thank Pascal. I am glad for having had you as a colleague in this experience and I will definitely miss our timeless, thought-provoking discussions. I would also like to thank Giorgia, Till, Laura and the best office mates Robert and Jen. François and Ursin deserve a special place in these acknowledgements - also, but not only- for their technical support and for being present whenever needed. If from the former I learned how to do a well organized lab work, with the latter we manage to avoid burning down the lab despite our technical knowledge of optical lenses, which is still a great result in my opinion. I am happy to see that my work will be continued by Stefano. I am sure you will do a great Ph.D. While all our glorious plans for a joint, outstanding, lunch paper have miserably failed, we still have time to make it in the future.

Fortunately, I was not alone along this journey and I wish to thank my friends that somehow supported me through it. I would like to thank Gianluca, Emiliano, Pierluigi, Alessandro and Federico for visiting me in Zürich, as well as Alessio and João that were

always there for our evening talks.

I would like to express my gratitude to my extended family believing in me; I always felt your moral support.

Finally, a special 'Thank you' is reserved to my wife Alessandra. Thank you for being always at my side, for being patient with me, for advising me, for inspiring me and for smoothing all my edges. This work could not have existed without your unconditional support and encouragement.

Curriculum Vitae

Marius Mihai Neamtu-Halic

Date of birth: October 22, 1989

Nationality: Romanian

neamtu@ifu.baug.ethz.ch

Education

10/2016 - 05/2020 Ph.D studies at ETH Zurich, Switzerland, Institute of Environmental Engineering - Thesis: "Objective coherent structures near the turbulent/non-turbulent interface of a gravity current" (Supervisor Prof. Dr. Markus Holzner).

10/2013 - 03/2016 Master of Science in Civil Engineering at Roma TRE university of Rome, Italy - Thesis: "Numerical and experimental simulation of non-Boussinesq gravity currents" (Supervisors: Prof. Dr. Giampiero Sciortino and Dr. Valentina Lombardi).

10/2010 - 10/2013 Bachelor of Science degree in Civil Engineering at Roma TRE university of Rome, Italy - Thesis: "Hydraulic design of a retention basin for first flush water of a storm sewer system in the district of *Fiera di Roma*" (Supervisors: Prof. Dr. Corrado Paolo Mancini).

09/2005 - 06/2010 High school degree at *Liceo Scientifico Gregorio da Catino* Poggio Mirteto, Italy.

Journal Publications

1. M. M. Neamtu-Halic, J.P. Mollicone, M. van Reeuwijk and M. Holzner (2020). *Role of vortical structures for enstrophy and scalar transport in flows with and without stable stratification*. Submitted to *J. Turbul.*
2. M. M. Neamtu-Halic, D. Krug, J.P. Mollicone, M. van Reeuwijk, G. Haller and M. Holzner (2020). *Connecting the time evolution of the turbulence interface to coherent structures*. Accepted for publication in *J. Fluid. Mech.*
3. M. M. Neamtu-Halic, D. Krug, G. Haller and M. Holzner (2019). *Lagrangian coherent structures and entrainment near the turbulent/non-turbulent interface of a gravity current*. *J. Fluid. Mech* 877(824-843), doi:10.1017/jfm.2019.635

Conference contributions and PhD Summer schools

1. Attendance at PhD summer school organized by CISM-JMBC. Name of the course: "Complex Flows and Complex Fluids". 8th - 12th May 2017, Udine, Italy.
2. Attendance and talk at European Mechanics Society Colloquium 590: "Turbulent/non-turbulent interface: from laboratory to geophysical scales" 3th - 5th July 2017, London, UK.
3. Attendance and poster at European Mechanics Society Colloquium 586: "Turbulent superstructures in closed and open flows" 12th - 14th July 2017, Erfurt, Germany.
4. Attendance and talk at the 16th European Turbulence Conference: 21st - 24th August 2017, Stockholm, Sweden.
5. Attendance and talk at Priority Program PhD fall school organized by SPP1881. Name of the course: "Turbulent Superstructures" 9th - 13th October 2017, Bad Hersfeld, Germany.